STUDIES IN FLUID MECHANICS

by

MICHAEL S. KOLANSKY

A dissertation submitted to the Graduate Faculty in Engineering in partial fulfillment of the requirements for the degree of Doctor of Philosophy, The City University of New York

1976

This manuscript has been read and accepted for the Graduate Faculty in Engineering in satisfaction of the dissertation requirements for the degree of Doctor of Philosophy.

7/30/76
date

Chairman of Examining Committee

8/2/76
date

for Executive Officer

Robert Pfeffer, chairman

Sheldon Weinbaum

Latif Jiji

Norman Jen

Supervisory Committee

The City University of New York

TO

MY

PARENTS

ABSTRACT

STUDIES IN FLUID MECHANICS

by

Michael S. Kolansky

Advisor: Professor Robert Pfeffer

Co-Advisor: Professor Sheldon Weinbaum

Chapter I

Simultaneous gas and particle velocity profiles and turbulence intensities were obtained for the flow of 22 and 36 micron diameter glass beads in air using fiber film and laser Doppler anemometry. The suspensions were circulated in a 2.2 centimetre closed loop at air Reynolds numbers between 17,000 and 22,000 at solids loading ratios between 0 and 2.

The velocity profile measurements indicated that large slip velocities were not generated in the near wall region although a significant slip of the order u* between the mean profiles extends well into the core (up to $y/R \approx 0.5$) and a value of y^+ equivalent to approximately 10 buffer layer thicknesses. The integrated viscous dissipation due to particle slip across this much thicker region is thus of the same order as that calculated using a much thinner (buffer layer) model with much larger slip velocities.

Chapters II and III

A new approximate theory is described for treating the flow past 2-dimensional and axisymmetric bluff objects in the intermediate regime $0(1) < Re < 0(100)$. The theory is based on a new simplyfying hypothesis for the pressure field which enables one to take account of the displacement interaction and centrifugal effects in thick viscous layers by modifying the surface pressure boundary condition. Detailed numerical comparisons with available finite difference solutions of the Navier-Stokes equations for both 2-dimensional (cylinders, parabolas of revolution) and axisymmetric (spheres, prolate spheroids, paraboloids of revolution) bodies are in very good agreement.

Acknowledgement

I would like to express my sincere appreciation to Professors Robert Pfeffer and Sheldon Weinbaum for their guidance, inspiration and patience during the course of my graduate studies. Their confidence in me never waivered and the debt that I owe them can never be repaid. Thanks also go to Dr. Michael J. Gluckman for his many helpful suggestions.

I would also like to express my appreciation to the Chemical Engineering Department shop but most especially to Mr. Fred Schwarz.

During the course of my studies I was financially supported by a NDEA Title IV fellowship, University Research Assistantship and a University Fellowship. I gratefully acknowledge this assistance. In addition, the experimental research presented in Chapter I was supported by the National Science Foundation under Contract ENG 74-21714. The theoretical research presented in Chapters II and III was supported by the Office of Naval Research under Contract NR-061-208.

TABLE OF CONTENTS

Page

DEDICATION

ABSTRACT

ACKNOWLEDGEMENT

TABLE OF CONTENTS

LIST OF TABLES

LIST OF FIGURES

NOMENCLATURE

INTRODUCTION

CHAPTER I. DRAG REDUCTION IN DILUTE GAS SOLID SUSPENSION FLOW: GAS AND PARTICLE VELOCITY PROFILES

1. Introduction I-1
2. Experimental Apparatus I-4
3. Mean Velocity Profiles I-12
4. Turbulence Intensity Profiles I-14
5. Drag Reduction Results I-16
6. Motion Picture Results I-19
7. Theoretical Considerations and Discussion I-21
8. Additional Results and Discussion I-31
9. References I-35
10. Experimental Evidence of Drag Reduction I-38
11. Figures I-40

Appendix A: Motion Picture Commentary I-A-1

TABLE OF CONTENTS

Page

CHAPTER II. AN APPROXIMATE THEORY FOR INCOMPRESSIBLE VISCOUS FLOW PAST TWO-DIMENSIONAL BODIES IN THE INTERMEDIATE REYNOLDS NUMBER REGIME $O(1) < Re < O(10^2)$

1.	Introduction	II-1
2.	The New Pressure Hypothesis for the Viscous Layer	II-7
3.	The New Boundary Value Problem	II-12
4.	Solution Procedure	II-14
5.	Parabolic Cylinders	II-22
6.	Circular Cylinders	II-26
7.	Additional Results and Comments	II-29
8.	References	II-32
9.	Figures	II-33

TABLE OF CONTENTS

Page

CHAPTER III: AN APPROXIMATE THEORY FOR THE STREAMING MOTION PAST AXISYMMETRIC BODIES AT REYNOLDS NUMBERS FROM 1 TO APPROXIMATELY 100

1. Introduction III-1
2. The Boundary Value Problem for Axisymmetric Flow III-7
3. Solution Procedure III-10
4. Paraboloids of Revolution III-20
5. Spheres III-23
6. Additional Results and Comments III-27
7. References III-28
8. Figures III-29

TABLE OF CONTENTS

	Page
CHAPTER IV: CONCLUDING REMARKS	IV-1

LIST OF TABLES

Page

CHAPTER I

CHAPTER II

CHAPTER III

TABLE I Forward stagnation point shape Factor vs. Reynolds Number for a sphere III-16

TABLE II Separation Angle vs. Reynolds Number III-25

CHAPTER IV

LIST OF FIGURES

Figure		Page
	CHAPTER I	
1	Closed Loop System	I-40
2	Mass Flowmeter	I-41
3	Schematic of the Laser Anemometer Optical Arrangement	I-42
4	Photograph of the Laser Anemometer Traverse Mechanism	I-43
5	Clean Air Velocity Profiles	I-44
6	Comparison of Particle and Gas Velocity Profiles in Suspension Flow	I-45
7	Air Mean Velocity Profiles in Suspension Flow	I-46
8	Particle Mean Velocity Profiles in Suspension Flow	I-47
9	Gas Mean Velocity Profiles	I-48
10	Dimensionless Mean Air Velocity as a Function of Dimensionless Distance From the Wall in Suspension Flow	I-49
11	Dimensionless Mean Particle Velocity as a Function of Dimensionless Distance From the Wall in Suspension Flow	I-50
12	Air Mean Velocity Profiles in Suspension Flow	I-51
13	Particle Mean Velocity Profiles in Suspension Flow	I-52
14	Streamwise Intensity of Turbulence Profiles of Clean Air as Measured with the Laser Anemometer	I-53

Figure		Page
	CHAPTER I (cont.)	
15	Dimensionless Streamwise Gas Turbulence Intensity Ratio in Suspension Flow	I-54
16	Dimensionless Streamwise Particle Turbulence Intensity Ratio in Suspension Flow	I-55
17	Friction Factor Ratio versus Loading Ratio	I-56
18	Friction Factor Ratio versus Loading Ratio	I-57
19	Effect of Eddy Motion on Particle Slip Velocity	I-58
20	Fit of Equation 29 to Particle Slip Velocity	I-59
21	Friction Factor versus Reynolds Number for the 3.81 cm Test Section	I-60
22	Clean Air Velocity Profiles for the 3.81 cm Test Section	I-61

Figure		Page
	CHAPTER II	
1	Boundary Layer Coordinate System	II-33
2	Surface Pressure Distribution for a Parabolic Cylinder	II-34
3	Surface Pressure Distribution for a Parabolic Cylinder	II-35
4	Stream Function Fit of the Displacement Body for a Parabolic Cylinder	II-36
5	Stream Function Fit of the Displacement Body for a Circular Cylinder	II-37
6	Successive Approximations for the Displacement Body for a Circular Cylinder	II-38
7	Separation Angle as a Function of Reynolds Number for a Circular Cylinder	II-39
8	Surface Pressure Distribution around a Circular Cylinder	II-40
9	Surface Pressure Distribution around a Circular Cylinder	II-41
10	Surface Pressure Distribution around a Circular Cylinder	II-42
11	Angle of Minimum Surface Pressure for a Circular Cylinder	II-43
12	Surface Vorticity Distribution around a Circular Cylinder	II-44
13	Velocity Profile Development in the Viscous Layer around a Circular Cylinder	II-45

Figure		Page
	CHAPTER II (cont.)	
14	Velocity Profile Development in the Viscous Layer around a Circular Cylinder	II-46
15	Separation Angle as a Function of Reynolds Number for Elliptic Cylinders, with Aspect Ratio as a Parameter	II-47

Figure		Page
	CHAPTER III	
1	Boundary Layer Coordinate System	III-29
2	Surface Pressure Distribution for a Paraboloid of Revolution	III-30
3	Surface Pressure Distribution for a Paraboloid of Revolution	III-31
4	Stream Function Fit of the Displacement Body for a Sphere	III-32
5	Stream Function Fit of the Displacement Body for a Sphere	III-33
6	Successive Approximations for the Displacement Body for a Sphere	III-34
7	Successive Approximations for the Displacement Body for a Sphere	III-35
8	Separation Angle as a Function of Reynolds Number for a Sphere	III-36
9	Surface Pressure Distribution around a Sphere	III-37
10	Surface Pressure Distribution around a Sphere	III-38
11	Surface Pressure Distribution around a Sphere	III-39
12	Angle of Minimum Surface Pressure for a Sphere	III-40
13	Surface Vorticity Distribution around a Sphere	III-41
14	Velocity Profile Development in the Viscous Layer around a Sphere	III-42
15	Velocity Profile Development in the Viscous Layer around a Sphere	III-43

Figure		Page
	CHAPTER III (cont.)	
16	Stream Function Fit of the Displacement Body for a Prolate Spheroid	III-44
17	Surface Pressure Distribution around a Prolate Spheroid	III-45
18	Stream Function Fit of the Displacement Body for a Prolate Spheroid	III-46
19	Surface Pressure Distribution around a Prolate Spheroid	III-47

NOMENCLATURE

The principal symbols are shown below. Symbols for quantities having only temporary significance are not shown, but are clearly defined in the text. A certain amount of duplication of symbols occurs, in which cases all pertinent definitions are given and in some cases are followed by equation numbers in parenthesis which correspond to the particular definitions.

CHAPTER I

$\mathring{A}$	angstroms
A(1), A(2)	local constants
B(1), B(2)	local constants
d	particle diameter
d_f	fringe spacing
D	pipe inside diameter
e	base of natural logarithms
f_g	clean gas friction factor
f_s	suspension friction factor based on clean gas properties
f_o, f_s, f_p	focal lengths defined in Figure I-3
F_D	doppler frequency
g	gravitational acceleration
G, G_s	local constants
I	turbulence intensity
K, K_s	Von Karman type constants
l, w	measuring volume dimensions

ℓ_g	mixing length of gas
ℓ_p	mixing length of particle
L	vertical length of test section
ΔP	total measured pressure drop across a test section
ΔP_{ads}	pressure drop associated with solids acceleration
ΔP_{ag}	pressure drop associated with gas acceleration
ΔP_{fcg}	pressure drop associated with clean gas skin friction
ΔP_{fds}	pressure drop associated with direct contact solids friction and with maintaining particles in suspension
ΔP_{fg}	pressure drop associated with gas skin friction in a suspension
ΔP_{fs}	$= \Delta P_{fds} + \Delta P_{fg}$, total frictional pressure drop in a suspension
ΔP_h	pressure drop associated with static head of mixture
ΔP_{hds}	pressure drop associated with static head of solids
ΔP_{hg}	pressure drop associated with static head of gas
R	tube radius
Re_g	$\overline{U}_g D/\nu$, gas Reynolds number
t_e	eddy relaxation time
t_i	interaction time
t_s	stokes relaxation time
t^*	short time
u_i	fluctuating gas velocity component

$\vec{u}$	fluctuating gas velocity vector
u^*	friction velocity
U	local mean velocity
$\overline{U}_g$	bulk average gas velocity
U_{gsl}	slip velocity
v_i	fluctuating particle velocity component
$\vec{V}$	fluctuating particle velocity vector
V	particle velocity (I-6a)
$\overline{V}_m$	measuring volume
$\overline{V}_p$	bulk average particle velocity
y	distance from wall
α	constant of proportionality (I-13)
β	density ratio (I-10)
η	loading ratio
θ	laser beam intersection angle
λ	wavelength of laser
μ	gas viscosity
ν	gas kinematic viscosity
π	constant, 3.14159
ρ_{ds}	density dispersed solids
ρ_g	gas density
ρ_s	particle density
σ,σ_p,σ_L	optical parameters defined in Figure I-3
σ	defined in equation I-16
τ	dimensionless time
τ_w	wall shear stress

Superscripts and Subscripts

c	centerline
d_s	dispersed solids
e	edge of viscous layer
f_s	gas property in suspension flow
f_o	clean gas property
g	gas
h	hydrodynamic head
p	particle
s	suspension
1	streamwise
2	vertical (normal)
3	spanwise
-	(bar), average
+	dimensionless quantity
→	(arrow), vector

NOMENCLATURE

CHAPTERS II AND III

A_1, A_2	local constants
c	local constant
C_p	pressure coefficient
D^2	Stokes stream function operator
e, f, g, h	local constants
F	complex potential
F_1, F_2	local constants
G	local constant
m	strength of source/sinks
p	pressure
q	speed
r	radial distance
R	radius of curvature (II-I)
R, R_o	defined by Figure III-1
Re	Reynolds number
s, n	natural streamline coordinates
u	local fluid velocity
u, v	coordinates in the W complex plane
U	inviscid tangential velocity
U_∞	free stream velocity
v	normal velocity component (II-14)
W	complex plane
X, R	cylindrical polar coordinates (III-19)
x, y	boundary layer coordinates (II-10)

x, y	cartesian coordinates (II-24)
Z	complex plane
γ	local curvature (III-12b)
δ	boundary layer thickness
δ^*	displacement thickness
ε	local angle of curvature
θ	momentum thickness (II-16, III-11b)
θ	angular coordinate
Λ	shape factor
ν	fluid kinematic viscosity
π	constant, 3.14159
ρ	fluid density
Σ	summation
τ	shear stress
ϕ	angular coordinate, $180^\circ - \theta$
Φ	velocity potential
Ψ	stream function
ω	vorticity
∇^2	laplace operator

Superscripts and Subscripts

e	displacement body
f_{sp}	forward stagnation point
n	normal
w	wall
0	forward stagnation point
$*$	displacement body
∞	free stream quantity, infinity

INTRODUCTION

This dissertation is based upon the two research projects that I have been engaged in over the past 4-1/2 years.

Chapter I deals with the experimental measurement of gas and particle velocity profiles and turbulence properties in a flowing dilute gas-solid suspension in a tube in an effort to gain a better understanding of the phenomenon of drag reduction which has been observed independently by many investigators in these flows.

Initially it was planned that I concentrate my entire research effort on this experimental work. However, I experienced a multitude of difficulties in modifying the existing experimental apparatus and setting up the DISA laser Doppler anemometer (LDA). After a six month delay due to slow delivery of supplies the test apparatus used by Kane et al (1973, Chapter I) was successfully modified to include the glass optical sections necessary for the LDA. The basic problem encountered with the LDA was that the DISA tracker would not track the Doppler signal obtained in the suspension flow. After a year and a half of trying to get the tracker to work including many trips to the DISA office in New Jersey it looked as if I was no closer to my goal than when I started. Because of this long delay I became somewhat apprehensive and asked my advisors, Professors Pfeffer and Weinbaum, for another thesis topic.

My new topic, the results of which are presented in Chapters II and III, dealt with the development of a new intermediate Reynolds number boundary layer theory for the flow past 2-dimensional and axisymmetric

bluff bodies. The new boundary layer theory herein developed successfully bridges the gap between existing high Reynolds number (Inviscid) boundary layer theory and the low Reynolds number (Re < 1) Stokes and Oseen theories. This second research project was quite different from the first. Whereas the first project consisted of experimental measurements in a two phase (gas-particle) turbulent flow the second project was an analytic and computational development of laminar flow theory around bluff bodies. The two projects were, however, related in the sense that they were both concerned with basic problems in fluid mechanics.

While working on the new analytic research I also continued the experimental work and as it turned out after another two years of work I was able to get the equipment operating and obtain meaningful and useful experimental results. At this point my guidance committee decided that because both projects were proceeding well and were useful contributions my dissertation should be comprised of both studies. Hence, the title "Studies in Fluid Mechanics".

This thesis is organized in such a way that each of the three chapters is suitable for publication in a scientific journal. Each chapter, therefore, has its own introduction, reference list and page numbering.

CHAPTER I: DRAG REDUCTION IN DILUTE GAS SOLID SUSPENSION FLOW: GAS AND PARTICLE VELOCITY PROFILES

1. INTRODUCTION

The objective of this research was the experimental measurement of gas and particle velocity profiles and turbulence properties in a flowing dilute gas-solid suspension in a tube in an effort to gain a better understanding of the phenomenon of drag reduction which has been observed in these flows. The highly abrasive nature of the suspension flow makes the use of hot-wire anemometry impossible; even relatively rugged probes such as the fiber film types used by Kane et al (1973) fail after a short time when subjected to particle bombardment. Furthermore, because of the physical size of these probes measurements close to the wall of the tube cannot be obtained. It was, therefore, desirable to use a measurement technique which did not require the use of probes.

The laser Doppler anemometer seemed to be the obvious solution to the problem. It does not require a probe to be inserted into the flow and, therefore, theoretically should allow measurements very close to the tube wall. It also allows for the direct measurement of particle velocities. Since drag reduction must be related to the effect of the slip between the particles and gas flow this was an important consideration.

Initial measurements using the laser Doppler anemometer were made with submicron graphite particles to seed the flow. These results compared favorably with fiber-film measurements in the clean gas. We then proceeded to make measurements in dilute gas-solids suspensions using two different particle sizes; #279 glass beads having a weight mean diameter of 22μm and #380 glass beads having a weight mean diameter

of 36 μm. These are the same particles used in an earlier study (Kane et al, 1973).

In addition to the laser Doppler and fiber-film measurements we also took a series of high speed (3000-6000 frames per second) motion pictures of the flowing gas-solids suspension in both vertical and horizontal test sections. These provided a good insight into the macroscopic properties of the suspension flow.

Pfeffer and Kane (1974) have written a comprehensive paper reviewing the present knowledge of gas-solids drag reduction in terms of experimental evidence and theoretical explanations. They also proposed a uniform definition of the suspension friction factor which would allow meaningful comparisons between results obtained from independent investigators. Section I, reproduced from Pfeffer and Kane (1974) summarizes literature reports of gas-solids drag reduction in tubes. In their review paper they also examined and evaluated six different theoretical explanations for drag reduction including the following: general turbulence suppression, stabilization, introduction of length and time scales, and local turbulence effects in the sublayer.

The first study of dilute gas-solids suspensions employing laser Doppler anemometry was that of Carlson (1973). He measured particle velocities in suspensions of 107μm and 22μm glass beads in a square duct. The gas velocity was measured by seeding the flow with contaminate material of less than 10μm in diameter. It was found that even for the 22μm particles the gas-particle slip velocity at the duct center was not negligible. In the case of the 107μm glass beads the difference between the gas velocity, measured assuming the contaminants follow the flow, and particle velocity was large enough to allow

resolution of two Doppler signals. This was not possible for the smaller 22μm beads because the gas and particle velocities overlapped.

Einav and Lee (1973) have also reported the ability to measure simultaneous liquid and particle velocities in laminar flow along a flat plate. In their study the particle and liquid velocities did not overlap and so the two Doppler signals could easily be separated.

The first reported measurements in which both gas and particle velocities were obtained in a region of velocity overlap was provided by Stock et al (1975). They studied the flow of a suspension of 60μm particles in air which had been cleaned of all particles greater than 1μm. Their study, which employed a counter type laser anemometer, was based on the work of Farmer (1972) and Haertig and Fleck (1974). Farmer showed that it is possible to determine particle size by comparing the Doppler part of the signal (AC) with the pedestal (DC). Haertig and Fleck (1974) showed that it is possible to distinguish large particles from small ones by the size of the Doppler pedestal (DC). Using this as a basis, Stock was able to differentiate between the signal attained from the large 60μm particles and that obtained from the smaller 1μm particles.

Recently, Birchenough and Mason (1976) have used a laser Doppler anemometer to measure particle velocities in the wall region of an upward flowing gas-solid suspension of fine (21μm mean diameter) alumina particles. Solids loading ratios (η) ranged from 0.5 to 5.0. Their study indicated that use of a laser anemometer at solids loading ratios above 2 was entirely feasible.

2. EXPERIMENTAL APPARATUS

The experimental test setup used in this study is shown in Figure 1. The physical layout is essentially the same as that described by Kane et al (1973). This test setup is unique in that it allows operation in a closed loop configuration. This eliminated the health hazards inherent in any study using micron and sub-micron size particles. Motive power for the flow was provided by a specially designed centrifugal circulator (Wachtell and Wagner, 1964) which was capable of pumping gas and solids simultaneously without damage to its internal parts. Because of this fact, solids inventories of less than 200 grams were required. Kane et al (1973) found only minimal degradation of the particles used in this study after prolonged circulation. The general procedure followed in all measurements was to add particles to the loop in 20 gram increments. A port was provided for introduction of the solids, as noted in Figure 1. Equilibrium was generally reached within 2-3 minutes after the circulator was turned on.

An important requirement in any gas-solid suspension work is the ability to measure the amount of particles in the flow. In this study we used the mass flowmeter originally designed by the Bureau of Mines (Gibson, Abel, Fashing, 1963) and modified by Rossetti and Pfeffer (1972). A cross section of the mass flowmeter is shown in Figure 2. A complete description is provided by Kane et al (1973). The flowmeter was comprised of two sections. The first section consisted of an orifice plate which was used to measure the gas mass flow rate. It was found that the presence of particles had no effect on the orifice measurements. This agreed with the findings of Boothroyd (1966). The second section contained a cantilevered steel target joined to a flat

steel support rod. Temperature compensated strain gauges were mounted on the top and bottom sides of the flat steel support. The operation of the target meter was based on the linear relationship between the deflection of a cantilever and the force producing the deflection. The deflection of the target as measured by the strain gauges, was filtered and recorded on a Brush model 280 recorder. Calibrations in an open loop configuration were made by Kane et al (1973) for the two particle sizes used in this study. The flow meter provided an extremely accurate and simple method to determine the instantaneous gas-solids loading ratios.

The only significant change in the experimental apparatus used by Kane et al (1973) was the inclusion of a perfectly smooth fused quartz optical test section in the downward vertical leg of the loop. The test section has an inside diameter of 22 mm and a wall thickness of 1.5 mm. Fused quartz was chosen because of its high transmission of light at 6328Å (the wavelength of the helium-neon laser). The section also proved to be resistant to the abrasive suspension. The inside diameter of the quartz tube was identical to the stainless steel tubing that comprised the remainder of the loop. The glass-steel joints were made using Cajon Ultra-Torr fittings. The 91.4 mm test section was fitted with two pressure taps 76.2 mm apart and a port suitable for insertion of fiber film probes. The anemometer port and pressure tap holes were precision drilled in the glass tube to insure a sharp edge. Aluminum clamps were affixed to the tube to hold the pressure taps (.33 mm stainless steel tubing) and silicone rubber was used as a sealant. Two R. Feuss model 134B, micromanometers filled with 0.8 specific gravity alcohol were used to measure the pressure drops across the vertical

glass and horizontal steel test sections. The micromanometers were connected to the taps using 1.58 mm I.D. Tygon tubing.

All gas profile measurements (excluding laser anemometry using sub-micron graphite) were made with electronic anemometry and fiber film probes (55F16) manufactured by the DISA S&B Corporation. The basic anemometer unit consisted of a type 55DØ1 constant temperature anemometer, a type 55D30 D.C. voltmeter and a 55D35 root mean square (r.m.s.) voltmeter. The probes were inserted into the vertical test section through a 6.35 mm precision drilled port (mentioned previously). An aluminum clamp was affixed to the tube using silicone sealant and a 3.175 mm swagelok connector with Teflon ferrules was used to provide a seal while still permitting probe traverse. A DISA S&B type 55HØ1 traversing mechanism was used. The 55HØ1 was manually gear operated to an accuracy of .01 mm. The entire apparatus was rigidly affixed to the laser anemometer traverse supports. The fiber film probes were calibrated using a DISA model 55D41 wind tunnel. Such calibrations are fairly routine. The procedures used are described by Kane et al (1973).

Figure 3 shows the optical arrangement used for laser Doppler measurements. All measurements were made in differential Doppler mode. The optical components including the laser, beam splitter and the photo-multiplier were mounted on a 150 cm long steel optical bench (DISA 55L60). A photograph of the arrangement is shown in Figure 4. The location of the beam intersection was easily controlled by a dual axis traversing table (Setco Industries model 104) which had 7.62 cm of travel and was adjustable to .0127 of a mm. The traversing table was attached to an aluminum plate which was in turn attached to a steel plate.

The whole arrangement, laser optics, optical bench, traversing mechanism and plates, weighed approximately 91 Kg. This entire assembly was isolated from vibration using four dashpot type vibration eliminators of the kind normally used to isolate small motors. The vibration eliminators were in turn attached to another steel plate (weighing approximately 34 Kg) which was atop a rigid steel structure 1,52 meters high. This arrangement provided excellent isolation from vibrations transmitted through the floor. Unfortunately it was less than satisfactory in controlling vibration transmitted along the steel tubing. Accordingly, further measures were taken to eliminate transmitted vibrations. Flexible stainless steel sections (Cajon number 321-X16-6) were installed at four strategic points in the loop. Two were placed at the outlet and inlet of the circulator and two others in the downward vertical leg of the loop 80 diameters before and 15 diameters after the test section. As a final measure, the lower horizontal section of the loop, adjacent to the two phase flow meter was fitted with a 136 Kg concrete jacket, 15.24 cm square and 1.82 meters long. No vibration could be discerned in the test section even though a considerable number of large motors were running only 4-1/2 meters away.

It was found that some modification of the standard DISA supplied optical components was required for our particular application. In order to reduce the size of the measuring control volume a 3X spectra physics beam expander was attached to the head of the spectra physics model 120 5mw Helium Neon laser (the reasons for desiring a smaller measuring volume are discussed later).

In order to use the DISA supplied 150 micron pin-hole aperature with the beam expander it was necessary to provide the photomultiplier with

some additional magnification (approx. 2X). A Spirolite macrovar adjustable closeup lens was used for that purpose. The adjustment capability of the closeup lens was extremely useful in focusing the optics.

All measurements were made using differential mode with a beam intersection angle of 14°. Using a Gaussian light intensity based on a $1/e^2$ distribution the salient parameters in Figure 3 are calculated as

$$4\sigma = \frac{4}{\pi}\frac{fo\lambda}{4\sigma_L} = 38\mu m \tag{1}$$

$$4\sigma_p = \frac{fp}{fs}\ 4\sigma = 135\mu m \tag{2}$$

This gives a measuring volume of

$$V_m = \frac{\pi}{3}\left(\frac{(4\sigma)}{\sin\theta}\right) = .00067mm^3 \tag{3}$$

with dimensions

$$\ell = \frac{2\cdot 4\sigma}{2\sin\theta/2} = 311.6\mu m \tag{4a}$$

$$w = \frac{2\cdot 4\sigma}{2\cos\theta/2} = 38.3\mu m \tag{4b}$$

This results in a fringe spacing of

$$d_f = \frac{\lambda}{2\sin\theta/2} = 2.59\mu m \tag{5}$$

The Doppler frequency is

$$F_D = V\,\frac{2\sin\theta/2}{\lambda} \tag{6a}$$

This can be combined with the fringe spacing equation (5) to yield

$$F_D = V/d_f \tag{6b}$$

Equation (6b) relates the Doppler frequency (F_D) with the fringe spacing (d_f) and particle velocity (V). It is thus apparent that changing the beam intersection angle will result in a corresponding change in Doppler frequency. Durst and Whitelaw (1970) in their paper on optimization of optical anemometers discuss the factors which adversely affect fringe anemometers. The two most important factors are vibration of the optics and differences in light intensity of the two intersecting beams. Mechanical vibrations tend to blur the fringes as do differing beam intensities. This blurring results in decreased Doppler signal amplitude. In the system used in this study the intensities of the intersecting beams was carefully measured and controlled using a laser power meter. The methods used to eliminate system vibration have already been discussed.

The signal from the photomultiplier was fed directly to the DISA tracker for processing. The combination of beam intersection angle (14°) and flow velocity required that the DISA tracker be operated on its highest range (5-15MHz). It was found that for the particular signal/noise ratio which was obtained in the experiments, the DISA tracker was unable to track the Doppler signal in its highest range. Therefore, some modifications to the DISA tracker had to be made by the DISA technicians. Basically, the modifications involved adjustment in the time constants of the frequency locked loop. After these modifications the tracker proved to be marginally satisfactory for the measurements made. A spectrum analysis of the photomultiplier output

was obtained using a Hewlett Packard model 141B spectrum analyzer. The spectrum analyzer proved to be indispensable because it allowed for a continuous visual check on the tracker output frequency. This was found to be necessary in our experiment since the DISA tracker would track the fluorescent light and other noise present in the laboratory. Fine tuning of the optics was greatly simplified using the spectrum analyzer. It was only necessary to peak for maximum display height on the spectrum analyzer. The output of the tracker was monitored in several ways. A digital frequency readout was obtained using a Hewlett Packard model 5302A frequency counter. RMS and DC voltages were obtained using DISA models 55D35 and 55D30 voltmeters. (The RMS voltage is proportional to the fluctuating velocity and the DC voltage to the mean velocity.) A Tektronix model 503 oscilloscope provided a visual indication of the turbulence fluctuations (RMS voltage). A check of the signal quality and system alignment was done using a 500 MHz Tektronix series 7000 oscilloscope. Without the spectrum analyzer and 500 MHz oscilloscope it would have been even more difficult to obtain any meaningful measurements near the tube wall. The ability to fine tune the optics visually proved to be invaluable.

The problems inherent in using a laser anemometer near a solid boundary with sub-micron scattering particles have already been well documented, (Berman and Dunning 1973, George and Lumley 1973, George and Berman 1973). The problem of gradient broadening which is caused by having a finite measuring volume in regions of high velocity gradient is a particularly serious one. In our particular application this is coupled with the need to obtain a well-modulated signal using relatively large particles (22μm and 36μm). The choice of beam intersection angle θ

was based on a compromise between the two above considerations. Large values of θ produced smaller gradient broadening effects with a corresponding reduction in signal quality. Small angles yielded well modulated signals but there was a serious gradient broadening problen near the tube wall. The difficulty of making meaningful measurements near the wall was further compounded by the fact that particles adhered to the walls of the tube due to electrostatic effects. This was alleviated to some extent by covering the glass test section with aluminum foil, leaving only a small uncovered area to admit the laser beams and thus providing a good ground.

Initially we expected to make simultaneous gas and particle mean velocity and turbulence measurements using the laser Doppler system by introducing sub-micron particles into the gas together with the large particles. Theoretically two separate Doppler signals should be produced, one for the large particles and one for the sub-micron particles which follow the gas motion. In practice we found that the difference in gas and particle velocity was so small that we could not separate the two Doppler signals.

3. MEAN VELOCITY PROFILES

Mean velocity profiles were taken in clean air seeded with submicron graphite particles using the laser Doppler anemometer and compared with measurements taken with the fiber-film anemometer. These results are shown by the curves in Figure 5 which present a least squares fit of all of the data points taken in the gas Reynolds number range between 13,000-22,000. In this small Reynolds number range the effect of gas Reynolds numbers is negligible. The two curves are practically identical indicating that the laser Doppler system was working properly. However, we were unable to track the laser signal closer than 0.51mm from the wall which essentially negated the expected advantage of the laser system in the vicinity of the wall.

Mean velocity profiles for suspension flow were taken in the vertical test section simultaneously with the laser system and the fiber-film probe as a function of particle loading ratio. A typical result is shown in Figure 6 which indicates that the velocity profile of the particles (as measured with the laser) is the same at the tube centerline but starts lagging the velocity profile of the gas (as measured with the fiber-film) as the wall is approached. Figures 7 and 8 show a series of gas and particle velocity profiles taken at different loading ratios for the #380 (36μm) particles with the clean air velocity profile as a comparison. Figure 7 indicates that the gas velocity profile becomes flatter in the core as the loading ratio is increased indicating greater turbulence in the core region. Although no data was taken in the near wall region ($y/R < .05$) it appears that the gas velocity profiles U_{fs}/U_c in the presence of the particles will cross the clean air profile U_{fo}/U_c providing a lower velocity gradient at the wall

which results in drag reduction. A similar result was predicted by Boothroyd (1966) based on a combination of experimental and theoretical arguments and is reproduced in Figure 9.

Figures 7 and 8 have been replotted in terms of the dimensionless variables u^+ and y^+ in Figures 10 and 11. Figure 10 shows that the velocity profile curves in the presence of the particles are parallel to the clean air curve indicating that the von Karman constant and hence the gas mixing length remains the same although the data points in the buffer region deviate from the straight lines further away from the wall as the loading ratio is increased. This implies that the buffer layer has shifted outward in the presence of the particles. Figure 11 shows that the velocity profile curves of the particles, on the other hand, do not remain parallel to that of the clean air indicating a higher von Karman constant and smaller particle mixing length. This behavior was expected because of the measured slip between the particles and gas (see Figure 6).

Similar results were obtained for the smaller #279 (22μm) particles and are shown in Figures 12 and 13. The gas velocity profiles in the presence of the particles are even flatter than for the #380 particles although the loading ratios are lower, indicating that the smaller #279 particles cause a greater turbulence production in the core region.

4. TURBULENCE INTENSITY PROFILES

Longitudinal turbulence intensity profiles $\sqrt{u_1^2}/U_{fo}$ were taken in the clean air with the laser Doppler system at two gas Reynolds numbers as shown in Figure 14. The turbulence intensity, unlike the mean velocity profiles are strongly dependent on the gas Reynolds number in the Reynolds number range of our data. Similar measurements (not plotted) were taken with the fiber-film probes (Rasmussen, 1966) and gave much lower values. These results indicated that the fiber film probes were much less sensitive to the higher frequency turbulent fluctuations than the laser Doppler system. In order to remove the effect of gas Reynolds number and also probe sensitivity all subsequent turbulence intensity measurements were recalculated as ratios of suspension turbulence either $\sqrt{u_1^2}/U_{fs}$ or $\sqrt{v_1^2}/U_p$ divided by clean gas turbulence for each measured Reynolds number and measurement technique used. Figure 15 is a plot of this ratio for the gas phase based on measurements using the fiber-film probe for the #279 particles at two different loading ratios. The figure shows the gas turbulence intensity ratio to rise in the presence of particles especially as the wall is approached. Figure 16 is a plot of this ratio for the particles measured by the laser system for both the #380 and #279 particles at two different loading ratios. The results for the particles are similar to those for the gas although the turbulence intensity ratios are even higher. At first glance, these results seem anomolous since the particle fluctuating velocity should at best approach the eddy fluctuating velocity. However, since the turbulent fluctuations u_1 are scaled with the mean velocity and the particle mean velocity U_p always lags the mean gas velocity, U_{fs}, one must be careful in comparing Figures 15 and 16. This same behavior of higher particle

turbulent intensities was observed by Carlson (1973) who also made laser Doppler measurements using clean air and 22μm particle suspension flow. Carlson attributes the effect mainly due to the fact that the particles are not all of uniform size and therefore moving at different velocities causing a positive contribution to the intensity of turbulence measurements.

5. DRAG REDUCTION RESULTS

The total measured pressure drop across a pipe test section conveying a gas-solids suspension can be expressed as:

$$\Delta P = \Delta P_{ag} + \Delta P_{ads} + \Delta P_{hg} + \Delta P_{hds} + \Delta P_{fg} + \Delta P_{fds} \qquad (7a)$$

Note that three terms appear in equation 7a that would not appear for a uniform fluid: ΔP_{ads} (which can be negative) is associated with the energy required by the gas to accelerate the solids to a steady velocity relative to the gas velocity, ΔP_{hds} (which also can be negative) is associated with the static head of solids in a vertical pipe, and ΔP_{fds} (which is always positive) is associated with the energy required to overcome direct contact friction between particles and between particles and the wall and the energy required to keep the particles in suspension. ΔP_{fds} has not been divided into two separate terms because it is not possible to separate the terms either by measurement or analysis. The same is true about the two terms ΔP_{fg} and ΔP_{fds} and the simplification:

$$\Delta P_{fs} = \Delta P_{fg} + \Delta P_{fds} \qquad (7b)$$

must be used.

In some correlations ΔP_{fg} is assumed to be identical to the frictional pressure drop of a clean gas and calculated by standard correlations. ΔP_{fds} is then calculated as the additional pressure drop required for the conveyance of particles. This scheme is quite acceptable provided the solids increase the frictional pressure drop. However, negative frictional pressure drops will result from this correlation method under drag reducing conditions. Therefore, one should not consider gas or solids contributions separately but only ΔP_{fs} in evaluating data obtained under drag reducing conditions.

For the optimum conditions for evaluation of drag reduction, the non-frictional pressure drops should be negligible or rigorously accounted for in the experimental data analysis. The gas acceleration term can be eliminated in the experimental setup by insuring that the flow is fully developed and isothermal in the test section. If the residence time in the entrance region to the test section is sufficiently long, the solids acceleration term can also be neglected. The static head terms cannot be avoided in a vertical test section; however, they can be rigorously accounted for by:

$$\Delta P_{hg} = \rho_g g L \; ; \; \Delta P_{hds} = \rho_{ds} g L \tag{7c}$$

Since the loading ratio $\eta = \rho_{ds}\bar{V}_p/\rho_g\bar{U}_p$, equation 7c can be replaced by:

$$\Delta P_h = \Delta P_{hg} + \Delta P_{hds} = \rho_g g L(1 + \eta\bar{U}_g/\bar{V}_p) \tag{7d}$$

If the slip velocity between the particles and gas is small

$$\Delta P_h \simeq \rho_g g L(1 + \eta) \tag{7e}$$

For a single phase incompressible fluid in a hydraulically smooth pipe, the friction factor is calculated from the Blasius equation

$$f_g = \frac{2\Delta P_{fcg}\, D}{\rho_g \bar{U}_g^2 L} \tag{8a}$$

and is a function of the Reynolds number. For a gas-solids suspension, the question arises as to the interpretation of quantities such as density, viscosity, and mean velocity in the Blasius equation - are these gas or suspension properties? Since the two-phase mixture does

not behave like a single phase fluid having the properties of the suspension, the simplest and most logical procedure is to use the gas properties as this provides a direct measure of the gas behavior both before and after the addition of particles. Thus, the suspension friction factor is defined as

$$f_s = \frac{2\Delta P_{fs} D}{\rho_g \overline{U}_g^2 L} \tag{8b}$$

Figures 17 and 18 show the friction factor ratios f_s/f_g plotted versus loading ratio for each particle size in both the vertical and horizontal test section. The friction factor ratio f_s/f_g is equivalent to the pressure drop ratio $\Delta P_s/\Delta P_{cg}$ as defined in Kane et al (1973). As can be seen, both the #279 (22μm) particles and #380 (36μm) particles gave significant drag reduction in vertical flow. In horizontal flow the #279 (22μm) particles still provided some drag reduction while the #380 (36μm) particles produced a drag increase. This is in agreement with the results reported in Kane et al (1973). This is probably due to the gravity effects which were observed visually in the high speed motion pictures.

6. MOTION PICTURE RESULTS

High speed motion pictures were taken in both the vertical and horizontal glass sections at the two solids loading ratios where we obtained maximum drag reduction, i.e., $\eta = 0.59$ for the #279 (22μm) glass beads and $\eta = 1.91$ for the #380 (36μm) glass beads. The film used was Kodak 2484 negative type so that the regions of high particle concentration appear light. The test section was backlighted through a frosted glass plate to minimize reflections. The depth of field was controlled such that the entire test section was in focus.

The film of the vertical test section showed that the flow was essentially uniform for both particle sizes especially in the near wall region. The #279 (22μm) glass beads produced a sporadic clustering of particles which were randomly distributed throughout the tube cross section. The larger #380 (36μm) glass beads did not exhibit this cluster type flow but instead appeared to flow in streamers mainly in the center of the tube.

The behavior of the suspension flow in the horizontal section was markedly different for both particle sizes. The flow of the #279 (22μm) glass beads appeared essentially uniform in the upper portion of the tube with a thin dense layer of particles along the bottom of the test section. Turbulent bursts which appeared to eject particles from the bottom dense layer into the main flow were clearly visible. The flow of the #380 (36μm) glass beads was similar to that of the smaller particles but the dense layer of particles at the bottom of the tube was considerably thicker giving the appearance of dune-like formations. This undoubtedly was the cause of the large drag increase observed for the #380 (36μm) glass beads in the horizontal section (see Figure 15).

The horizontal flow for both particle sizes was clearly affected by gravity settling. A narrative of the complete film describing the various flows is given in Appendix A.

7. THEORETICAL CONSIDERATIONS AND DISCUSSION

The most intriguing new results of the present series of experiments are the radial extent of the measured slip between the gas and particulate phases and the observation in Figures 10 and 11 that the von Karman constant for the gas phase is unaffected by the particles, whereas the solid phase, while it still obeys a logarithmic profile outside the buffer layer and, hence, a linear mixing length relation, exhibits a change in the proportionality constant as a function of particle loading.

Previous theoretical models (Jotaki and Tomita, 1971) and Kane et al (1973) which have attempted to explain the basic drag reduction mechanism in terms of the Stokesian dissipation between particle and eddy, have assumed that significant slip between the two phases is confined to a thin region of the order of the buffer zone. These models which were based on the use of a Townsend-Bakewell eddy showed that the amount of viscous dissipation in the buffer layer needed to produce the measured amount of drag reduction required slip velocities which are an order of magnitude larger than u^*. These results suggested that significant slip velocities of the same order as the mean flow might be occurring at the wall. The present experiments indicate that large slip velocities of this nature are not generated and that the relative motion between the two phases appears to vanish as the wall is approached. The interesting qualitative observation, see, for example, Figure 6, is that a significant slip of the order of u^* between the mean profiles extends well into the core (up to $y/R \approx 0.5$) and a value of y^+ equivalent to approximately 10 buffer layer thicknesses. The integrated viscous dissipation due to particle slip across this much thicker region is thus of the same order as that calculated by Kane et al (1973) using a much

thinner buffer layer model with much larger slip velocities.

The obvious, but crucial question, which arises is whether the slip between the mean profiles arises from the local particle-eddy interaction or from the turbulent bursts that originate at the edge of the laminar sublayer as observed by Kline et al (1959, 1967), Clark and Markland (1970), Grass (1971), Corino and Brodkey (1969), and others. To answer this question we shall construct a simple but qualitatively adequate model to determine how far a typically 20-40μm particle can be injected into the flow by a turbulent burst in the range $5 < y^+ < 15$ where the measurements by Laufer (1954) have shown the values of $\sqrt{u_1^2}$ to rise rapidly to a maximum and the fluid to experience maximum accelerations. Before starting this theoretical development we note that the Stokes relaxation time $t_s = d^2/18\nu\ (\rho_s/\rho + 1/2)$ including the virtual mass effect for the 36μm particles used in the present study is approximately 10^{-2} sec. The characteristic time $t_e = \nu/u^{*2}$ for a fluid eddy with velocity u* to cross the sublayer is only about 3×10^{-5} sec. using a typical value for u* of 2.3 found in our current experiments. This is in contrast to sub-micron particles which closely follow fluid fluctuations. The glass beads in the present study will traverse an eddy at the edge of the sublayer in roughly two to three orders of magnitude less than that required to establish velocity equilibrium with the eddy. In problems of this nature the Basset force due to the unsteady boundary layer on the particle may be much more important than the Stokes drag force. If a particle fluctuation of O(u*) can be created by this short duration unsteady force then the particle will subsequently travel a distance of order u^*t_s before its motion decays. For the 36μm particle just considered u^*t_s is about 0.5 cm and thus a significant fraction of

the pipe radius.

In accord with the above remarks we shall now construct a simple model in which a particle is first subject to a normal fluctuation u_2 due to the passage of an eddy on the time scale t_e and then undergoes a Stokes relaxation on the time scale t_s. The equation governing the interaction between the particle and the eddy is derived in Tchen (1947)

$$\frac{\pi d^3}{6}\rho_s\frac{d\vec{v}}{dt} = 3\pi\mu d(\vec{u}-\vec{v}) + \frac{\pi d^3}{12}\rho\frac{d}{dt}(\vec{u}-\vec{v}) + \frac{\pi d^3}{6}\rho\frac{d\vec{u}}{dt}$$

$$+ \frac{3d^2}{2}\sqrt{\pi\rho\mu}\int_o^t (\frac{d\vec{u}}{dt}-\frac{d\vec{v}}{dt})\frac{dt}{\sqrt{t-t'}} \tag{9}$$

Here $\vec{u}$ and $\vec{v}$ are the fluid and particle fluctuation velocities, $d\vec{u}/dt$ and $d\vec{v}/dt$ are the Eulerian derivatives for the fluid and particle acceleration respectively and the other symbols have their usual meaning. The forces on the right hand side of (9) are the Stokes drag, the virtual mass force, the fluid inertia force and the Basset force. Tchen (1947) sought a solution of (9) in the limit $t_s << t_e$. This limit where a particle performs small undulations within a given field eddy is the opposite extreme to that considered herein.

To determine the magnitude of each of the terms in (7) we introduce the following dimensionless variables

$$\tau = t/\frac{\beta d^2}{18\nu} \quad \vec{u}^+ = \frac{\vec{u}}{u^*} \quad \vec{v}^+ = \frac{\vec{v}}{u^*} \quad \beta = \frac{\rho_s}{\rho} + \frac{1}{2} \tag{10}$$

where $t_s = \beta d^2/18\nu$ and rewrite equation (9) as

$$\frac{d\vec{v}^+}{d\tau} = \vec{u}^+ - \vec{v}^+ + \frac{3}{2\beta}\frac{d\vec{u}^+}{d\tau} + \frac{3}{\sqrt{2\pi\beta}}\int_o^\tau \frac{d\vec{u}^+}{dt'} - \frac{d\vec{v}^+}{dt'}\frac{dt'}{\sqrt{\tau-t'}} \tag{11}$$

For glass beads $\beta \approx 2000$. Thus the fluid inertia force can be neglected in comparison with the Basset force even if the fluid acceleration is large and occurs on a time scale $t_e << t_s$ for which $\tau << 1$. The particle acceleration in the Basset force integral will be small compared to $d\vec{u}^+/dt'$ since it is responding passively to the fluid fluctuation and has greater inertia. The y^+ (normal) component of equation (11) thus simplifies to

$$\frac{dv_2^+}{d\tau} + v_2^+ = u_2^+ + \frac{3}{\sqrt{2\pi\beta'}} \int_o^\tau \frac{du_2^+}{dt'} \frac{dt'}{\sqrt{\tau - t'}} \tag{12}$$

One now needs to develop a model for the u_2^+ fluctuation at the edge of the sublayer. From Laufer's (1954) data it is observed that the growth of the u_1^+ fluctuation up to $y^+ \approx 12$ is nearly linear with y. Simple continuity considerations thus dictate an expression for u_2^+ of the form

$$u_2^+ = \alpha y^{+2} \tag{13}$$

Matching (13) with Laufer's (1954) data yields a value for $\alpha = .005$. If (13) is now differentiated with respect to the dimensionless (time to cross sublayer) short time $t^* = t/\frac{\nu}{u^{*2}}$ and y^+ and its derivations are expressed in terms of u_2^+, one obtains

$$\frac{du_2^+}{dt^*} = 2\sqrt{\alpha}\, u_2^{+3/2} = 2\alpha^2 y^{+3} \tag{14}$$

One observes that for $y^+ > 15$ the dimensionless normal acceleration du_2^+/dt^* resulting from the burst of the eddy is of order unity. The dimensionless acceleration on the time scale t_s, $du_2^+/dt' = du_2^+/dt^* (t_s/t_e)$, which appears in the Basset force integral in (12) is thus of $O(t_s/t_e)$ and large compared to unity as anticipated.

For values of y^+ in the range $5 < y^+ < 15$, the streamwise fluctuation u_1^+ is considerably larger than u_2^+ with the result that a fluid eddy will pass over a particle nearly horizontally. Corino and Brodkey (1969) observe that the average burst angle is about 8 degrees. This and the fact that the characteristic lifetime of the particle in the eddy $t_e << t_s$ permit one to treat the fluid acceleration as constant in the Basset force integral for the duration τ_e of the particle eddy interaction even though the y^+ location of the particle does change slightly as a result of the interaction. With this approximation equations (12) and (14) can be combined to give

$$\frac{dv_2^+}{d\tau} + v_2^+ = u_2^+ (y^+) \left(1 + \frac{6\alpha y^+}{\sqrt{2\pi\beta'}} \frac{t_s}{t_e} \int_o^{\tau_e} \frac{dt'}{\sqrt{\tau - t'}}\right) \tag{15}$$

Equation (15) can be integrated analytically for $\tau << 1$ using series expansion techniques. The two leading terms of this series solution which satisfies the initial condition $v_2^+ (0) = 0$ are

$$v_2^+ (y^+, \tau_e) \quad u_2^+ (y^+)$$

$$v_2^+ (y^+, \tau_e) = u_2^+ (y^+) \tau_e \left(1 + \frac{2}{3} \sigma y^+ \tau_e^{1/2} + O(\tau_e)\right) \tag{16}$$

$$\sigma = \frac{12\alpha}{\sqrt{2\pi\beta'}} \frac{t_s}{t_e}$$

σ for our 36μm particle has the value .074. τ_e is approximately given by $.4y^+/u_1^+ (t_e/t_s)$ where we have used the Prandtl mixing length as representative of the eddy size. At $y^+ = 12$ the second term in (16) is about 10 percent of the leading term. The normal acceleration of the fluid eddy is thus not large enough for the Basset force to dominate the particle-eddy interaction.

From equation (16) the particle upon exiting from the eddy has a dimensionless normal velocity $u_2^+ (y^+) \tau_e$. We now assume that the particle is free to dissipate its acquired kinetic energy before encountering another burst from the sublayer. Equation (12) for this motion simplifies to

$$\frac{\partial v_2^+}{\partial \tau} + v_2^+ = 0; \tau > \tau_e \tag{17}$$

Solving for v_2^+ and integrating to find the normal particle displacement at time τ one obtains

$$y^+ - y_e^+ = v_2^+ (y_e^+, \tau_e) e^{\tau_e} (1 - e^{-\tau}) \frac{t_s}{t_e} \tag{18}$$

The total displacement as $\tau \to \infty$ is

$$y^+ - y_e^+ = u_2^+ (y_e) \tau_e \left(\frac{t_s}{t_e}\right) \tag{19}$$

Result (19) is the dimensionless particle mixing length ℓ_p^+. In dimensionless terms $\ell_p = u_2 \ell / |\vec{u}-\vec{v}|$ where ℓ is the fluid mixing length.

It is evident from the above approximate result that the particle and fluid mixing lengths are of the same order with ℓ_p being a little less than ℓ since u_2 in general is somewhat less than $|\vec{u}-\vec{v}|$ throughout the boundary layer. At first glance this seems rather surprising since the fluid eddy passes right over the particle transferring only a small portion of its disturbance velocity to the latter. However, the same difficulty that the fluid eddy has encountered in accelerating the particle is also encountered in arresting its motion with the result that the particle and the fluid eddy travel comparable though not exactly equal distances. This behavior is fundamental to understanding

the basic drag reduction mechanism. Particles ejected by bursts from the sublayer like the eddies which accelerated them terminate their trajectories in the buffer zone. The slip between the two phases is not due to low momentum particles from the wall region penetrating the flow in the core of the pipe, but rather from the local interaction of the particles with the eddies as described below.

The simple model just described for the eddy's particle interaction at the edge of the sublayer can with minor modification be applied at any point in the flow. The principal result is that a particle will move a normal distance $u_2 t_i$ as a result of an interaction with an eddy, where t_i is the interaction time for the eddy to traverse the particle. The slip between the two phases is due to the fact that average value of $\overline{u_2 t_i}$ does not vanish even though $\bar{u}_2 = 0$ by definition. The reason for this is that the average interaction time for a particle moving radially inward towards the core (upburst phase) is considerably greater than a particle at the same y location moving towards the wall (inrush phase). The experimental observations in references 7-11 have now well-documented that a period of upburst is accompanied by a streamwise deceleration in the mean profile ($\partial u_1/\partial x < 0$) and a vertical acceleration of the fluid ($\partial u_2/\partial y > 0$) from local continuity considerations as sketched in Figure 19. Thus if $\vec{U}_1 - U_{gs_1} < 0$ an eddy will move back over the particle if it is behind sketch (a) or overtake the particle if $U_{gs_1} - \vec{u}_1 > 0$ and it is ahead as shown in sketch (b). In either case the time required for a particle to traverse an eddy of dimension ℓ is

$$t_e^{\uparrow} = \frac{\ell}{\sqrt{(U_{gs_1} - u_1)^2 + u_2^2}^{\uparrow}} \tag{20}$$

In contrast a period of inrush is accompanied by a streamwise acceleration of the mean profile ($\partial u_1/\partial x > 0$) and a vertical deceleration of the fluid ($\partial u_2/\partial y < 0$). Thus, in a period of inrush the slip velocity between the mean profiles U_{gs_1} and the fluid fluctuation augment each other. A particle which is behind the fluid eddy will never catch up with it, sketch (c) whereas the eddy will quickly overtake the particle with a relative x velocity component $U_{gs_1} + \vec{u}_1$, if it is ahead, sketch (d). In the latter case the particle eddy interaction time is

$$t_e^{\downarrow} = \frac{\ell}{\sqrt{(U_{gs_1}+u_1)^2+U_2^{2\uparrow}}} \tag{21}$$

The qualitative considerations are still valid in the presence of spanwise flow fluctuations. It is evident from a comparison of equations (20) and (21) that the slip between the two phases serves to augment the particle-eddy interaction time in a period of upburst and to decrease the particle eddy interaction time in a period of inrush. Thus $\overline{u_2 t_e} > 0$ if $U_{gs_1} > 0$. As one proceeds toward the center of the pipe $U_{gs_1} \to 0$ with the result that $t_e^{\uparrow} \to t_e^{\downarrow}$ and $\overline{u_2 t_2} \to 0$.

The second intriguing feature noted earlier is that the fluid mixing length outside the buffer layer ℓ is unchanged by the addition of particles, Figure 10, whereas the particle mixing length ℓ_p decreases as a function of particle loading ratio, Figure 11. The effect of the particles on the gas is principally to thicken the buffer layer by draining energy from the entire flow by the Stokes dissipation that results from the particle slip and to increase the turbulence intensity. From Figures 10 and 11 one concludes that the mean velocity profiles for

the gas and solid phases outside the buffer layer are respectively of the form

$$\frac{U_g}{u^*} = \frac{1}{K} \ln y^+ + G(\eta) \tag{22}$$

and

$$\frac{U_s}{u^*} = \frac{1}{K_s(\eta)} \ln y^+ + G_s(\eta) \tag{23}$$

where one notes that K_s is a function of η but that K is independent of η. The equation for the slip velocity $U_g - U_s$ between the mean profiles is obtained by subtracting (22) from (23).

$$\frac{U_{gs}}{u^*} = \frac{K_s - K}{K_s K} \ln y^+ + G(\eta) - G_s(\eta) \tag{24}$$

In general $K_s < K$ since the particle mixing length ℓ_p is less than ℓ. The slope $(K_s - K)/K_s K$ in a $U_{gs_1}^+$ versus $\ln y^+$ plot is thus negative. The functions $K_s(\eta)$, $G(\eta)$ and $G_s(\eta)$ can all be determined experimentally. Whereas K is independent of η, K_s depends on η since the particle eddy interaction time decreases as the turbulent intensity increases. The effect of particle addition is thus to decrease the particle mixing length.

We conclude this section by examining the magnitude of the slip velocity as a function of tube position y/R for two typical experimental runs as shown in Figure 20. We were able to fit these data points quite closely by using the following approximate analysis to estimate the slip velocity U_{gs_1}. If we assume that a solid particle originally

in equilibrium with the gas flow moves a distance ℓ_p normal to the wall (particle mixing length), then

$$U_{gs_1} = \ell_p \frac{dU}{dy} \tag{25}$$

But we have already shown that $\ell_p = u_2 t_i$. The average lifetime of the particle in an eddy can be approximated by $t_i = \ell / U_{gs_1}$. Therefore,

$$U_{gs_1}^2 = u_2 \frac{dU}{dy} \ell \tag{26}$$

since $dU/dy = u^*/Ky$ and $\ell_g = Ky$, equation 26 becomes

$$U_{gs_1} = \sqrt{u_2 u^*} \tag{27}$$

Assuming u_2 has the same y dependence as the normal component of the Townsend-Bakewell eddy (Kane et al, 1973), i.e.,

$$u_2 = A(1) y e^{-A(2) y^2} \tag{28}$$

combining equations (27) and (28), normalizing y with R and U_{gs_1} with U_c, we obtain

$$\frac{U_{gs_1}}{U_c} = B(1) \sqrt{y/R} \; e^{-B(2)\,(y/R)^2} \tag{29}$$

Equation (29) is plotted as the solid lines in Figure 20. The agreement between the above approximate analysis and the data points is striking. This suggests that eddies exhibiting the structure of the Townsend-Bakewell eddy may exist well beyond the buffer layer.

8. ADDITIONAL RESULTS AND DISCUSSION

A. 38.1 mm Test Section

The inability to obtain meaningful measurements with the laser Doppler system into the buffer region beyond a y^+ of 0.51 mm prompted an investigation into methods of increasing the buffer layer thickness so as to obtain additional data in the near wall region. These data were considered to be important since the crucial mechanism behind drag reduction probably occurs in this region.

An obvious method of increasing the boundary layer thickness, and the method that was adopted, is to increase the diameter of the test section. A tube with an inside diameter twice that used previously (an increase from 22 mm to 38.10 mm inside diameter) was chosen. The downward vertical leg of the loop was modified to accommodate the larger test section. An entry length of 20 diameters was the largest possible because of the finite length of the vertical test section which was fixed due to ceiling height limitations. The pressure drop in the new test section was calculated to be 32 times less than in the old 22 mm I.D. test section. This was roughly equivalent to 2.54 cm of water at maximum circulator speed. In order to measure such small pressure differentials an electronic micromanometer manufactured by Furness Controls, Ltd., Bexhill, England was used. Measurements were made to determine the friction factor versus Reynolds number in clean air flow. The results of these tests are shown in Figure 21. It is obvious that the friction factor curve is much larger than the accepted value for well developed flow in a smooth tube. A similar curve for the 22 mm diameter test section (not shown) reproduced the accepted smooth tube line almost identically. This led to the conclusion that the flow was probably not

fully developed. Confirmation of this suspension was provided by making some gas velocity profile measurements using fiber-film anemometry. One such profile is shown in Figure 22. Also shown is the expected clean gas profile. As can be seen, the profile measured in the 38.1 mm test section is much blunter than predicted by the 1/7 power law. This bluntness further indicated that the flow was not fully developed. Further confirmation was obtained when pressure drop measurements were made with small amounts of glass beads present. For #380 glass beads at a loading ratio of .3, the micromanometer indicated a negative pressure drop in the test section. This is clearly impossible in fully developed flow. Because of space limitation, it was impossible to increase the entrance length and, therefore, these experiments in the 38.1 mm test section were abandoned.

B. Pulsating Flows

The most serious impediment to an application of drag reduction to commercial conveying systems is the relatively small amount of drag reduction achieved in horizontal flow. We obtained less than 10% drag reduction in the horizontal test section for the #279 glass beads (22μm) and a drag increase for the #380 glass beads (36μm). As seen in the high speed motion pictures, the particles tend to segregate in the bottom of the horizontal test section due to gravity settling. This segregation is responsible for the small amount of drag reduction achieved with the 22μm particles and the drag increase observed for the 36μm particles. The movies of the vertical flow indicated a much more uniform dispersal of the solids around the periphery of the test section.

Private communication with Dr. Marcus of the University of the Witwatersrand in South Africa indicated that we could obtain much larger

drag reduction in horizontal sections than we have measured in the past by pulsating the flow. The pulsations apparently would tend to disperse the solid more uniformly through the gas preventing particle separation and sedimentation.

In order to introduce pulsations into our system a diaphragm valve was designed and installed in the upper horizontal section. The valve was driven by an MB model no. C11-D vibration testing head capable of frequencies from 5 to 200 Hz. Movement of the diaphragm resulted in changes in flow area and thus resulted in pulsations in the flow.

The results obtained in this study were inconclusive due primarily to mechanical limitations. Dr. Marcus indicated that he obtained maximum drag reduction at a pulsation frequency of 200 Hz. In his system the pulsations were caused by the positive displacement pump that provided the motive force for circulation. In our system the stroke of the vibration testing head at 200 Hz was limited. The pulsation amplitude obtained at this frequency was, therefore, small resulting in only a minor flow disturbance. In order to measure the frequency and amplitude of the pressure fluctuations two Kistler model 206 low pressure (dynamic) transducers were installed in the loop; one 20 diameters upstream and the other 80 diameters downstream of the test section. The output of the transducers was displayed on an oscilloscope. At 200 Hz pulsations were completely washed out by the turbulence. At lower frequencies, of the order of 40 Hz, it was found that the amplitude of the pulsations was much higher and only a small decrease in amplitude (due to turbulence) was noted at the two transducer locations. It was, therefore, decided to make a series of drag reduction measurements at the lower frequency pulsations (40 Hz) in order to determine if the

pulsations resulted in any further reduction in drag. It was found that our closed loop system had multiple resonance points in the frequency range 10-100 Hz. Because of this it was impossible to obtain any meaningful data at these particular frequencies. Furthermore, no significant differences in pressure drop reading were measured with or without pulsations. Therefore, these experiments were considered inconclusive.

9. REFERENCES

Berman, N.S. and Dunning, J.W., 1973, "Pipe Flow Measurements of Turbulence and Ambiguity Using Laser-Doppler Velocimetry", J. Fluid Mech., 61, 289.

Birchenough, A. and Mason, J.S., 1976, "Particle Wall Velocity Measurements in a Densely Flowing Gas-Solid Suspension", Paper B2, Pneumotransport 3, BHRA Fluid Engng., Cranfield, Bedford, England.

Boothroyd, R.G., 1966, "Pressure Drop in Duct Flow of Gaseous Suspension of Fine Particles", Trans. Instn. Chem. Engrs., 44, T306.

Boyce, H.P. and Blick, E.F., 1970, "Fluid Flow Phenomena in Dusty Air", Trans. ASME, J. Basic Engng., 92, 495.

Carlson, C.R., 1973, "Turbulent Gas-Solids Flow Measurements Utilizing a Laser Doppler Velocimeter", Ph.D. Thesis, Rutgers University.

Carlson, C.R. and Peskin, R.L., 1975, "One-Dimensional Particle Velocity Probability Densities in Turbulent Gas-Particle Duct Flow", Int. J. Multiphase Flow, 2, 67.

Clark, J.A. and Markland, E., 1970, "Vortex Structures in Turbulent Boundary Layers", Aeronaut. J., 74, 243.

Clark, R.H., Charles, D.E., Richardson, J.F. and Newitt, D.M., "Pneumatic Conveying, 1952. Part I: The Pressure Drop During Horizontal Conveyance", Trans. Instn. Chem. Engrs., 30, 209.

Corino, E.R. and Brodkey, R.S., 1969, "A Visual Investigation of the Wall Region in Turbulent Flow", J. Fluid Mech., 37, 1.

Depew, C.A., 1960, "Heat Transfer to Flowing Gas-Solids Mixtures in a Vertical Circular Duct", UCRL 9280, Lawrence Radiation Laboratory, U. of Cal., Berkeley, Calif.

Durst, F. and Whitelaw, J.H., 1971, "Optimization of Optical Anemometers", Proc. Roy. Soc. Lond. A. 324, 157.

Einav, S. and Lee, S.L., 1973, "Measurement of Velocity Distribution in Two-Phase Suspension Flows by the Laser-Doppler Technique", Rev. Sci. Instrum., 44(10).

Farmer, W.M., 1972, "Measurement of Particle Size, Number Density, and Velocity Using a Laser Interferometer", Applied Optics, 11(11).

George, W.K. and Berman, N.S., 1973, "Doppler Ambiguity in Laser Doppler Velocimeters", Applied Research Laboratory.

George, W.K. and Lumley, J.L., 1973, "The Laser Velocimeter and Its Applications to the Measurement of Turbulence", J. Fluid Mech., 60, 321.

REFERENCES (cont.)

Gibson, H.G., Abel, W.T., and Fasching, G.E., 1963, "Meter for Determining Mass Flow of Solids in Multi-Phase Fluids", Proc. Multi-Phase Flow Symp., ASME, Philadelphia, Pa., Nov. 17-22, 1963.

Grass, A.J., 1971, "Structural Features of Turbulent Flow Over Smooth and Rough Boundaries", J. Fluid Mech. 50, 233.

Haertig, J. and Fleck, V., 1974, "Anémométric Laser, Amélioration de la Précision des Mesures par Elimination des Erreurs dues a la Presence de Grosse Particules", ISL - 10/74 also NTIS #N75 16845 H 2/D.

Halstrom, E.A.N., 1953, "Design of Experimental Apparatus for the Study of Two-Phase Flow in Circular Straight Pipe", M.S. Thesis, Princeton U., Princeton, N.J.

Hawes, R.E., Holland, E., Kirby, G.T., and Waller, R., 1964, "An Experimental Investigation Into Heat Transfer and Pressure Drop Properties of Gaseous Suspensions of Solids", Atomic Energy Est. Report AEEW-R244.

Jotaki, T. and Tomita, Y., 1971, "Turbulent Friction Drag of a Dusty Gas", Proc. 1st Int. Conf. on Pneumatic Transport of Solids in Pipes, Paper C5, BHRA Fluid Engng., Cranfield, U.K.

Kane, R.S., Weinbaum, S. and Pfeffer, R., 1973, "Characteristics of Dilute Gas-Solids Suspension in Drag Reducing Flow". 2nd Int. Conf. on Pneumatic Transport of Solids in Pipes, Paper C3, Proc. BHRA Fluid Engng., Cranfield, U.K.

Kline, S.J., Reynolds, W.C., Schraub, F.A. and Rundstadler, P.W., 1967, "The Structure of Turbulent Boundary Layers", J. Fluid Mech., 30, 741.

Kline, S.J. and Rundstadler, P.W., 1959, "Some Preliminary Results of Visual Studies of the Flow Model of the Wall Layers of the Turbulent Boundary Layer", J. of Applied Mech., ASME Series E, 26, 166.

Laufer, J., 1954, "The Structure of Turbulence in Fully Developed Pipe Flow", NACA Tech. Rept. 1174.

Mason, J.S. and Boothroyd, R.G., 1971, "Comparison of Friction Factors in Pneumatically Conveyed Suspensions Using Different-Sized Particles in Pipes of Varying Size", Paper C1, Proc. 1st Int. Conf. on Pneumatic Transport of Solids in Pipes, BHRA Fluid Engng., Cranfield, U.K.

Peters, L.K. and Klinzing, G.E., 1972, "Friction in Turbulent Flow of Solids-Gas Systems", Can. J. Chem. Engng., 50, 441.

REFERENCES (cont.)

Pfeffer, R. and Kane, R.S., 1974, "A Review of Drag Reduction in Dilute Gas-Solids Suspension Flow in Tubes", Paper F1, 1st Int. Conf. on Drag Reduction, BHRA Fluid Engng., Cranfield, U.K.

Rasmussen, C.G., 1966, "Measurement of Turbulence Characteristics", DISA Information No. 3.

Richardson, J.F. and McLeman, M., 1960, "Pneumatic Conveying - Part II: Solids Velocities and Pressure Gradients in a One-Inch Horizontal Pipe", Trans. Instn. Chem. Engrs., 38, 257.

Rossetti, S.J. and Pfeffer, R., 1972, "Drag Reduction in Dilute Flowing Gas-Solid Suspension", AIChE. J., 18, 31.

Schluderberg, D.C., Whitelaw, R.L., and Carlson, R.W., 1961, "Gaseous Suspensions - A New Reactor Coolant", Nucleonics, 8, 67.

Soo, S.L. and Trezek, G.J., 1966, "Turbulent Pipe Flow of Magnesia Particles in Air", Ind. Eng. Chem. Fundamentals, 5, 388.

Sproull, W.T., 1961, "Viscosity of Dusty Gases", Nature, 190, 976.

Stock, D.E., Jurewicz, J.T., Crowe, C.T. and Eschback, J.E., 1975, "Measurement of Both Gas and Particle Velocity in Turbulent Two-Phase Flow", Fourth Biennial Symposium on Turbulence in Liquids, Rolla, Missouri.

Tchen, C.M., 1947, "Mean Value and Correlation Problems Connected with the Motion of Small Particles Suspended in a Turbulent Fluid", Ph.D. Thesis, Delft.

Wachtell, G.P. and Waggener, J.P., 1964, "Flow Stability of Gas-Solids Suspensions," The Franklin Institute Report F-B1938.

10. EXPERIMENTAL EVIDENCE OF DRAG REDUCTION

Reference	Solids Diameter and Type	Pipe Diameter and Orientation	Loading Ratio	Reynolds Number
Clark, et al, 1952	1060μm cress	25.4mm horizontal	1.5-5	12,000-68,000
Halstrom, 1960	115μm glass 177-219μm glass	50.8mm	---	----
Depew, 1960	30μm glass	18.0mm vertical	0-5.0 0-3.5	13,500 27,400
Richardson and McLeman, 1960	1524μm perspex	25.4mm horizontal	0-1.0	12,000-70,000
Schluderberg et al, 1961	1-5μm graphite	13.5mm vertical	0-12.0	20,000-200,000
Sproull, 1961	----	----	0.21	100,000
Hawes, et al, 1964	0-10μm graphite	12.7mm vertical	---	----
Boothroyd, 1966	0-40μm zinc	25-4mm vertical	0-3.0 0-7.0 0-12.0 0-12.0	35,000 53,000 80,000 100,000
		50.8mm vertical	0-2.0 0-2.5 0-2.5 0-2.5	35,000 53,000 80,000 100,000
		76.2mm vertical	0-1.5	80,000
Soo and Trezek, 1966	30μm magnesia	127mm horizontal	0-1.0	130,000-295,000
Boyce and Blick, 1970	2-60μm silica	69.9mm angulated	0-3.5	18,200-63,000
	100μm glass		0-4.0	9,450-63,000
	200μm glass		0-4.0	12,000-63,000
	840μm glass		0-5.0	40,400-63,000
	1680μm glass		0-6.0	13,800-63,000
Mason and Boothroyd, 1971	15,40,70μm alumina	25.4mm vertical	0-6.0 0-4.0	140,000 75,000
	15,40μm alumina 15μm alumina	50.8mm vertical	0-1.0 0-1.0 0-1.0	70,000 85,000 105,000
	15,40,70μm alumina	76.2mm vertical	0-1.5	69,500
Peters and Klinzing, 1972	25μm glass	25.4mm vertical	0.7-1.6	14,000-27,000

Reference	Solids Diameter and Type	Pipe Diameter and Orientation	Loading Ratio	Reynolds Number
Rosetti and Pfeffer, 1972	15μm glass	25,4mm vertical	0-1.5	24,250
	20μm glass		0-0.4	13,150
			0-0.7	16,700
			0-2.0	22,750
	25μm glass		0-0.4	13,000
			0-0.6	16,250
			0-1.8	22,800
	34μm glass		0-0.7	12,000
			0-0.9	15,450
			0-1.5	22,300
	59μm glass		0-0.6	12,500
			0-0.7	16,400
			0-1.0	21,800
	10μm glass	22.1mm	0-1.5	27,700
	20μm glass	horizontal	0-0.4	15,000
			0-0.6	19,100
			0-2.0	25,925
	25μm glass	22.1mm	0-1.0	18,800
		horizontal	0-2.15	25,900
Kane et al, 1973	15μm glass	22.1mm vertical	0-0.9	11,000-23,000
	21μm glass		0-1.0	11,000-23,000
	36μm glass		0-3.0	10,000-24,000
	55μm glass		1.6-3.0	10,000-19,000
	15μm glass	22.1mm	0-0.9	11,000-23,000
		horizontal		
	21μm glass		0-1.0	11,000-23,000

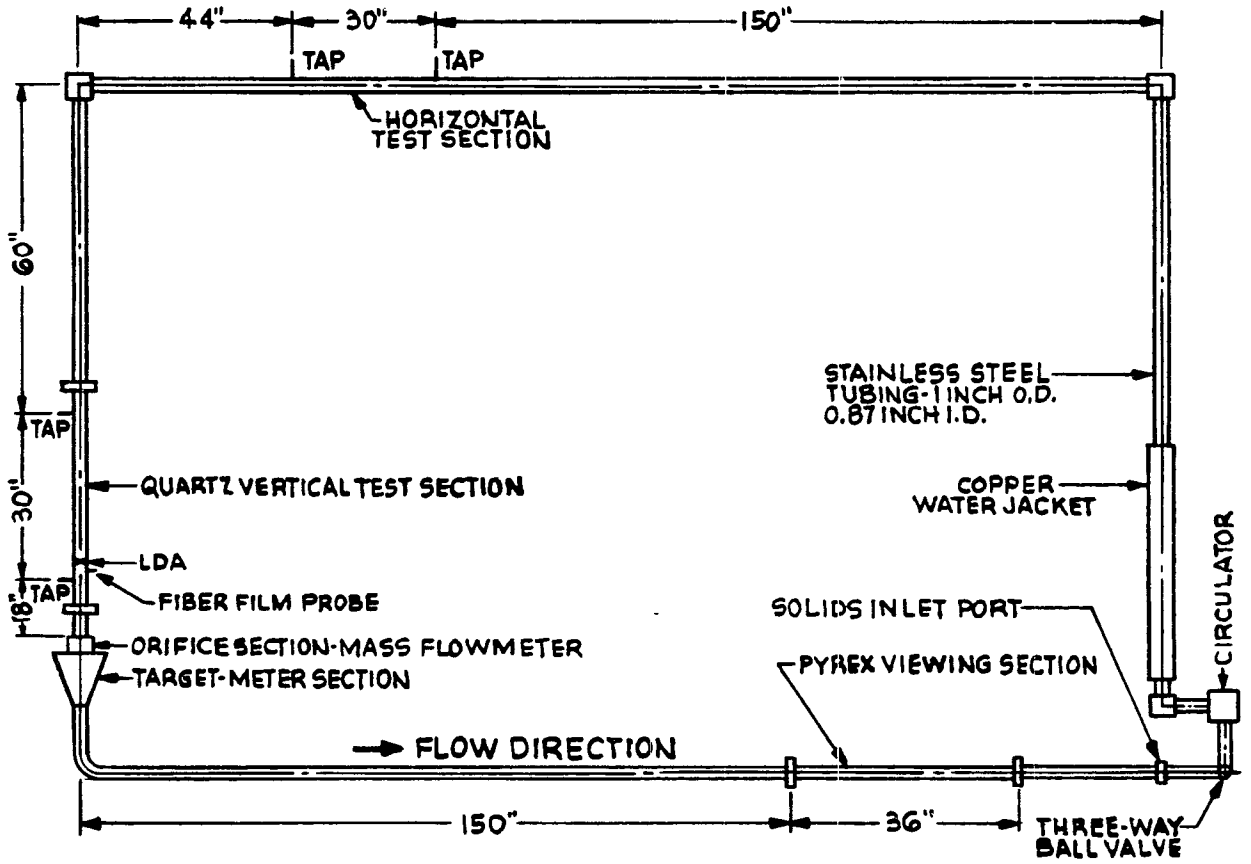

Figure 1. Closed Loop System.

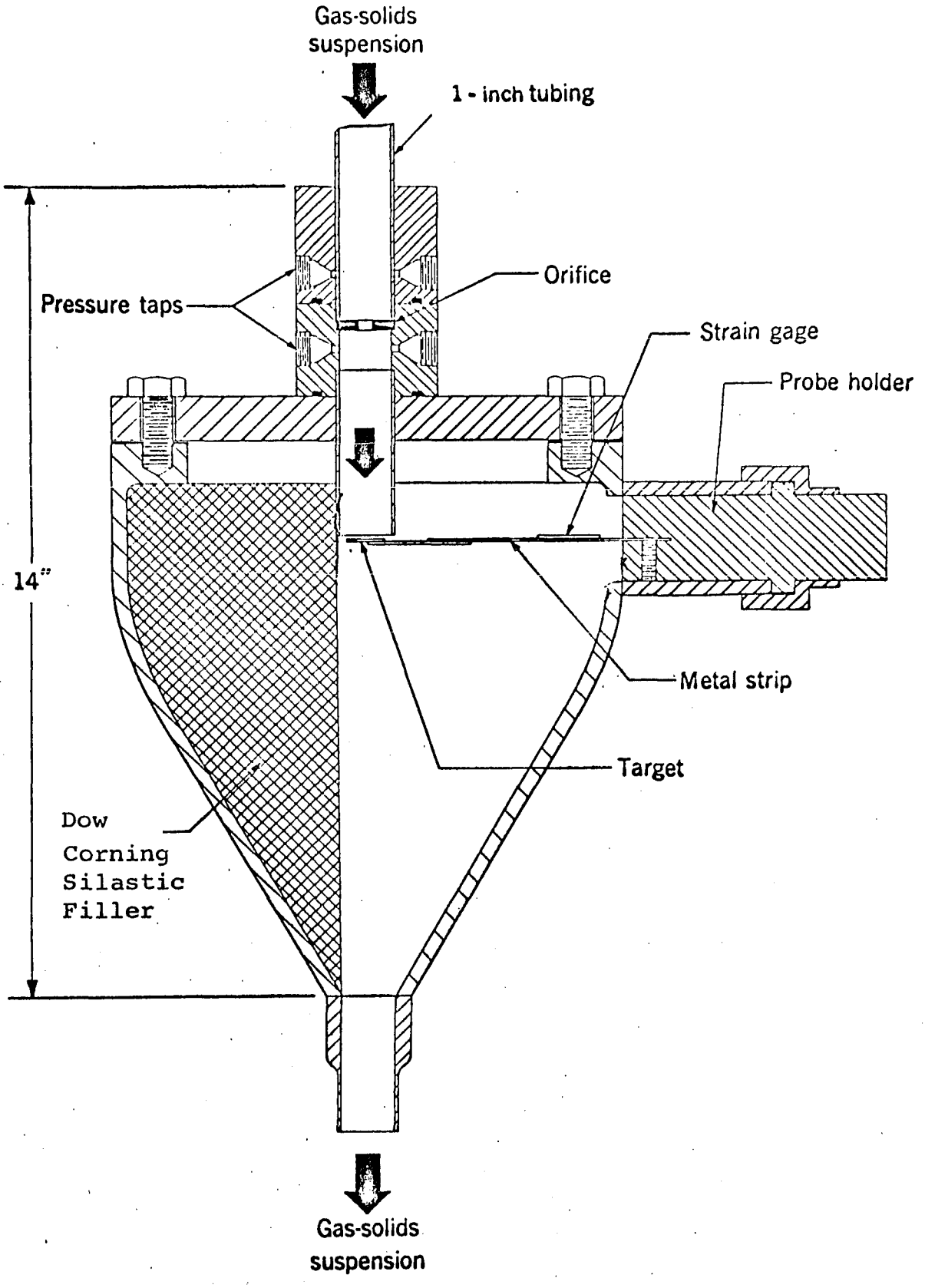

Figure 2. Mass Flowmeter.

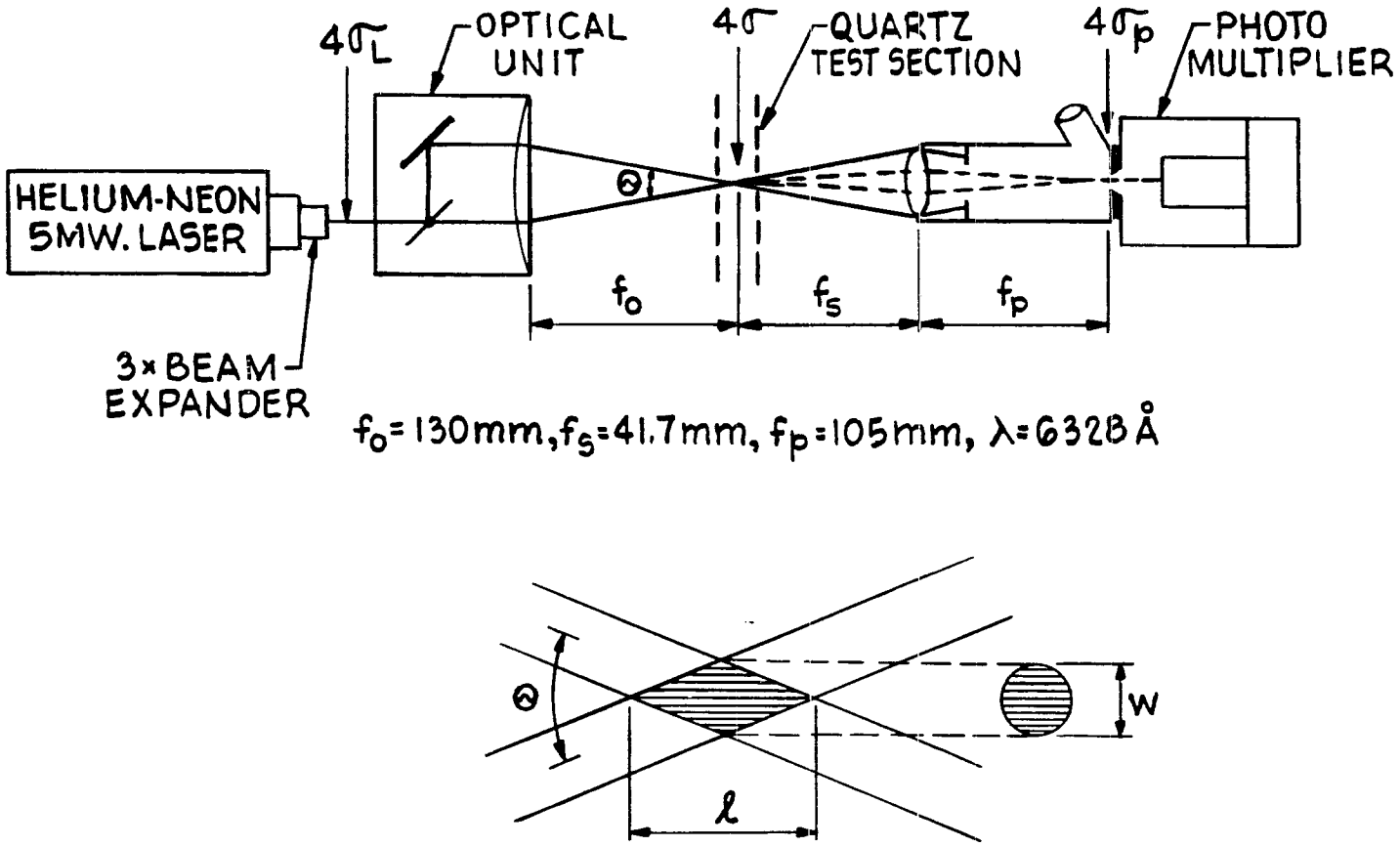

Figure 3. Schematic of the Laser Anemometer Optical Arrangement.

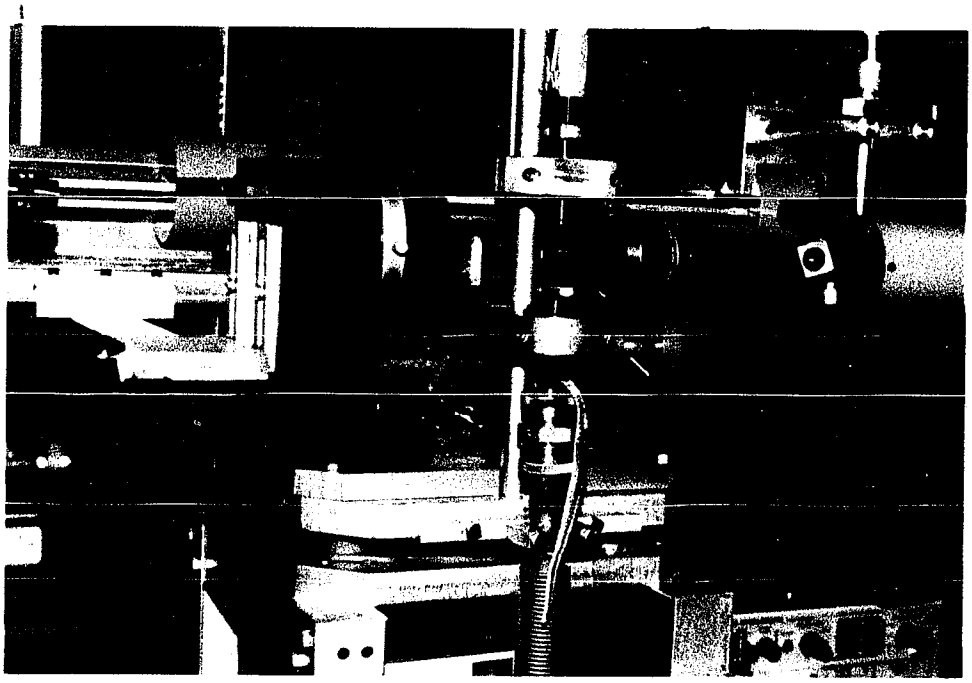

Figure 4. Photograph of the Laser Anemometer Traverse Mechanism.

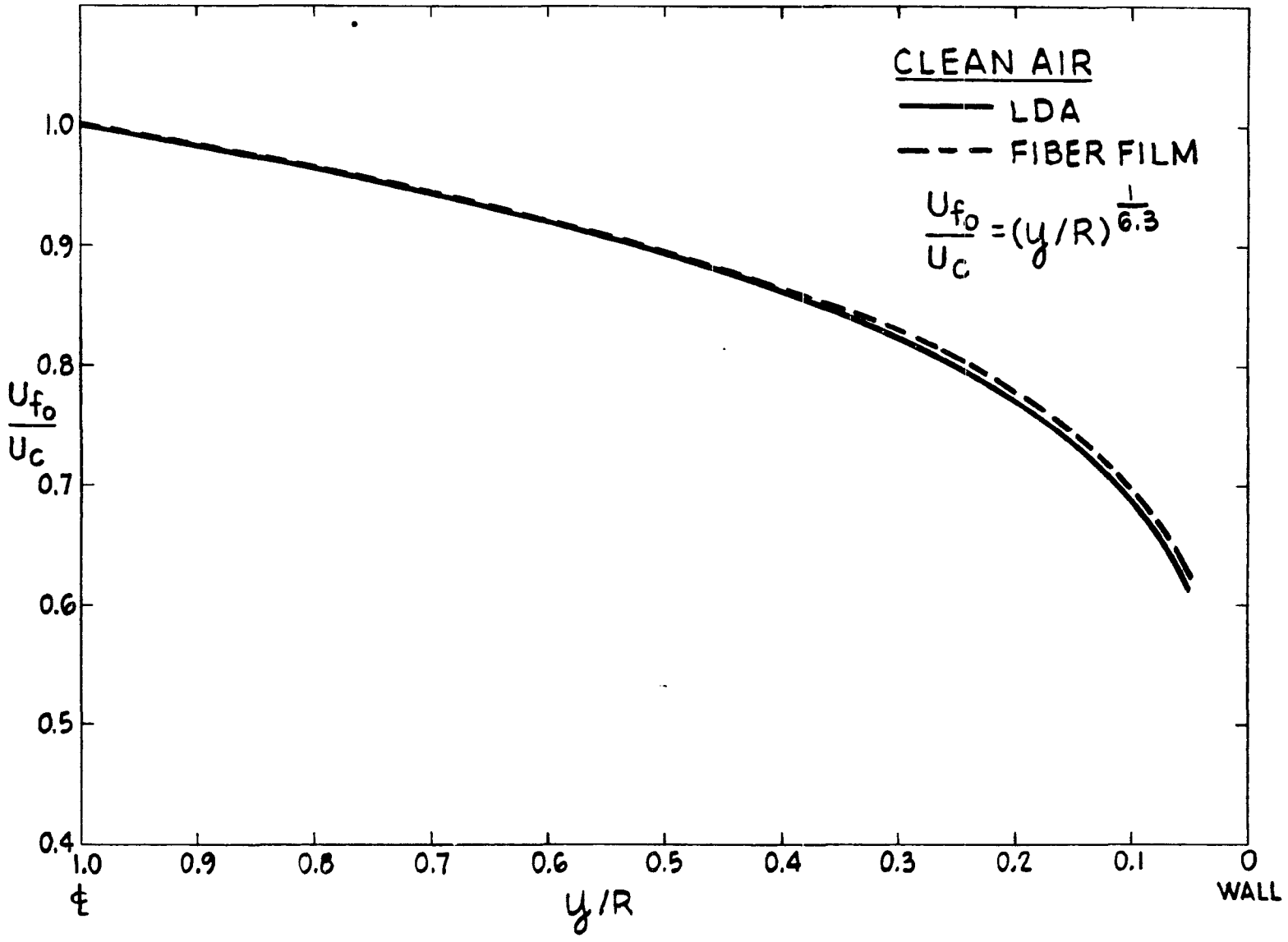

Figure 5. Clean Air Velocity Profiles.

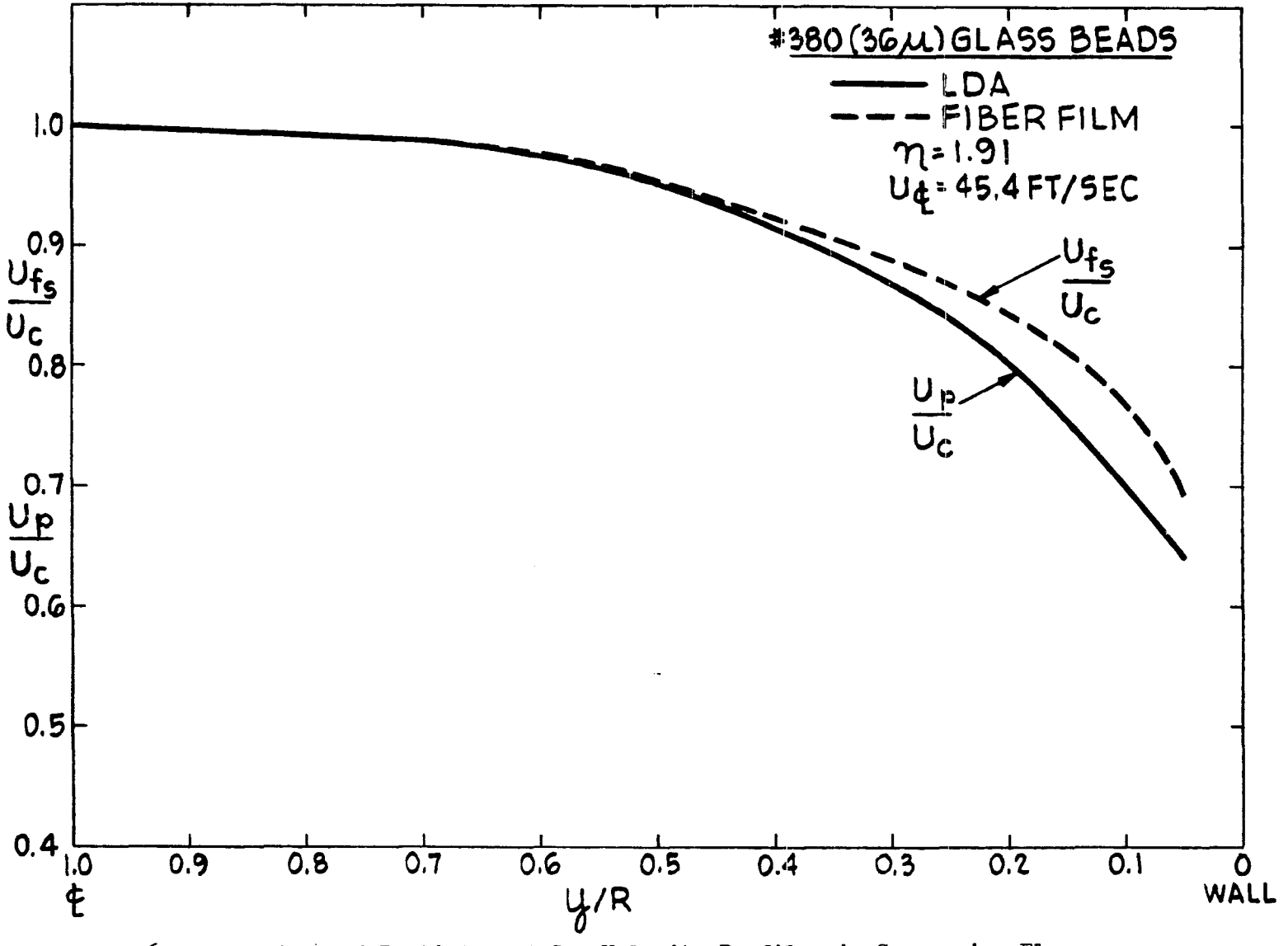

Figure 6. Comparison of Particle and Gas Velocity Profiles in Suspension Flow.

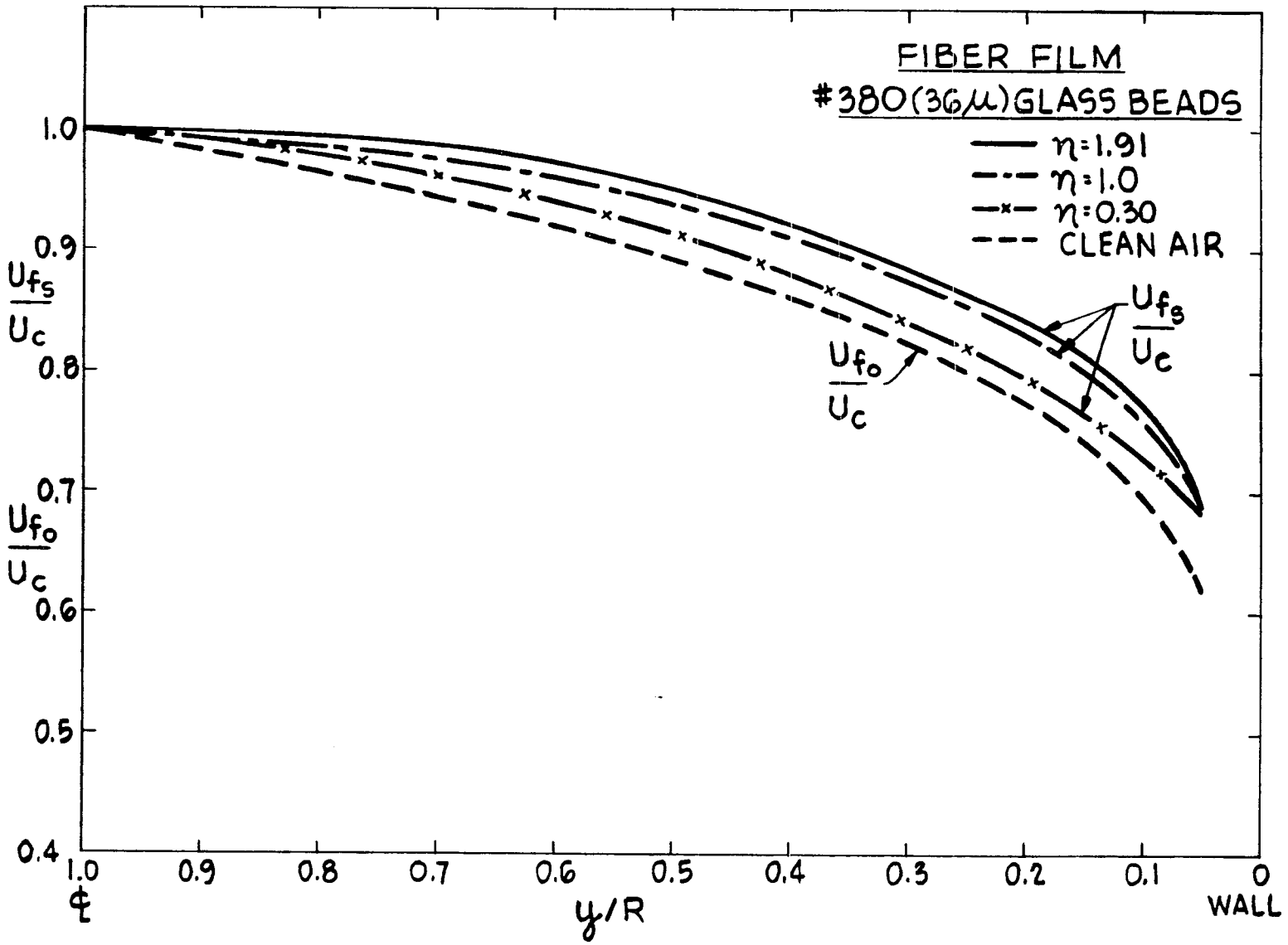

Figure 7. Air Mean Velocity Profiles in Suspension Flow.

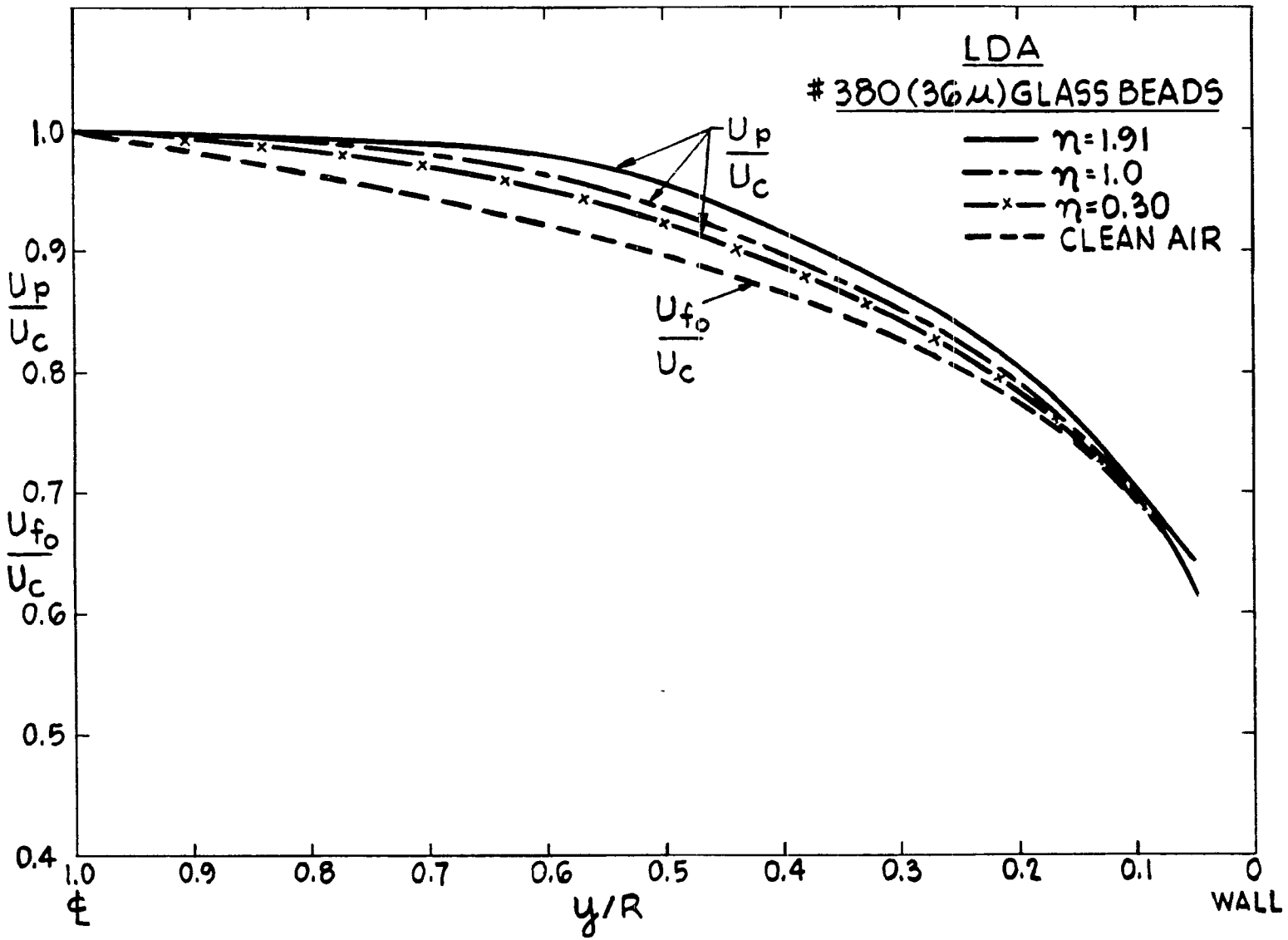

Figure 8. Particle Mean Velocity Profiles in Suspension Flow.

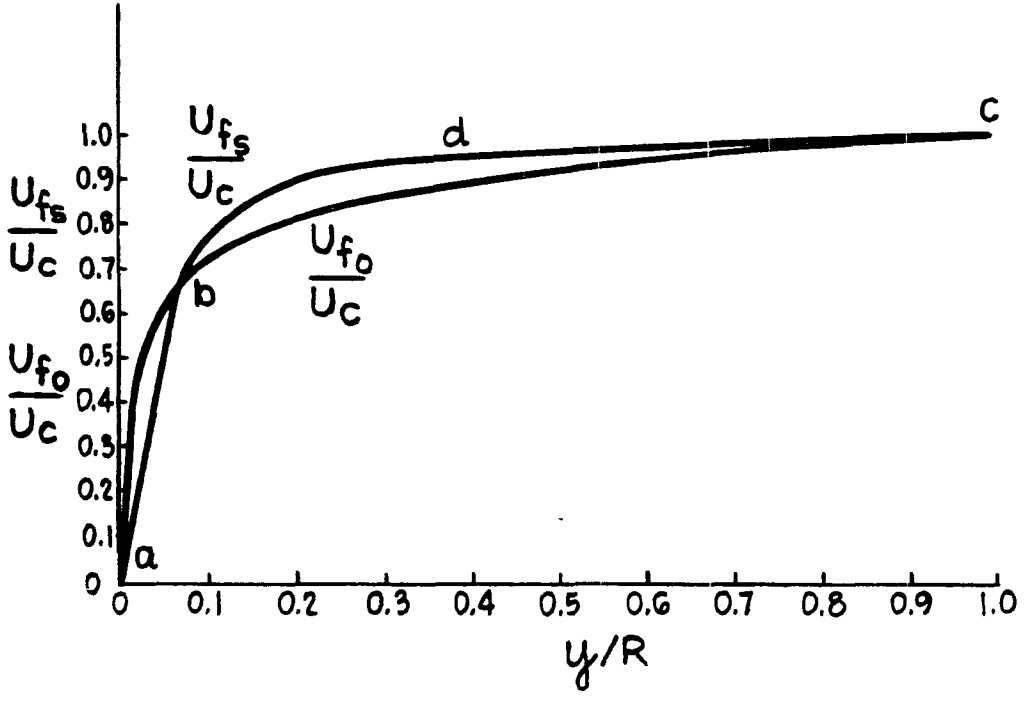

Figure 9. Gas Mean Velocity Profiles, Reproduced from Boothroyd (1966). Curve b to c was Obtained from Experimental Data and Curve a to b was Obtained from Theoretical Assumptions Based on the Velocity Defect Law.

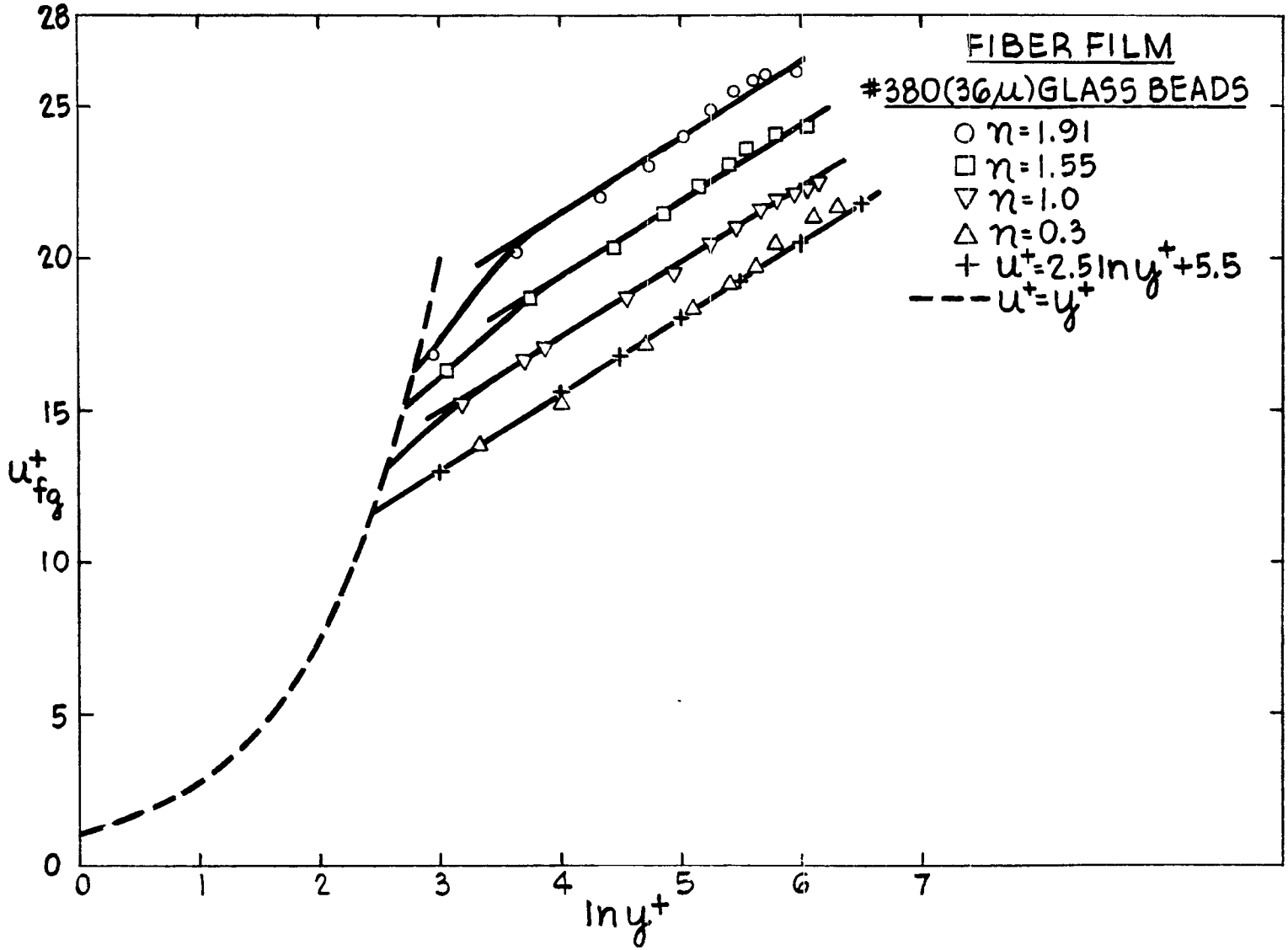

Figure 10. Dimensionless Mean Air Velocity as a Function of Dimensionless Distance from the Wall in Suspension Flow.

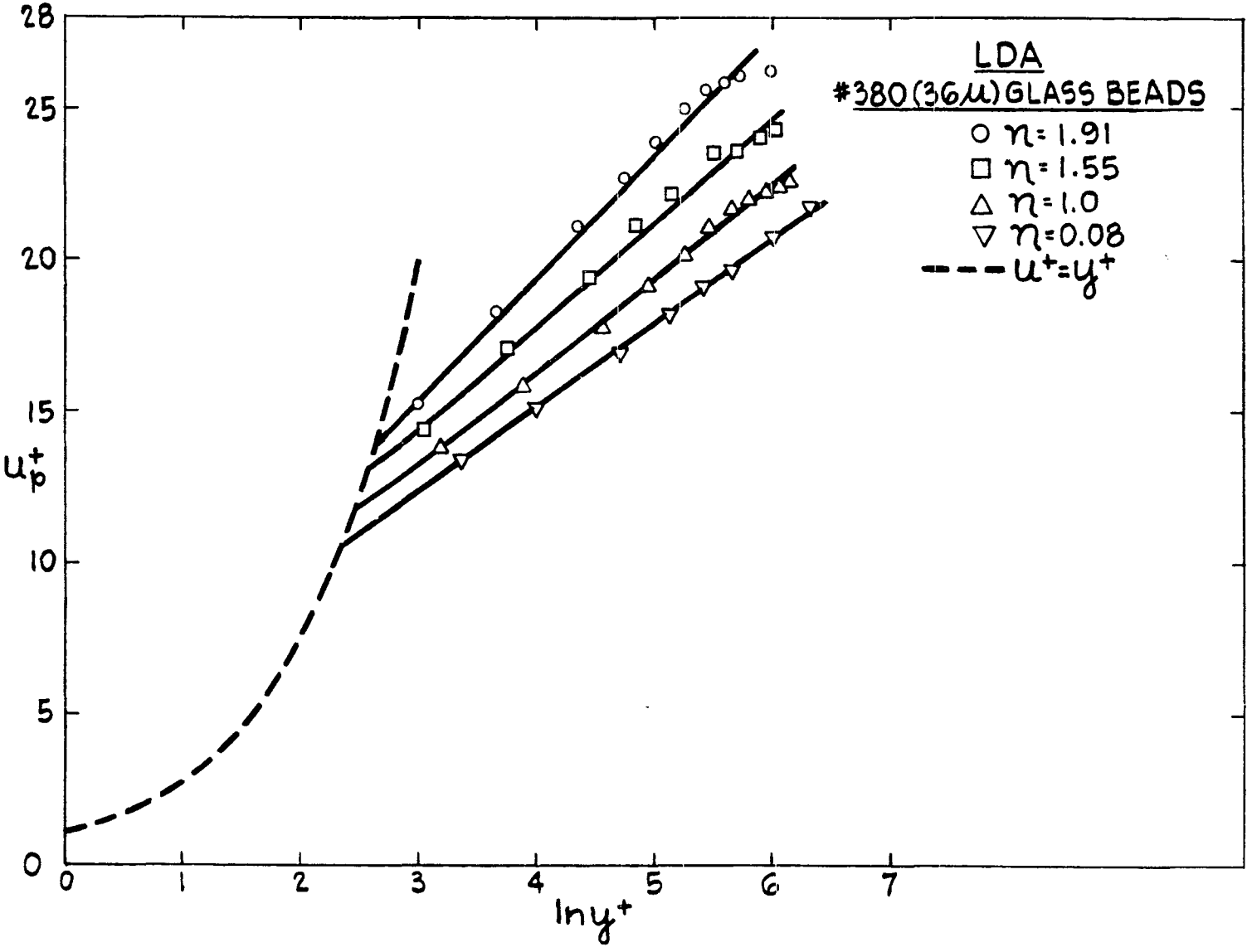

Figure 11. Dimensionless Mean Particle Velocity as a Function of Dimensionless Distance from the Wall in Suspension Flow.

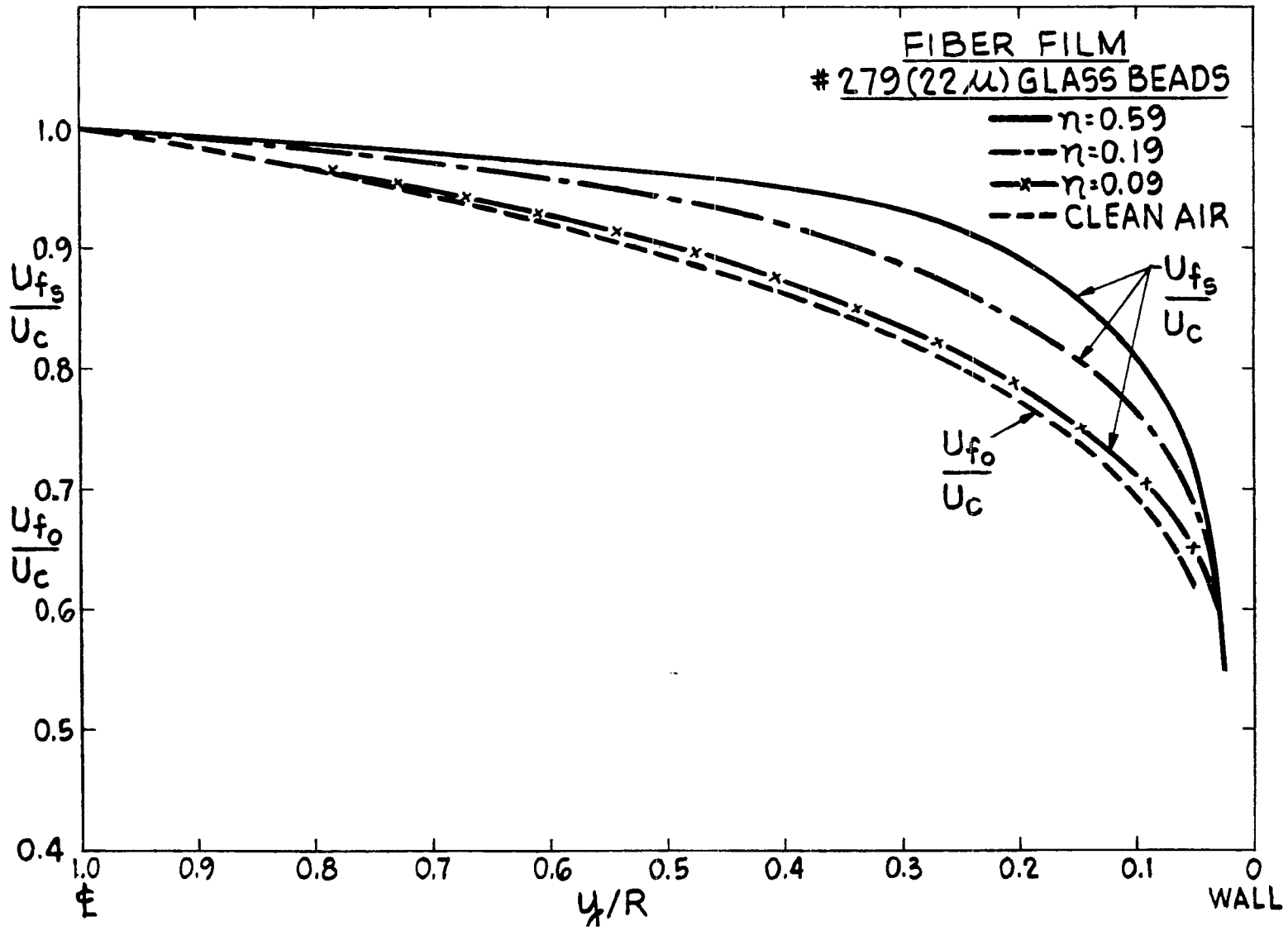

Figure 12. Air Mean Velocity Profiles in Suspension Flow.

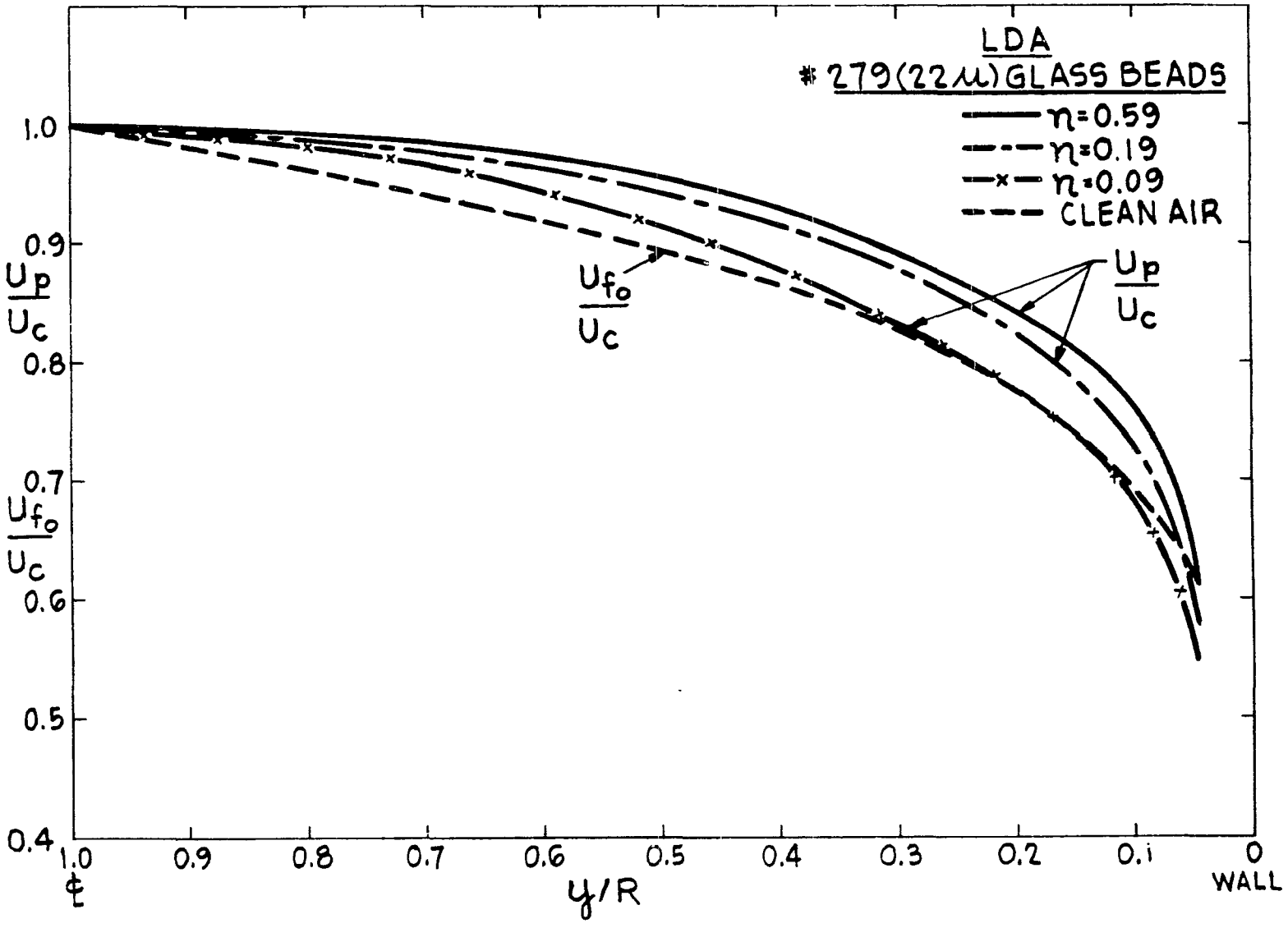

Figure 13. Particle Mean Velocity Profiles in Suspension Flow.

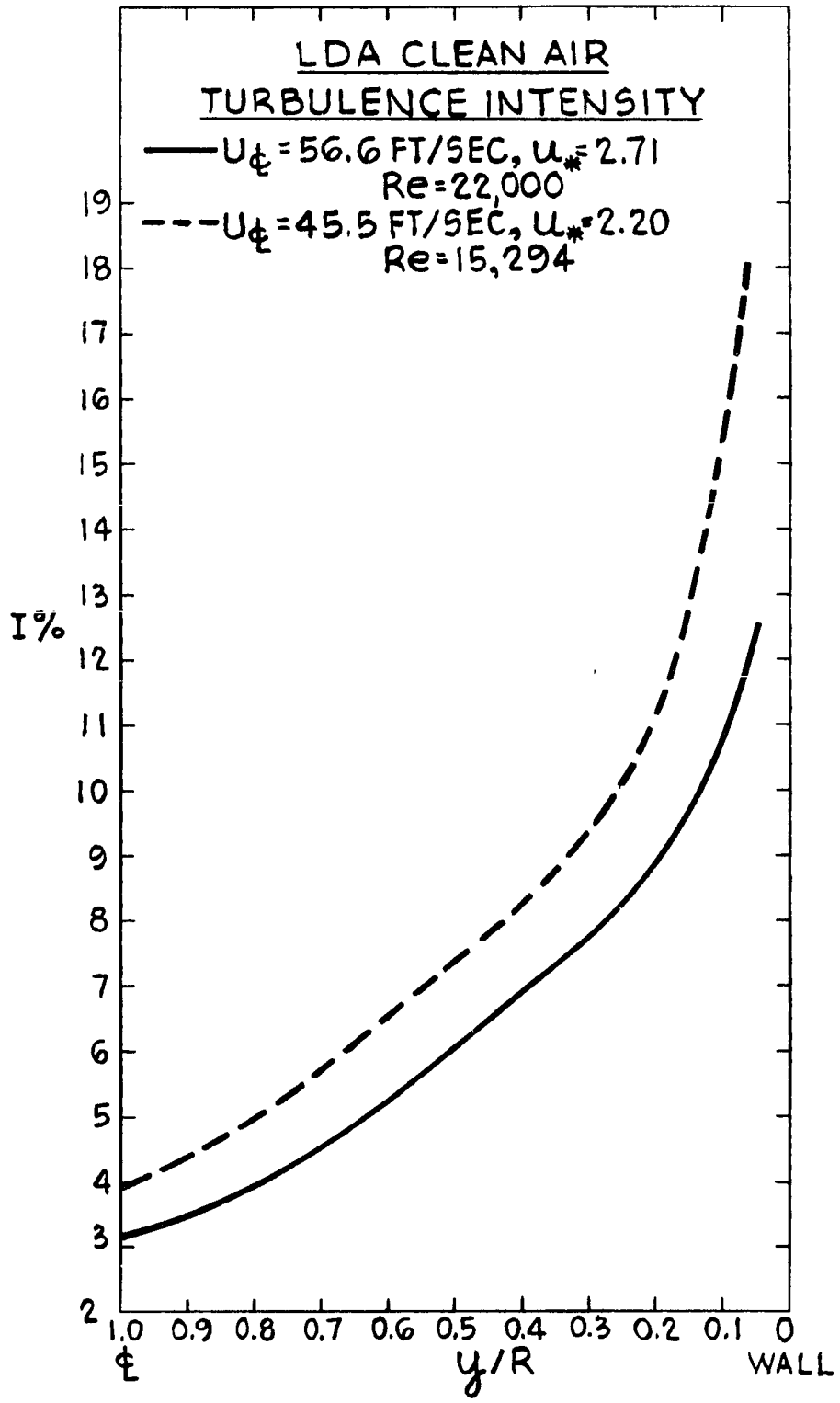

Figure 14. Streamwise Intensity of Turbulence Profiles of Clean Air as Measured with the Laser Anemometer.

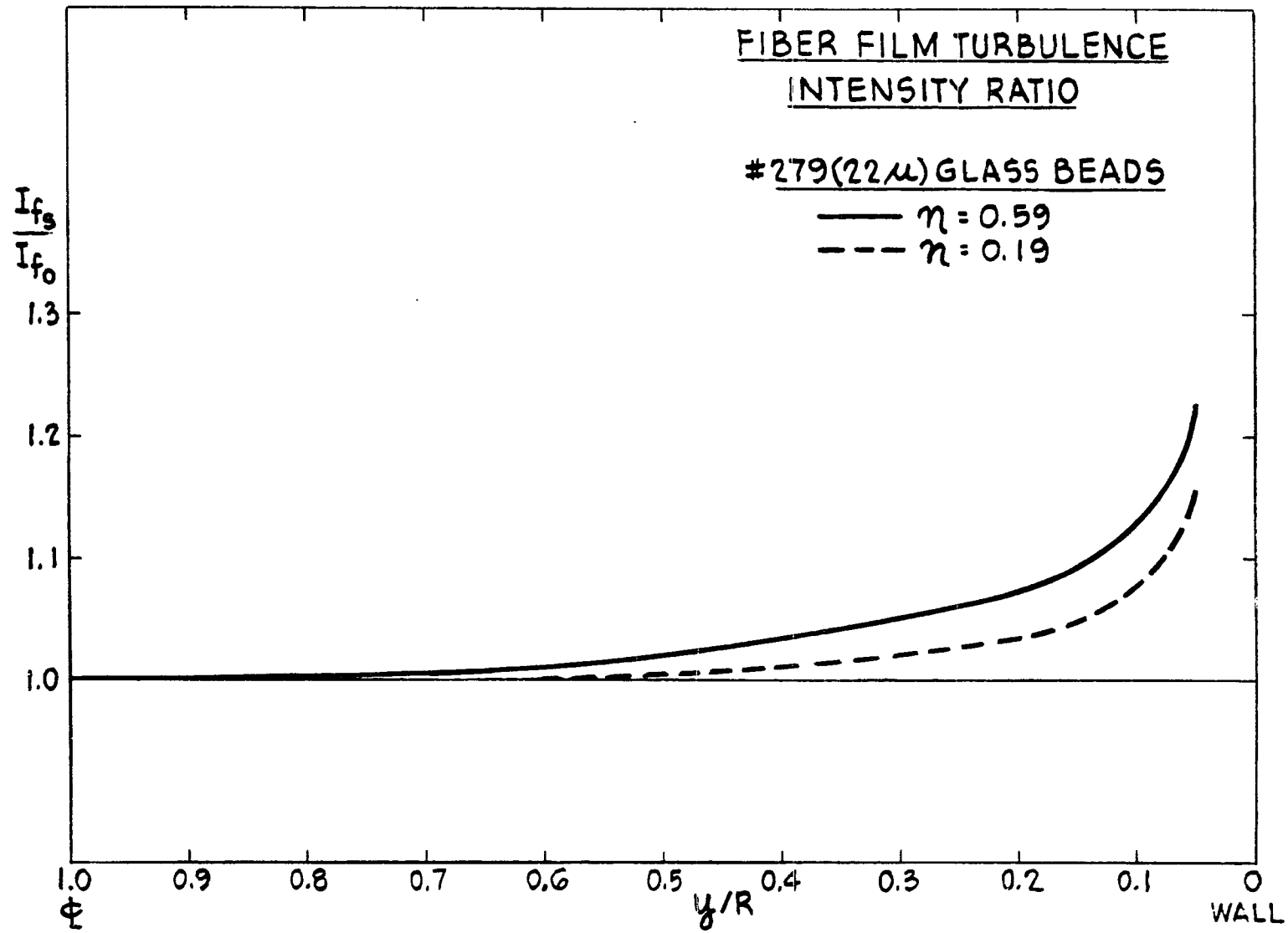

Figure 15. Dimensionless Streamwise Gas Turbulence Intensity Ratio in Suspension Flow.

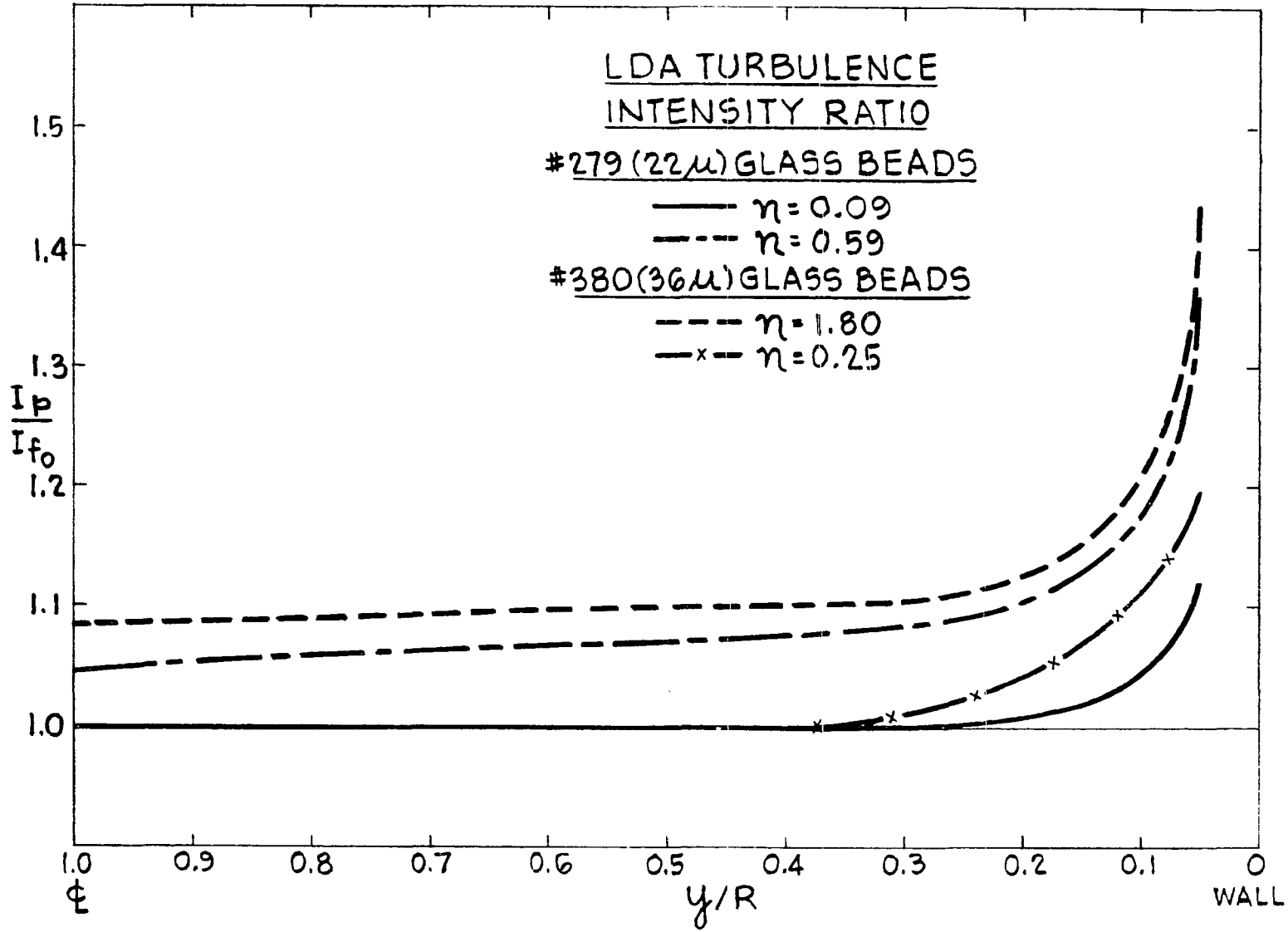

Figure 16. Dimensionless Streamwise Particle Turbulence Intensity Ratio in Suspension Flow.

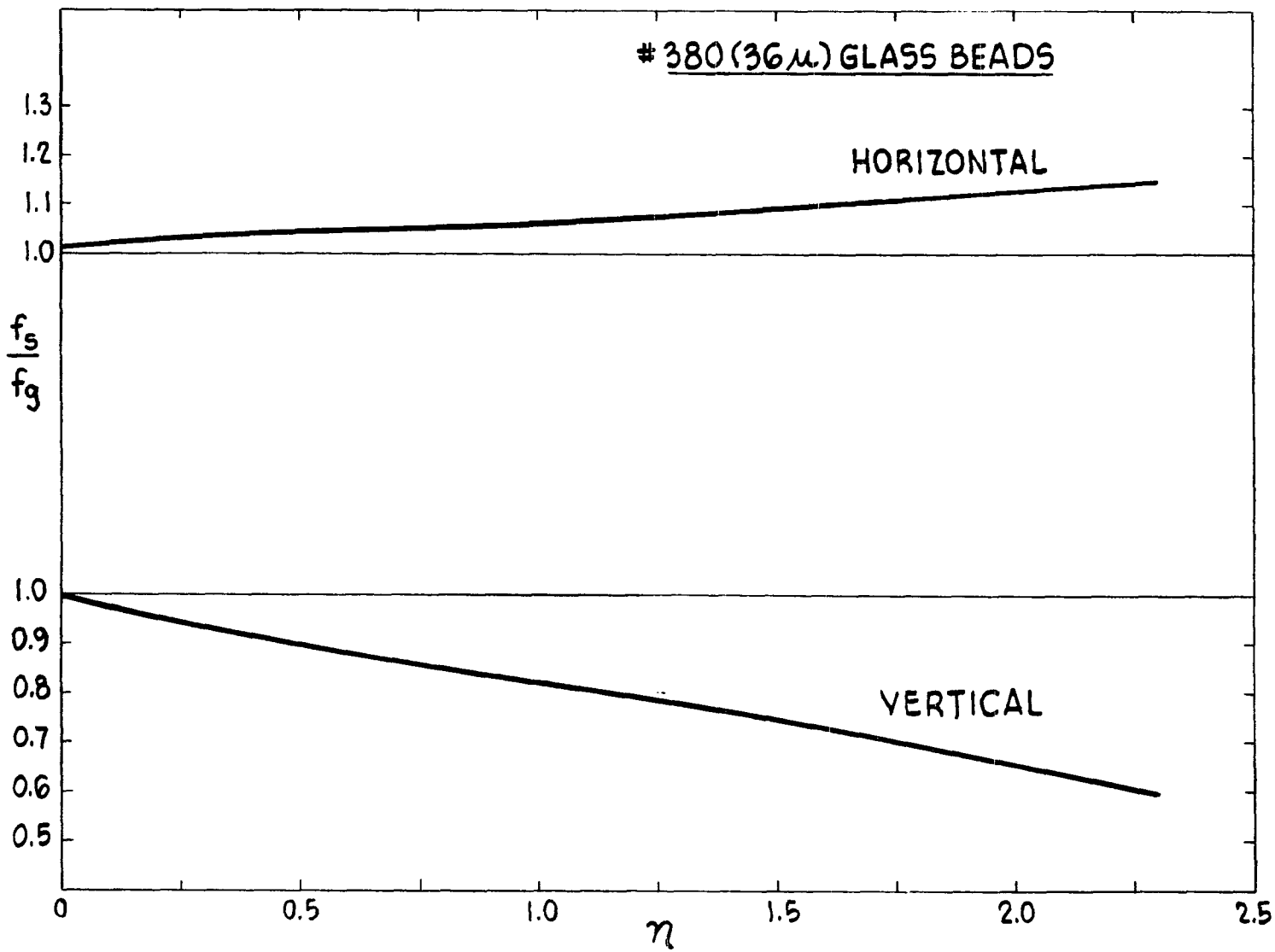

Figure 17. Friction Factor Ratio versus Loading Ratio.

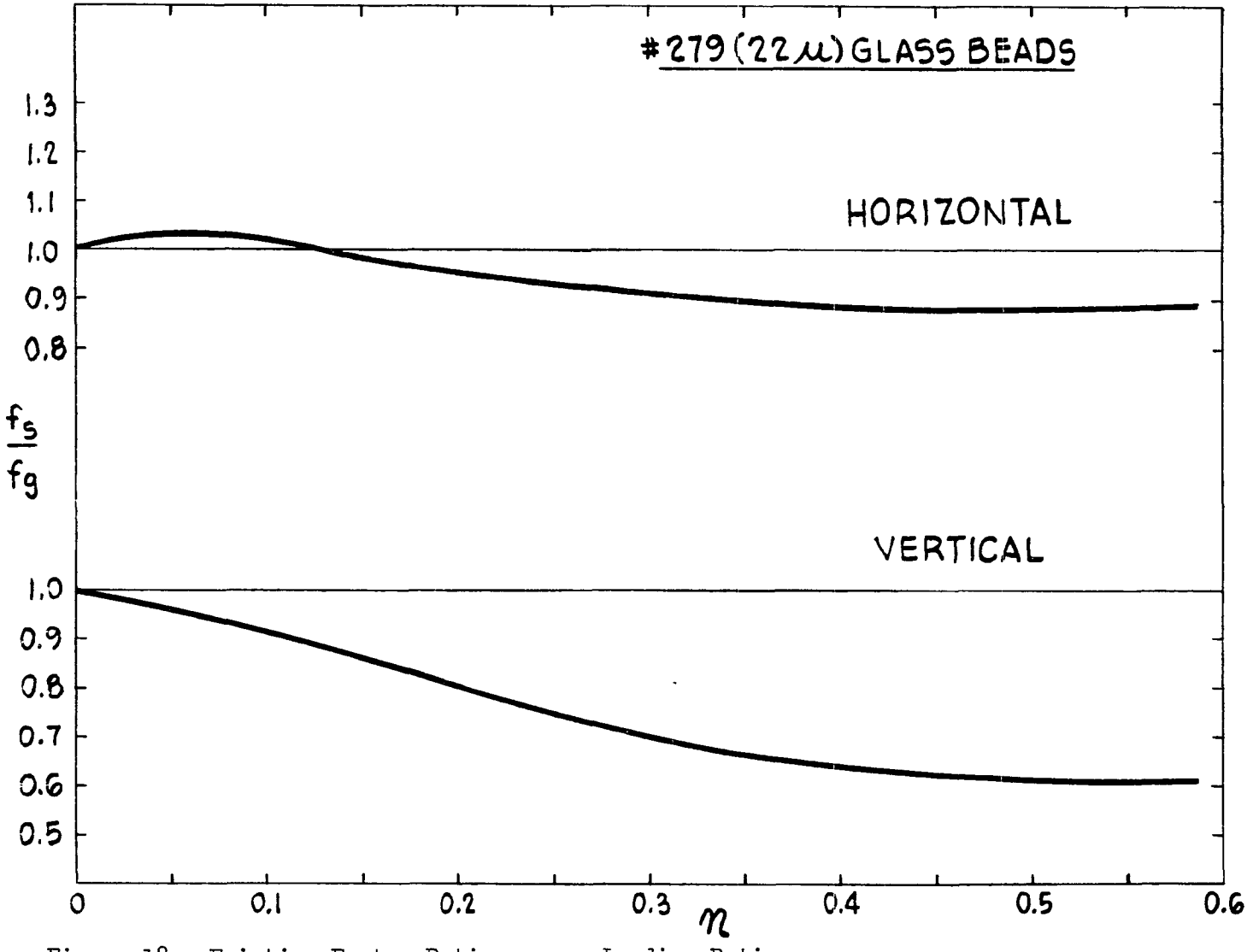

Figure 18. Friction Factor Ratio versus Loading Ratio.

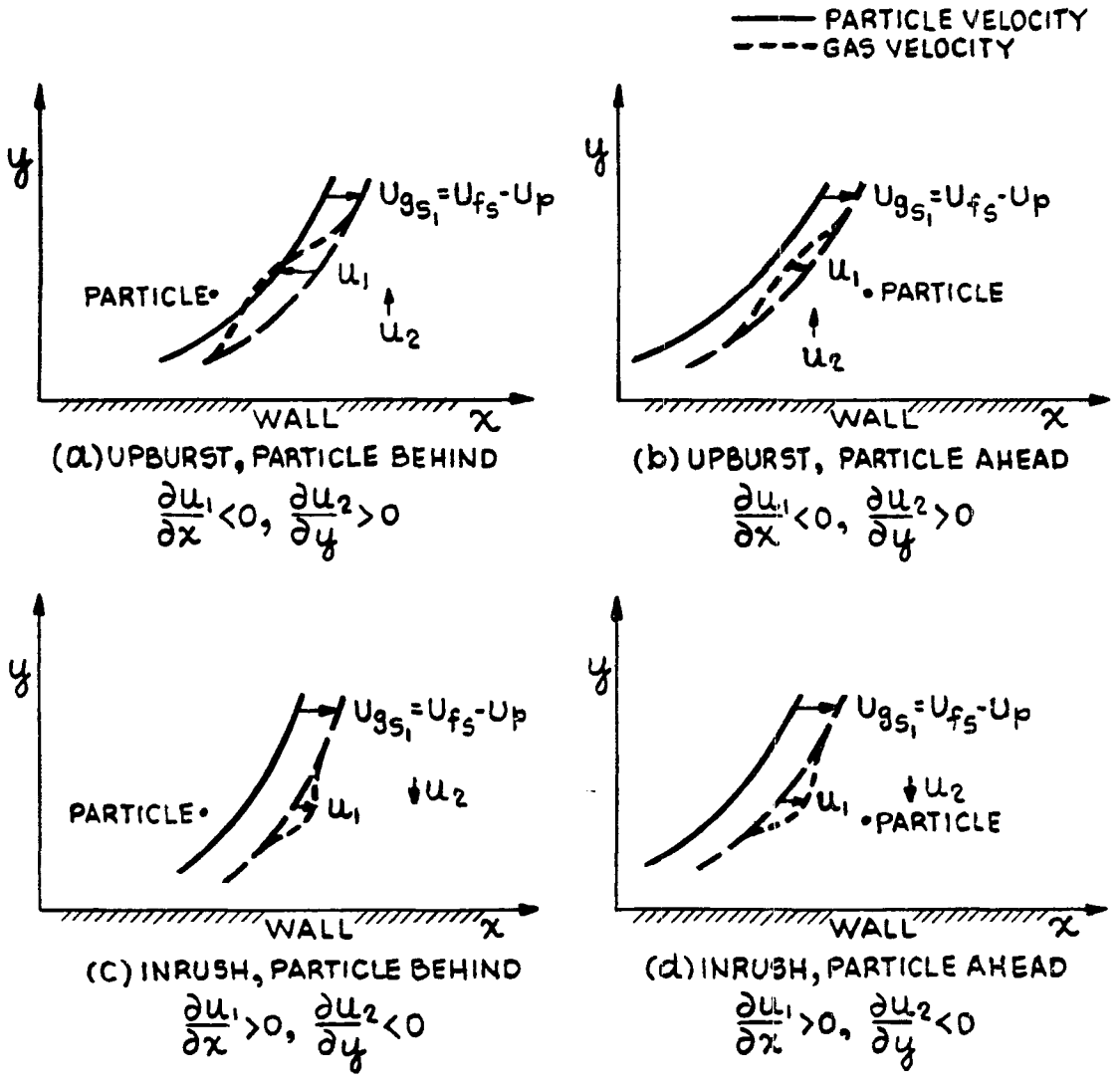

Figure 19. Effect of Eddy Motion on Particle Slip Velocity.

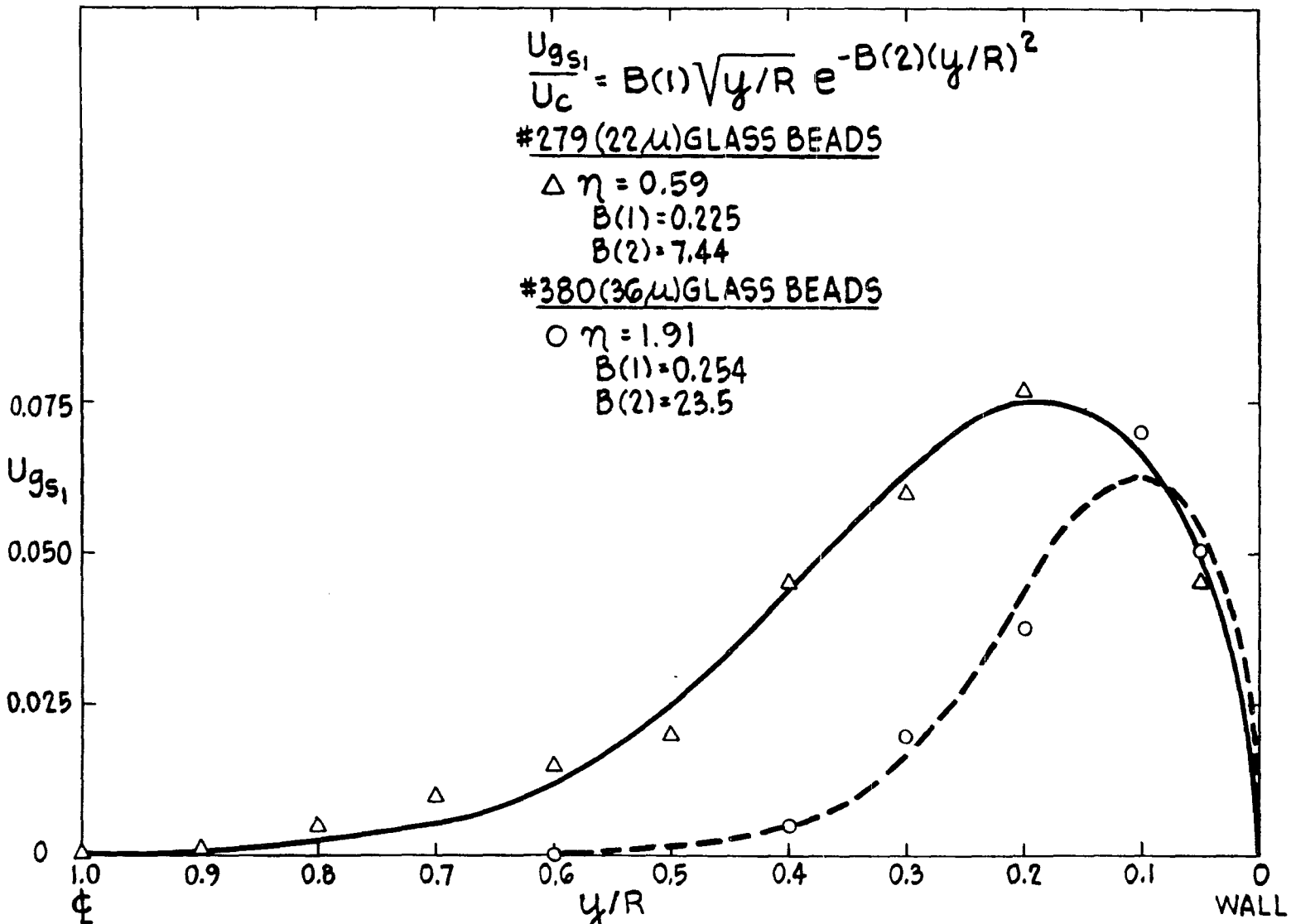

Figure 20. Fit of Equation 29 to Particle Slip Velocity.

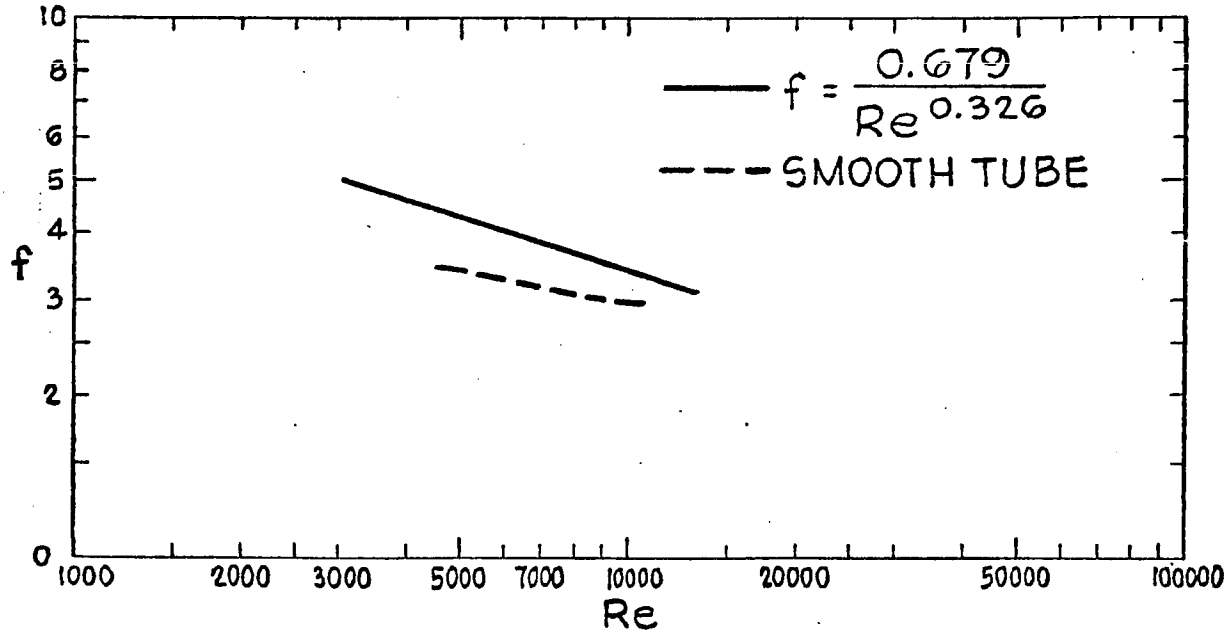

Figure 21. Friction Factor versus Reynolds Number for the 3.81 cm Test Section.

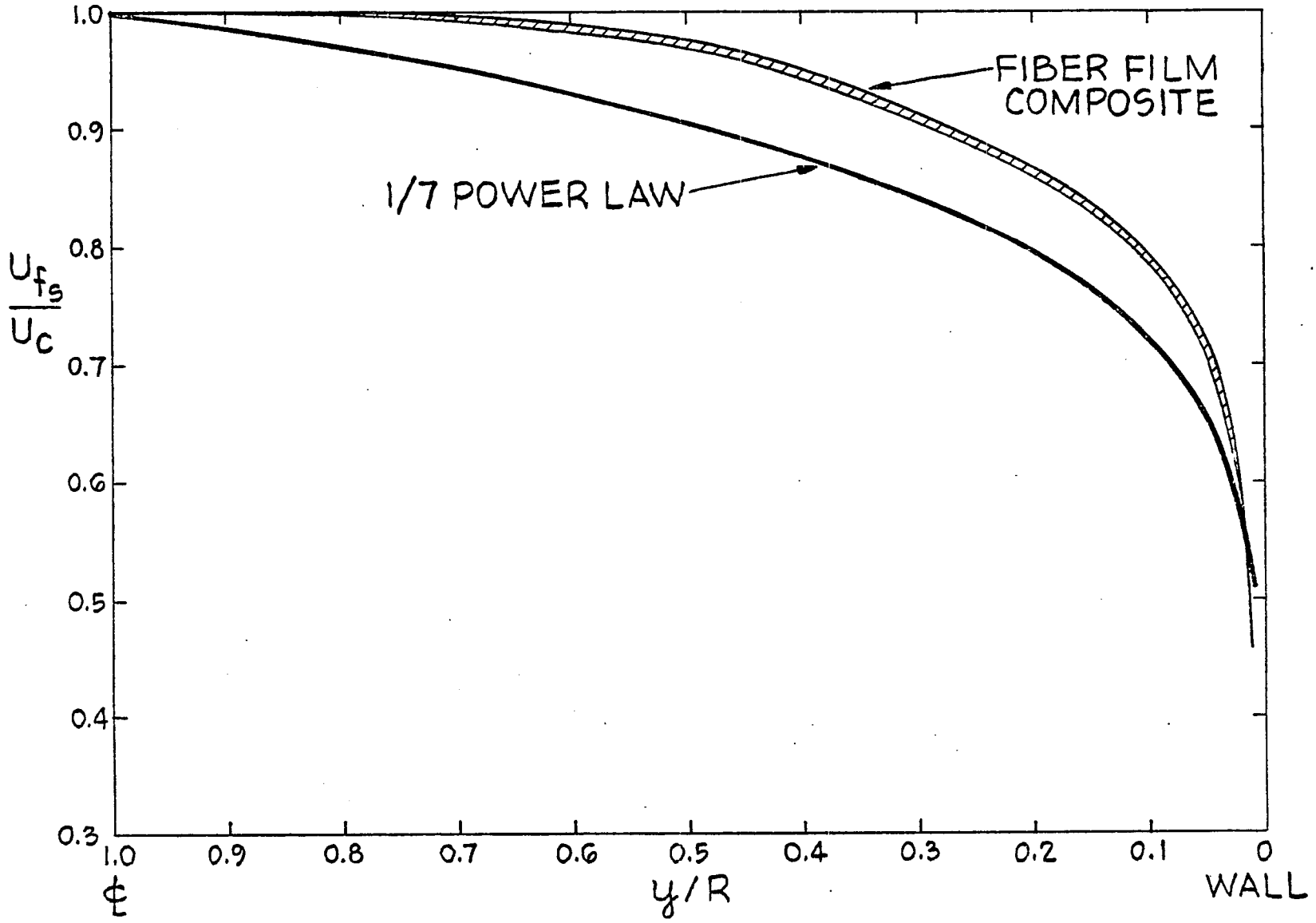

Figure 22. Clean Air Velocity Profiles for the 3.81 cm Test Section.

APPENDIX A

In order to obtain information on the macroscopic properties of the suspension flow a series of high speed motion pictures were taken in both the horizontal and vertical test sections at the two solids loading ratios where we obtained maximum drag reduction, i.e., $\eta = 0.59$ for the #279 (22μm) glass beads and $\eta = 1.91$ for the #380 (36μm) glass beads. The film used in the study was Kodak type 2484 negative film so that regions of high particle concentration appear light. A Hycam model K20S4E camera with a 90 mm lens was used with the film speed set at 5,000 frames per second. This resulted in a 312:1 reduction in flow velocity when viewed at the normal 16 frames per second.

The film that you are about to see is comprised of 8 flow sequences. The first four sequences are for #380 (36μm) glass beads in both vertical and horizontal flow at a loading ratio of 1.9. The Reynolds number is 16,800 and the centerline velocity is 17.8 m/sec. The second four sequences are for the #279 (22μm) glass beads. Here, the loading ratio is 0.63 with a Reynolds number of 15,800 and a centerline velocity of 16.7 m/sec.

ROLL FILM

#380 (36μm) Sequences

1st seq. In this first sequence the camera to flow distance is 86 mm. The dark gray region on the sides of the test section is due to the opaque glass plate used to diffuse the high intensity movie lights. As can be seen the vertical flow of particles appears to be essentially uniform.

2nd seq. This next sequence is a closeup of the previous flow. Particle streamers are clearly visible. As you can see they are mainly confined to the central portion of the flow.

3rd seq. Here we are looking at the horizontal flow of the #380 particle suspension. A thick dense layer is clearly visible at the bottom of the test section with relatively few particles in the wall region at the top of the tube. The dense particle layer gives the appearance of dune-like formations.

4th seq. In this closeup the test section just fills the screen. The thick dense layer of particles on the tube floor indicates conclusively that the flow is severely affected by gravity settling. This would account for the drag increases that we achieved for this particle size in horizontal flow.

#279 (22μm) Sequences

5th seq. The flow of the #279 glass beads in the vertical test section is essentially the same as that observed for the #380 beads. The particles appear to be uniformly distributed throughout the test section.

6th seq. In this closeup it is possible to distinguish small dense pockets of particles. Unlike the #380 beads no particle streamers are observed.

7th seq. Horizontal flow of the #279 beads appears to be much more uniform than for the #380 beads. There is only a thin layer of particles on the bottom of the test section. You can clearly see the turbulent bursts ejecting particles from the particle layer on the tube floor.

8th seq. This final sequence is a closeup of the horizontal flow of the #279 beads. The flow here appears to be essentially uniform. There is a thin dense layer of particles near the tube floor and a thin layer of low particle concentration near the tube ceiling.

CHAPTER II: AN APPROXIMATE THEORY FOR INCOMPRESSIBLE VISCOUS FLOW PAST TWO-DIMENSIONAL BODIES IN THE INTERMEDIATE REYNOLDS NUMBER REGIME $O(1) < Re < O(10^2)$

SUMMARY

A new approximate theory is proposed for treating the flow past smoothly contoured two-dimensional and axisymmetric bluff bodies in the intermediate Reynolds number range $0\ (1) < Re < 0\ (10^2)$ where the displacement effect of the thick viscous layer near the surface of the body is large and a steady laminar wake is present. The theory is based on a new pressure hypothesis which enables one to take account of the displacement interaction and centrifugal effects in thick viscous layers using conventional first order boundary layer equations. The basic question asked is how the wall pressure gradient in ordinary boundary layer theory must be modified if the pressure gradient along the displacement surface using the Prandtl pressure hypothesis is to be equal to the pressure gradient along this surface using a higher order approximation to the Navier-Stokes equation in which centrifugal forces are considered. The inclusion of the normal pressure field with displacement interaction is shown to be equivalent to stretching the streamwise body coordinate in first order boundary layer theory.

While the new theory is of a non-rigorous nature, it yields results for the location of separation and detailed surface pressure and vorticity distribution which are in remarkably good agreement with the large body of available numerical Navier-Stokes solutions. A novel feature of the new boundary value problem is the development of a simple but accurate approximate method for determining the inviscid flow past an arbitrary two-dimensional or axisymmetric displacement body with its wake.

1. Introduction

Until very recently the development of approximate theoretical models for solving the Navier-Stokes equations for laminar flow have been limited to either very low Reynolds numbers, $Re < 1$ where inertia effects are either neglected or linearized or very high Reynolds numbers, $10^3 < Re < 10^6$ where the simplifications of Prandtl's thin boundary layer theory are valid. Existing theoretical studies of flows in the intermediate Reynolds number range $1 < Re < 10^3$ have been confined primarily to numerical solutions of the full Navier-Stokes equations. These exact solutions which provide an invaluable guide for the construction of approximate theoretical models, require large amounts of computer time on even the most advanced of the present generation of computers. The recent numerical studies of Gluckman (1971), Ghia and Davis (1974), Briley and McDonald (1974), Werle and Bernstein (1975) and Ghia et al (1975), however, strongly suggest that flows in the lower portion of this intermediate Reynolds number range $O(1) < Re < (10^2)$, where a steady laminar wake is observed on bluff bodies, can be analyzed using boundary layer like models provided the viscous-inviscid displacement interaction with the external inviscid flow is adequately treated.

The present investigation proposes an approximate model, based on a new pressure hypothesis, which is able to predict to within a few percent the location of separation and the detailed surface pressure and vorticity distribution on smoothly contoured semi-infinite and finite bodies. Detailed numerical comparisons with available two-

dimensional finite difference solutions of the Navier-Stokes equations for parabolas and circular cylinders are shown in the present Chapter. Equally good agreement with exact Navier-Stokes solutions for the axisymmetric flow past paraboloids of revolution and spheres is presented in Chapter III.

Some idea of the magnitude of the displacement interaction on a bluff body at Reynolds numbers typical of those considered in the present study can be gleaned from the following example. At Re = 30 the displacement thickness at the forward stagnation point on a circular cylinder is about 15 percent of its radius. At the location of separation, which is approximately 130 degrees from the forward stagnation point for this Reynolds number, the displacement thickness has grown to about 0.7 radii and increases rapidly in the separated flow downstream. It is not surprising in view of the large changes in effective body shape that the external inviscid flow must experience at these Reynolds numbers that a theory of successive approximation which is based on the potential flow past the original body shape will converge very slowly. This would appear to be the basic difficulty encountered in extending the results of second order boundary layer theory, Van Dyke (1962) to flows with Reynolds numbers less than about 10^3.

In the past few years Davis, Ghia, Werle and co-workers have performed a series of numerical experiments, which are summarized in Ghia et al (1975), that greatly elucidate the importance of the various terms in the Navier-Stokes equations in the Reynolds number range $0(1) < Re < 0(10^3)$. In these numerical experiments several different approximate models to the complete two-dimensional Navier-Stokes equations are considered. In each model one solves an approximate viscous flow equation

for the vorticity distribution throughout the entire flow field and a streamfunction equation relating the vorticity ω to the two-dimensional streamfunction Ψ. In the most accurate model termed the parabolized-vorticity approximation, Ghia and Davis (1974), only the streamwise diffusion terms are dropped from the Navier-Stokes vorticity equation and the full elliptic streamfunction equation is used. The results obtained are in almost perfect agreement with the exact Navier-Stokes solution of Davis (1972) for the flow past a parabola and Ghia and Davis (1974) for the two-dimensional flow past a semi-infinite body with a shoulder in which separation can occur depending on the shoulder bluntness. In a second model the curvature terms are omitted from the parabolized vorticity equation. The agreement with exact Navier-Stokes solutions is not quite as satisfactory as the first model but still a significant improvement over conventional boundary layer theory. In both these models the viscous-inviscid interaction describing the displacement and separation effects is automatically included since the full elliptic streamfunction equation is used for the entire flow field. In a third model called the parabolic approximation, the curvature terms are retained in the parabolic approximation to the Navier-Stokes vorticity equation, as in the first model, but a boundary layer like streamfunction is employed. Very good agreement with exact Navier-Stokes equations could be obtained, except for cases of extreme shoulder curvature, provided either the Navier-Stokes generated surface vorticity distribution or streamfunction distribution in the inviscid external flow is prescribed. No difficulty is encountered in integrating through the separation point singularity confirming the result first reported by Catherall and Mangler (1966) that if the displacement interaction was

properly accounted for this singularity in the forward numerical integration of the boundary layer equations could be removed. If, on the other hand, the Navier-Stokes interaction pressure or velocity field at the edge of the viscous layer were prescribed instead of the aforementioned vorticity or streamfunction distributions the difficulty in integrating through the separation point still persisted.

Further important evidence that the boundary layer equations are still an adequate description of the velocity profile development in a thick viscous layer with strong displacement interaction is found in the work of Gluckman (1971) and Werle and Wornom (1972). These two studies show that if either experimentally measured or Navier-Stokes generated surface pressure distributions are used to drive the Prandtl boundary layer equations, good predictions of the separation point location and surface vorticity distribution are possible for the flow past a circular cylinder for the entire range of Reynolds numbers where a steady wake separation bubble exists, even though all curvature effects have been omitted. These findings, which at first glance appear to contradict the results reported in Ghia et al (1975) where curvature effects were shown to be important if close numerical agreement with the Navier-Stokes solutions were to be obtained, can be explained if the curvature effects omitted from the boundary layer equations themselves are retained in the description of the viscous layer as a modification of the surface pressure boundary condition. The results presented in this study provide strong evidence that this is indeed the case, since it is demonstrated that if the streamwise coordinate along the body surface is stretched in accordance with the new pressure hypothesis derived herein the pressure distribution along

the surface of the body will agree remarkably well with the Navier-Stokes predicted surface pressure distribution. The new pressure hypothesis states that if the conventional Prandtl boundary layer equations are to include the lowest order curvature effects in the viscous layer then the streamwise pressure gradient as a function of distance along the surface should be equal to the local pressure gradient as a function of distance along the displacement body. The hypothesis implies that the effective pressure interaction for a viscous layer with curvature using first order boundary layer equations is the streamwise distance measured along its centroid of vorticity. Lighthill (1958) has shown that this centroid is equivalent to the local displacement thickness of the viscous layer.

The crucial problem in the development of any approximate theory based on the matching of an inner viscous and outer inviscid flow is the construction of an effective displacement body when the inviscid pressure distribution used to determine the viscous layer displacement growth is also not known. In a matching problem of this nature one attempts to develop an iterative solution scheme based on a judicious initial guess of either the viscous layer displacement growth or the inviscid pressure field. The same difficulty which caused the iterative solution procedure of second order boundary layer theory to break down at lower Re, the large distortion in effective body shape due to the displacement interaction of the thick viscous layers, however, can be used to good advantage in a different scheme of successive approximation. For flows whose Reynolds numbers are of 0 (10^2) or less the details of the wake separation bubble on a bluff object such as a cylinder are completely enshrouded in the thick viscous layers that have developed

along the body surface. As far as the inviscid outer flow is concerned it is more important to approximate the qualitative shape and dimensions of the effective displacement body and its wake than the detailed geometry of the original body or the fine structure of the separated flow region. To this end one seeks an iterative approximation procedure in which the lowest order solution for the growth of the displacement thickness along the body surface already takes into account the change in surface pressure gradient due to the local enlargement of the body and centrifugal effects. The local inviscid pressure gradient obtained from a geometrically similar body whose local radius is equal to the local body radius plus the local displacement thickness provides a convenient geometry for generating the lowest order solution. This simplified body approximately reproduces the local radius of curvature of the effective displacement body, the local flow characteristic which is of greatest importance according to the new pressure hypothesis stated above. The lowest order approximation for the displacement body is now used to generate a new inviscid pressure distribution, which in turn is used to calculate a more accurate displacement thickness distribution. The procedure is repeated until a converged solution of predetermined accuracy is obtained.

In Section 2 we present the theoretical motivation behind the new pressure hypothesis. Section 3 states the boundary value problems for the viscous and inviscid flow regions. The general solution procedure is outlined in Section 4. Sections 5 and 6 describe the application of the new displacement interaction model to parabolic and circular cylinders and present detailed numerical comparisons with existing exact Navier-Stokes solutions for the flow past these bodies. Section 7 briefly

discusses the results for other boundary shapes and concludes with some general comments about the validity and accuracy of the model.

2. The New Pressure Hypothesis for the Viscous Layer

In the conventional construction of the displacement body one refers the pressure along the displacement body back to the surface of the original body along the normal boundary layer coordinate treating the pressure as constant on this coordinate. This pressure mapping has implicit in it the assumption that the pressure gradient measured along the actual and displacement body surfaces are related by

$$\frac{dp}{ds_w} = \frac{R^*}{R_w} \frac{dp}{ds^*} \tag{1}$$

where the subscript w denotes the wall, the superscript * the displacement body, s the distance along each surface, and R the local radius of curvature assuming that both surfaces are nearly parallel. The difference in pressure gradient is thus of 0 (δ) and is strictly a geometrical consequence of the wall curvature and is not related to the centripetal force field.

We now wish to examine how the streamwise pressure gradient varies across a thick viscous layer in which centrifugal effects are present to see how equation (1) must be modified to obtain a more accurate description of the wall pressure gradient. To this end we examine the following approximate set of governing equations for the viscous layer

$$u\frac{\partial u}{\partial s} = -\frac{1}{\rho}\frac{\partial p}{\partial s} + \nu\frac{\partial^2 u}{\partial n^2} \tag{2}$$

$$\frac{u^2}{R} = \frac{1}{\rho}\frac{\partial p}{\partial n} \tag{3}$$

where s and n here refer to natural streamline coordinates. Note that the higher order curvature correction for the viscous term in equation (2) has been omitted.

The simplifying feature of supersonic viscous-inviscid interaction theory is that there is a local relation between pressure and flow angle at the edge of the boundary layer. This simplification permits one to derive using rational arguments the characteristic streamwise distance for a self-induced displacement interaction leading to separation and the characteristic thickness of the viscous sublayer near the wall. No equivalent rational theory has yet been developed for incompressible displacement interactions leading to separation. For high Reynolds number flow the size of the separated flow region is typically of the order of the body dimensions though the length of run for which the body boundary layer can withstand an adverse pressure gradient without separating is considerably shorter. For the thick viscous layers characteristic of the intermediate Reynolds number flows examined in the present study one observes that the displacement thickness can double over a distance which is of the same order as the viscous layer thickness. In accord with these remarks, we introduce the following dimensionless scaled coordinates into equations (2) and (3):

$$\tilde{R} = \frac{R}{R_o}, \quad \tilde{n} = \frac{n}{\delta_o}, \quad \tilde{s} = \frac{s}{\delta_o}, \quad \tilde{u} = \frac{u}{U_\infty}, \quad \tilde{p} = \frac{p}{\rho U_\infty^2} \tag{4}$$

Here $\delta_o = Re^{-1/2} R_o$ is the characteristic thickness of the viscous layer and the Reynolds number is based on the body dimension R_o and the free stream velocity U_∞. Differentiating equation (3) with respect to s and substituting for $u\frac{\partial u}{\partial s}$ from equation (2) one obtains the following differential equation for the variation of the dimensionless streamwise

pressure gradient across the viscous layer:

$$\frac{\partial}{\partial \tilde{n}}\left(\frac{\partial \tilde{p}}{\partial \tilde{s}}\right) + \frac{2}{Re^{1/2}\tilde{R}}\left(\frac{\partial \tilde{p}}{\partial \tilde{s}}\right) = -\frac{1}{Re^{1/2}}\frac{\tilde{u}^2}{\tilde{R}^2}\frac{\partial \tilde{R}_w}{\partial \tilde{s}} + \frac{2}{ReR}\frac{\partial^2 \tilde{u}}{\partial \tilde{n}^2} \qquad (5)$$

where

$$\tilde{R} = \tilde{R}_w + Re^{-1/2}\tilde{n}$$

The integral of equation (5) which satisfies the condition

$$\frac{\partial \tilde{p}}{\partial \tilde{s}} = \frac{\partial \tilde{p}}{\partial \tilde{s}_w} \quad \text{at } \tilde{n} = 0$$

is

$$\frac{\partial p}{\partial s} = \frac{\partial p}{\partial s_w}\left(\frac{R_w}{R}\right)^2 + \frac{1}{Re^{1/2}R^2}\frac{\partial R_w}{\partial s_w}\int_o^n u^2\,dn$$

$$+ \frac{2}{Re\,R^2}\left(R\,\frac{\partial u(n)}{\partial n} - R_w\frac{\partial u(o)}{\partial n} - \frac{1}{Re^{1/2}}u(n)\right) \qquad (6)$$

where the tilda superscript has been dropped. Equation (6) relates the streamwise pressure gradient at any height n in the viscous layer to the wall pressure gradient $\partial p/\partial s_w$. The first term on the right hand side of equation (6) represents the centrifugal correction due to the change in streamline curvature as one moves away from the wall. The second term represents the correction due to the change in curvature of the wall. This term vanishes for a circular cylinder and in general will be smaller than $O(Re^{-1/2})$ unless R_w changes to lowest order on a length scale of $O(\delta_o)$. The third group of terms in parentheses is the viscous correction and is observed to be of $O(Re^{-1})$ or

smaller. The dominant correction to the streamwise pressure gradient as one moves away from the wall is thus seen to arise from the first term except for local regions with large changes in wall curvature where the second term on the right hand side of equation (6) will also be important. The viscous correction is higher order in the Re since the variation in the normal pressure field is principally due to centrifugal effects.

The important result which we wish to obtain from equation (6) is the relationship between the wall pressure gradient and the streamwise pressure gradient acting along the fictitious surface which the external flow perceives as the effective body shape including displacement effects. Denoting this effective displacement body by R* and neglecting the higher order viscous corrections, one finds from equation (6) that

$$\frac{\partial p}{\partial s^*} = \frac{\partial p}{\partial s_w}\left(\frac{R_w}{R^*}\right)^2 + \frac{1}{Re^{1/2}R^{*2}}\frac{\partial R_w}{\partial s_w}\int_o^{n^*} u^2\,dn \qquad (7)$$

We now return to the original problem posed just prior to equation (2). The essential question is whether equation (1) which is based on first order boundary layer theory and neglects all centrifugal effects can be simply modified so that it generates a displacement body which has the same pressure distribution along its surface as that predicted by equation (7) which includes these effects. For the two pressure distributions to be equal to within an arbitrary constant one equates $\partial p/\partial s^*$ in equations (1) and (7). Denoting the wall pressure gradient predicted by equation (7) by the subscript n to signify the presence of the normal pressure field, one obtains

$$\frac{\partial p}{\partial s_{wn}} = \frac{\partial p}{\partial s_w}\left(\frac{R^*}{R_w}\right) - \frac{\dfrac{\partial R_w}{\partial s_w}}{Re^{1/2} R_w^2}\int_o^{n^*} u^2\, dn \qquad (8)$$

For smoothly contoured bodies without rapid changes in surface curvature equation (8) reduces to

$$ds_w = \frac{R^*}{R_w}\, ds_{wn} = ds^* \qquad (9)$$

Equation (9) states that the pressure gradient along the effective displacement body constructed in the conventional manner using first order boundary layer theory will be the same as in a viscous layer theory which includes centrifugal forces provided the differential distance element along the body surface ds_{wn} is stretched by the factor R^*/R_w in mapping the pressure distribution from the displacement body back to the surface of the original body. This stretching implies that the pressure is referred from the displacement body back to the original body in a manner that preserves arc length, that is $ds_w = ds^*$.

The principal assumption introduced in the derivation of the new pressure hypothesis, equation (8) or (9), is that the characteristic streamwise length scale for the displacement induced viscid-inviscid interaction for a thick viscous layer is approximately of $O(\delta_o)$. The assumption is based on numerical and experimental observations and not rational theoretical arguments. It is also assumed that the displacement surface is represented by a streamline in the viscous layer (see equation (7)) and that the local radius of curvature of the displacement body is equal to the local radius of curvature of

the original body plus the local displacement thickness. Both assumptions are reasonable approximations at best. The derivation, despite its nonrigorous nature, leads to a result which greatly simplifies the treatment of curvature effects in thick viscous layers and provides remarkably good agreement with exact Navier-Stokes solutions.

In concluding this section we should mention that several other derivations of the pressure hypothesis have been tried. One approach that appeared particularly promising was based on the observation of Davis (1974) that the displacement body in the several flow geometries that he considered could be closely approximated by a conformal coordinate system. If this were the case then the flow past the displacement body could be transformed into a stagnation point flow through a conformal mapping. As is well known the pressure gradient in a stagnation point does not vary normal to the wall. This suggested that the streamwise pressure gradient might also exhibit special properties when its variation along the normal conformal coordinate to the displacement body were examined. One finds that for the flow past a wedge the normal derivative of the streamwise pressure gradient at the wedge surface vanishes but that this property is not in general true for other geometries.

3. The New Boundary Value Problem

The new boundary value problem for the matching of the inner viscous and outer inviscid flow fields differs from conventional theory principally in the construction of the effective displacement body and the application of the pressure hypothesis used to determine the wall pressure distribution. The governing equation for the viscous layer is the

usual first order boundary layer equation

$$u\frac{\partial u}{\partial x} + v\frac{\partial u}{\partial y} = -\frac{1}{\rho}\frac{dp}{dx} + \nu\frac{\partial^2 u}{\partial y^2} \tag{10}$$

Here x measures distance s_w along the original body surface and the pressure gradient is determined by the inviscid flow past the effective displacement body in accord with the pressure hypothesis (9). This hypothesis requires that

$$\frac{dp}{dx} = \frac{dp}{dx^*} \tag{11}$$

with

$$x = x^*$$

Where x* is the distance s* from the forward stagnation point of the displacement body. The pressure as a function of distance along the original and displacement bodies are thus equal except for an additive constant due to viscous losses in total pressure along the streamline passing through the forward stagnation point. Since $r^* > r_w$ the local polar coordinate θ is stretched such that θ > θ* as shown in Figure 1.

The effective displacement body is constructed by adding the displacement thickness distribution,

$$\delta^*(x) = \frac{1}{U(x)} \int_0^{\delta(x)} (U(x)-u)dy, \tag{12}$$

obtained from the solution of equation (10) for the velocity profile to the original body surface. This construction differs from the conventional method of constructing the displacement body in that the inviscid pressure gradient at position x* (angular location θ*) on the displacement surface is used to calculate the displacement thickness δ*

at position x (angular location θ) on the original body in accord with the pressure mapping described by equation (11).

The inviscid pressure distribution and the velocity $U(x^*)$ at the surface of the displacement body is determined from the solution to the potential flow equation

$$\nabla^2 \Phi = 0 \tag{13}$$

for the velocity field. This equation satisfies the usual inviscid boundary condition that the normal component of the velocity vanish at the displacement surface

$$v(x^*) = 0 \quad \text{on} \quad r = r^* \tag{14}$$

Since the solution for $\delta^*(x)$ depends on the solution for $U(x)$ and both are unknown, the solution of equations (10) through (14) represents a coupled non-linear boundary value problem. In essence, we wish to solve equation (13), subject to a known boundary condition (14) along an unknown surface, the effective displacement body. This body is determined from the solution of equation (10) in which the surface pressure distribution satisfies the pressure hypothesis (11) and must be obtained through a process of iterative approximation.

4. Solution Procedure

The solution of the boundary value problem just described to determine the effective displacement body requires that we make an initial guess of either the displacement thickness distribution or the pressure distribution used in equation (10) to determine this distribution. The rapidity of convergence of the solution procedure depends in a large measure on how good this initial estimate of δ^* or dp/dx is. For the

reasons stated in the introductory section, it appears that the critical considerations in optimizing this first trial guess are the ability to reproduce the qualitative dimensions of the effective displacement body while taking account of the centrifugal effects in the thick viscous layer through the use of the surface pressure hypothesis. An additional improvement in making this first guess can be obtained if at each step in the forward numerical integration of equation (10) the solution for the displacement thickness distribution up to that step is somehow incorporated into the assumed expression for the local pressure gradient. To try and accurately curve fit the displacement body at each forward integration step would be extremely time consuming. A convenient practical expedient which uses the latest knowledge of the growth of the displacement body and provides improved numerical results is to represent the displacement body by a family of geometrically similar bodies whose local radius is the same as the local radius of the displacement body.

The above considerations were the important motivations behind the first trial solution for the displacement body that we have adopted. A summary of the complete solution procedure including the first trial solution is given below.

A. First trial solution for the displacement body:

1. Both the displacement thickness and the pressure gradient at the forward stagnation point are unknown. To approximate the displacement body a family of geometrically similar bodies with the same focal point as the original body is selected. The pressure or velocity gradient at the forward stagnation point on the displacement body is written in

terms of the unknown displacement thickness and applied at the surface of the original body using the pressure stretching hypothesis equation (11). This expression is then simultaneously solved with equation (10) applied at the forward stagnation point. The solution technique is illustrated in subsection 4(a) for the case of a circular cylinder.

2. Having obtained this first trial solution for δ^*, dp/dx and the velocity profile at the forward stagnation point, one performs a forward numerical integration of equation (10). For present purposes it was deemed satisfactory to use the momentum integral approximation to equation (10) rather than the more accurate finite difference solutions in view of the other approximations introduced. At each forward integration step the pressure gradient is represented by the local pressure gradient for the inviscid flow past the geometrically similar body whose local radius from the focal point of the original body is equal to that of the displacement body. From equation (11) this pressure gradient is also equal to the pressure gradient along the original body surface.

3. The displacement thickness distribution obtained from the solution described in step 2. is now added on normally to the surface of the original body. Because of the pressure mapping (11) the pressure gradient at position x^* on the displacement body is used to calculate the displacement thickness at position $x = x^*$ on the original body as shown in Figure 1. This completes the first trial solution for the effective displacement body.

B. The iteration procedure for a converged solution:

1. As we shall observe in the results, the first trial solution just outlined provides a reasonable approximation for the displacement

surface since it qualitatively includes the streamwise coordinate straining required to describe curvature effects, but a poor detailed description of the surface pressure distribution since the actual shape of the displacement body and its wake can depart significantly from the family of geometrically similar bodies used in the first trial solution. The first step towards obtaining a converged solution is thus to obtain a much more accurate representation of the potential flow pressure distribution on the displacement body. This task is equivalent to solving equations (13) and (14) for an arbitrary boundary shape, since the displacement body obtained from A. above will not in general have a simple analytic representation. An approximate combined numerical and analytical solution technique based on the boundary method has been developed for this purpose and is described in subsection 4(b).

2. The potential flow pressure distribution on the first order displacement body obtained in 1. above is now mapped back to the surface of the original body using equation (11). The momentum integral equation formulation of equation (10) is now solved again using this new pressure distribution.

3. The new solution for the displacement thickness distribution found in 2. is now added on normally to the surface of the original body, in the same manner as before, to obtain the second order approximation for the displacement body.

4. Steps 1, 2 and 3 are now repeated to obtain the third and higher order approximations to the displacement body until convergence in either body shape or surface pressure distribution is achieved to within predetermined limits.

In accord with the preceeding solution outline the approximate

equation for the viscous layer is the integral of equation (10)

$$\frac{\tau_w}{\rho} = \frac{d}{dx}\ (U^2\theta) + \delta^* U\frac{dU}{dx} \tag{15}$$

where τ_w is the wall shear and

$$\theta(x) = \int_o^\delta \frac{u}{U}\left(1-\frac{u}{U}\right)\,dy \tag{16}$$

is the momentum thickness. The velocity profile used is the Pohlhausen (1921) fourth order polynomial profile,

$$\frac{u}{U} = (2+\Lambda/6)\,\frac{y}{\delta} - \frac{\Lambda}{2}\left(\frac{y}{\delta}\right)^2 + \left(-2+\frac{\Lambda}{6}\right)\left(\frac{y}{\delta}\right)^3 + \left(1-\frac{\Lambda}{6}\right)\left(\frac{y}{\delta}\right)^4 \tag{17}$$

where the shape factor Λ is defined by

$$\Lambda = \frac{\delta^2}{\nu}\frac{dU}{dx}$$

This profile provides a reasonable description up to separation and a solution of undetermined accuracy beyond the separation point. It is important to note that there is a marked difference between separated flow velocity profiles in the present study and those at high Re where there is a thin boundary layer like structure both in the reversed flow near the wall and in the separated shear layers. The smoothly varying polynomial profile is much more likely to provide at least a qualitatively passable description of the separated thick viscous layers considered herein where the spread of vorticity is much more diffuse.

4(a). First trial solution for the forward stagnation point

To elucidate the solution procedure described under step 1. of the first trial solution for the displacement body, we consider the stagnation point flow on a circular cylinder of unit radius. The geometrically

similar displacement bodies considered are concentric cylinders of radius $r^* = 1 + \delta^*$. Both δ^* and dU/dx at the forward stagnation point are unknown. The potential flow solution for the velocity on the surface of a geometrically similar displacement cylinder of radius r^* is

$$U = 2U_\infty \sin\theta^* \tag{19}$$

where θ and θ^* are related by $r\theta = r^*\theta^*$ from equation (11). The velocity gradient at the forward stagnation point on the original body surface obtained from equation (19) and the pressure transformation (11) is

$$\frac{dU}{dx} = \frac{2U_\infty}{1+\delta^*} \tag{20}$$

It is well known that the solution of equation (15) at the forward stagnation point for a fourth order Pohlhausen profile leads to a cubic equation for the shape factor whose physically meaningful root is $\Lambda = 7.052$, see Schlichting (1968). The relationship between δ and δ^* for this profile is $\delta^* = \delta\left(\frac{3}{10} - \frac{\Lambda}{120}\right)$. Substituting these last two results into equations (18) and (20) and eliminating dU/dx as an unknown, one obtains

$$\frac{\delta^{*2}}{1+\delta^*} = \frac{1.701}{Re}\ , \tag{21}$$

where Re is the free stream Reynolds number based on the diameter of the original cylinder. The physically realizable solution for $\delta^*(0)$ is

$$\delta^*(0) = \frac{.856}{Re} + \sqrt{\frac{1.701}{Re} + \left(\frac{.856}{Re}\right)^2} \tag{22}$$

It is interesting to observe that for Re >> 1 equation (22) can be developed as a power series in inverse half powers of the Reynolds number. This result

$$\delta^*(0) = \frac{1.304}{Re^{1/2}} \left(1 + \frac{.657}{Re^{1/2}} + \frac{.213}{Re} + \ldots\right) \qquad (23)$$

is of the same form as one would anticipate from higher order boundary layer theory. The leading term in (23) is the same as one obtains from the solution for a two-dimensional stagnation point while the higher order terms are due to viscous layer displacement and curvature effects.

The solution procedure for other boundary shapes differs only in the expression for the surface velocity distribution (19).

4(b). Inviscid flow past the displacement body

The crucial step in the iterative approximation procedure used to obtain a converged solution is the development of a simple yet accurate approximate technique for determining the flow past non-analytic boundary shapes. In theory the exact solution for the two-dimensional streaming motion past an arbitrary cylinder can be represented by an appropriate surface distribution of line sources and sinks. Accurate approximation representations for smoothly contoured bodies can be obtained using internal source-sink distributions by applying the boundary method. The detailed application of the boundary method developed herein differs depending on whether the body is of low or high aspect ratio. In either case one starts with an unknown finite distribution of N sources and sinks of strength m_i located at positions x_i along the plane of symmetry of the body and placed in a uniform stream. The stream function for this flow

$$\Psi = U_\infty y + \sum_{i=1}^{N} m_i \left(\tan^{-1}\left(\frac{y}{x-x_i}\right) - \pi\right) \tag{24}$$

automatically satisfies equation (13). Far upstream of the body each term in the finite series vanishes and (24) reduces to the stream-function for a uniform stream. Far downstream the $\Psi = 0$ streamline representing the displacement body asympotically approaches a far wake of uniform thickness d determined by the net source strength:

$$d = \frac{\pi}{U_\infty} \sum_{i=1}^{N} m_i \tag{25}$$

The essential feature of the present application of the boundary method is that one wishes to satisfy the boundary conditions (14) along the arc of the displacement body through a judicious selection of the unknown constants x_i and m_i. This is accomplished by setting $\Psi = 0$ in equation (24) at discrete points along the displacement surface $r^*(x^*)$. The arbitrariness of the method lies in the selection of the boundary points and the choice as to which values of x_i and m_i one wishes to leave unspecified. After considerable numerical experimentation two different procedures have been adopted in the present study. For the flow past low and moderate aspect ratio finite bodies, such as the circular cylinder and ellipses treated herein, it was observed that a surprisingly good representation of the desired $\Psi = 0$ boundary shape could be obtained using only four equally spaced boundary points between flow attachment and separation if both m_i and x_i were left unspecified and the series in equation (24) was truncated at $N = 2$. A typical curve fit is discussed later in Figure 5. The unusually good agreement obtained using only two source-sink singularities can be

attributed to the smoothly varying contour of the displacement body and the fact that the detailed geometry of the wake downstream of the body is not important as far as the surface pressure distribution is concerned, and thus does not have to be accurately modeled.

For the flow past semi-infinite bodies, such as the family of parabolas considered herein or high aspect ratio finite bodies, many more boundary points are required for an accurate curve fit in which the $\Psi = 0$ streamline does not exhibit wavelike undulations. The solution of the matrix of equations derived from (24) when many boundary points are required is extremely tedious if both m_i and x_i are treated as unknowns since the x_i appear non-linearly as the arguments of the inverse tangent functions. A much simpler procedure for these extended bodies is to specify the source-sink locations x_i and leave only the values of m_i to be determined since these constants appear linearly in equation (24). A convenient but arbitrary selection of boundary points and source locations in this procedure is to position the singularities directly below the boundary points in one to one correspondence. Employing standard matrix reduction schemes for systems of linear equations, one can easily handle as many as 100 boundary points using less than a minute of computer time.

5. Parabolic Cylinders

As the first application of the new approximate theory described in Sections 3 and 4, we consider the uniform viscous flow past a parabolic cylinder whose surface is defined by

$$y^2 = 4(1+x) \tag{26}$$

at various Reynolds numbers. This simple body shape, for which separation

does not occur, provides a convenient geometry to test the basic hypotheses of the new model with existing finite difference solutions of the Navier-Stokes equations, Davis (1972), and conventional boundary layer theory.

The family of geometrically similar parabolas used to generate the surface pressure distribution in equation (15) for the construction of the first trial guess for the displacement body is given by

$$y^2 = 4c^2 (x+c^2) \tag{27}$$

For $c = 1$ this reduces to equation (26) whereas for $c > 1$ one obtains a family of geometrically enlarged parabolas with a common focal point at the origin.

The transformation $w = u + iv$ where

$$w = - \sqrt{z'} + ic \tag{28}$$

maps the flow past the parabolic surfaces described by equation (27) in the complex z plane into a two-dimensional stagnation point flow in the complex w plane, the parabolic surfaces mapping into the v axis. The solution for the complex potential $F(w) = \Phi + i\Psi$ in the transformed w plane is $F(w) = U_\infty w^2$. Differentiating this result, one obtains for the speed q in the z plane

$$q = \left| F'(z) \right| = U_\infty \sqrt{1 + \frac{c^2}{r} - \frac{2c}{\sqrt{r'}} \sin \left(\frac{\pi-\theta^*}{2}\right)} \tag{29}$$

where the angle θ^* is measured from the forward stagnation point. From (29) the speed along the surface of the parabolas defined by equation (27) is:

$$q = U = U_\infty \cos\left(\frac{\pi-\theta^*}{2}\right) \tag{30}$$

The potential flow solution (30) replaces equation (19) in the first trial solution for the forward stagnation point flow and is also used to approximate the local pressure gradient in equation (10) or (15) as described in step 2 of the procedure for determining the first trial solution for the displacement body. In applying the pressure mapping described by equation (11) we have related the polar angles θ and θ^* measured from the forward stagnation point along the original and effective displacement body surface by the arc length formula

$$\int_o^{\theta^*} \sqrt{r^{*2} + \left(\frac{dr^*}{d\theta}\right)^2}\, d\theta = \int_o^{\theta} \sqrt{r^2 + \left(\frac{dr}{d\theta}\right)^2}\, d\theta \qquad (31)$$

In the discussion beneath equation (11) it was mentioned that the pressure distribution as a function of distance along the original and displacement surfaces are equal to within an additive constant due to the viscous loss in total pressure along the stagnation streamline. To determine this constant we consider the two-dimensional Navier-Stokes equation in the vicinity of the stagnation point. In this local region the normal velocity component is independent of x and the normal momentum equation reduces to

$$v\frac{dv}{dy} = -\frac{1}{\rho}\frac{\partial p}{\partial y} + \nu\frac{\partial^2 v}{\partial y^2} \qquad (32)$$

The integral of equation (32) between the wall and the edge of the viscous layer denoted by the subscript e is:

$$\frac{v_e^2}{2} = -\frac{1}{\rho}(P_e - P_w) - \nu\frac{\partial v}{\partial y}_e \qquad (33)$$

Combining this last result with the Bernoulli equation applied along the stagnation streamline in the inviscid flow, one obtains the following expression for the increase in wall pressure coefficient due to viscous losses:

$$C_{pw} = \frac{P_w - P_\infty}{\rho U_\infty^2} = \frac{1}{2}\left(1 + \frac{4}{Re}\frac{\partial v_e}{\partial y}\right) \tag{34}$$

The Reynolds number here is based on the radius of curvature R_o at the forward stagnation point. For a parabola this is equal to twice the focal radius.

In Figures 2 and 3 we have compared the results of the present approximate model with the numerical Navier-Stokes solutions of Davis (1972) for the surface pressure distribution on a parabola at a Reynolds number of 10 and 100. The importance of the viscous pressure losses predicted by equation (34) and the streamwise stretching of the body surface coordinate required by the pressure hypothesis (11) are particularly evident for the Re = 10 flow. The potential flow pressure distribution for the inviscid flow past the original body considerably lags the Navier-Stokes solution for the surface pressure over the entire body. The inclusion of viscous layer displacement effects using conventional first order boundary layer theory to construct the displacement body and no stretching produces only a small improvement in this retarded pressure development, while the inclusion of the viscous pressure losses from equation (34) serves only to elevate the surface pressure distribution in the forward stagnation region. A very substantial improvement in the agreement with the exact Navier-Stokes solutions is achieved, however, for both the first and second order approximations to the displacement body using the new pressure stretching

hypothesis and the viscous correction for the pressure loss across the layer. The first order approximation is based on the family of geometrically similar parabolas (27) in which the pressure gradient is mapped back to the body surface in accord with equation (31). The second order approximation is based on the stream function fit of equation (24) to the first order approximation for the displacement body. A typical curve fit employing 25 boundary points is able to generate a $\psi = 0$ boundary streamline which is nearly indistinguishable from the desired shape.

At first glance the very close agreement between the first and second order approximate solutions for the surface pressure distributions in Figure 2 might seem surprising in view of the substantially different manner in which they were calculated. The reason for this close agreement is evident from Figure 4 where we have plotted the stream function fit to the second order displacement body. The first and second order displacement bodies are almost identical; one would therefore conclude that the displacement thickness distribution predicted by the potential flow past the geometrically similar family of parabolas is nearly the same as that predicted by equation (24). Also shown in the figure is the displacement body obtained when the integral equation for the viscous layer (15) is solved using the potential flow past the original body and the displacement body, constructed in the conventional manner.

6. Circular Cylinders

A much more rigorous test of the new approximate theory is the flow past a circular cylinder in the Reynolds number range 5 to approximately

60 where a closed steady wake separation bubble is observed in both experiments and numerical Navier-Stokes solutions.

The solution scheme for circular cylinders has already been described in detail in section 4. Equation (15) when integrated using the surface velocity distribution (19) yields the first trial solution for the displacement body. This body, for a Reynolds number of 10, is illustrated in Figure 5. Also shown in this figure is the approximate solution for the inviscid flow past this displacement body obtained using equation (24) with N=2, as discussed in section 4(b). The four match points used are denoted by asterisks. The last asterisk denotes the point of separation. The stream function fit, which has been continued past the point of separation, approaches the asymptotic wake width predicted by equation (25). The surprisingly good approximation that can be obtained for the displacement body using only two source-sink singularities is clearly evident in this figure.

Figure 6 shows the displacement bodies obtained by the successive iteration procedure described in 4B. The significant deviation between the first and higher order approximations arises because the second and higher order approximations predict separation at a smaller angle ϕ from the rear stagnation point. This is shown in Figure 7 where we have compared the theoretically predicted location of separation as a function of Reynolds number with available experimental data and Navier-Stokes solutions. The present first order approximation provides slightly better agreement than the second and higher order approximations at the higher Reynolds numbers, whereas the latter nearly exactly predict Taneda's (1956) experimentally observed Reynolds number for incipient separation. The difference between second and higher order

approximate solutions is in general very small as observed in Figure 6.

The crucial test of the new theory is whether it can accurately predict the surface pressure distribution on the cylinder. Figures 8-10 illustrate the excellent results obtained using the new pressure hypothesis equations (9) or (11). Also shown in these figures is the surface pressure predicted by standard second order boundary layer theory using the conventional construction of the displacement body. In the present study we have been primarily concerned with determining the surface pressure up to the point of separation, since the fourth order polynomial profile description given by equation (17) is a poor detailed representation of the flow in the separated flow region. The pressure at the rear stagnation point on the cylinder could, therefore, not be used as the zero reference value as is commonly done in the numerical Navier-Stokes solutions. Instead we have chosen the pressure at the forward stagnation point as predicted by numerical Navier-Stokes solutions as the reference pressure for all the circular cylinder calculations.

The dramatic improvement over second order boundary layer theory in the prediction of the surface pressure distribution noted in Figures 8-10 using the new pressure hypothesis can be attributed to the greatly improved representation of the first order displacement body that results from the present solution procedure. In the conventional boundary layer theory, where the first order solution for the displacement body is based on the potential flow past the original body surface, separation occurs at approximately 108 degrees from the forward stagnation point independent of Reynolds number. In contrast, the stretching of the body coordinate implicit in the new pressure hypothesis leads in the first

trial solution to a reasonable prediction of the separation point location as observed in Figure 7. The importance of the new pressure hypothesis is clearly demonstrated in Figure 11 where we have compared the angular location of the minimum surface pressure predicted by second order boundary layer theory and the present approximate theory with available Navier-Stokes numerical solutions.

In Figure 12 we have shown a typical surface vorticity distribution. As noted in the earlier work of Gluckman (1971) and Werle and Wornom (1972) and mentioned in the introduction, the boundary layer equations yield reasonable predictions of the surface vorticity distribution provided the surface pressure distribution is accurately known. Figures 13 and 14 show the velocity profile development in the viscous layer and the growth of the boundary layer outer edge up to separation at Reynolds numbers of 10 and 60 respectively. Figure 13 also shows the shape that the fourth order polynomial profile assumes shortly downstream of separation. No difficulty is encountered in integrating the momentum integral equation (15) through separation using the interaction pressure field. Thus if a more accurate family of separated flow profiles is constructed one should be able to obtain reasonable solutions for the wake separation bubble. This possibility is currently being studied.

7. Additional Results and Comments

Available published two-dimensional numerical Navier-Stokes solutions have primarily focused on the parabolic and circular cylinder geometries already discussed and the conformal family of semi-infinite bodies with a shoulder treated by Davis and co-workers. Based on the derivation presented in section 2 the approximate theory described herein

is confined to smoothly contoured bodies whose shoulder radius of curvature does not vary rapidly over a distance comparable to the local boundary layer displacement thickness. Other unpublished two-dimensional numerical Navier-Stokes solutions for which the present theory is applicable have been privately communicated to the author. S.C.R. Dennis has recently examined the incipient Reynolds number for separation on an elliptic cylinder whose aspect ratio of major to minor axis (major axis oriented parallel to the flow direction) is 5.0. The numerical results indicate that the Reynolds number for incipient separation based on the major axis dimension is nearly 200 compared to a value of only 6 for a circular cylinder, see Figure 7. This interesting result prompted the author to undertake a study of the effect of aspect ratio on the angle of separation ϕ for various elliptic cylinders. The angle ϕ is measured from the rear stagnation point to the radius vector from the geometric center of the body. These results using the new approximate theory are shown in Figure 15. Incipient separation for an elliptic cylinder whose aspect ratio is 5.0 occurs according to the present theory at a Reynolds number of approximately 100. While this value appears to differ significantly from that found by Dennis, one observes in Figure 15 that the separation angle at a Reynolds number of 200 is still only a few degrees. The wake separation bubble would, therefore, be very small and difficult to detect in any event.

The new pressure hypothesis and approximate theory described herein have also been applied to a variety of semi-infinite and finite three-dimensional axisymmetric bodies and is reported in Chapter III. The agreement with available numerical Navier-Stokes solutions for the flow

past paraboloids of revolution, spheres and Prolate Spheroids is on a par with the two-dimensional results presented herein.

8. REFERENCES

Acrivos, A., Snowden, D.D., and Petersen, E.E., 1965, J. Fluid Mech., 21, 737.

Apelt, C.J., 1961, Aero. Res. Council Rep. and Mem. no. 3175.

Batchelor, G.K., 1967, "Fluid Dynamics", Cambridge Univ. Press.

Briley, W.R. and McDonald, H., 1974, "Numerical Prediction of Incompressible Separation Bubbles", United Aircraft Res. Lab. Rep. No. N110887-3.

Catherall, D. and Mangler, K.W., 1966, J. Fluid Mech., 26, 163.

Davis, R.T., 1972, J. Fluid Mech. 51, 417.

Davis, R.T., 1974, "A Study of the Use of Optimal Coordinates in the Solution of the Navier-Stokes Equations", Univ. of Cincinnati Rep. No. AFL 74-12-14.

Ghia, V. and Davis, R.T., 1974, AIAA J. 12, 1659.

Ghia, K.N., Ghia, V., and Tesch, W.A., 1975, AGARD Symposium on "Flow Separation", Gottingen, Germany, May 27-30.

Gluckman, M.J., 1971, Ph.D. Dissertation, The City University of New York.

Grove, A.S., Shair, F.H., Petersen, E.E., and Acrivos, A., 1963, J. of Fluid Mech. 19, 60.

Jain, P.C. and Rao, K.S., 1969, Phys. of Fluids Suppl. 2, II-57.

Kawaguti, M. and Jain, P., 1966, J. Phys. Soc. Japan 21, 2055.

Lighthill, M.J., 1958, J. Fluid Mech. 4, 383.

Pohlhausen, K., 1921, Zamm 1, 252.

Son, J.S. and Hanratty, T.J., 1969, J. Fluid Mech. 35, 369.

Takami, H. and Keller, H.B., 1969, Phys. of Fluids Suppl. 2, 12.

Taneda, S., 1956, J. Phys. Soc. Japan 11, 302.

Van Dyke, M., 1962, J. Fluid Mech. 14, 161.

Werle, M.J. and Wornom, S.F., 1972, Internat'l J. Eng'g. Sci., 10, 875.

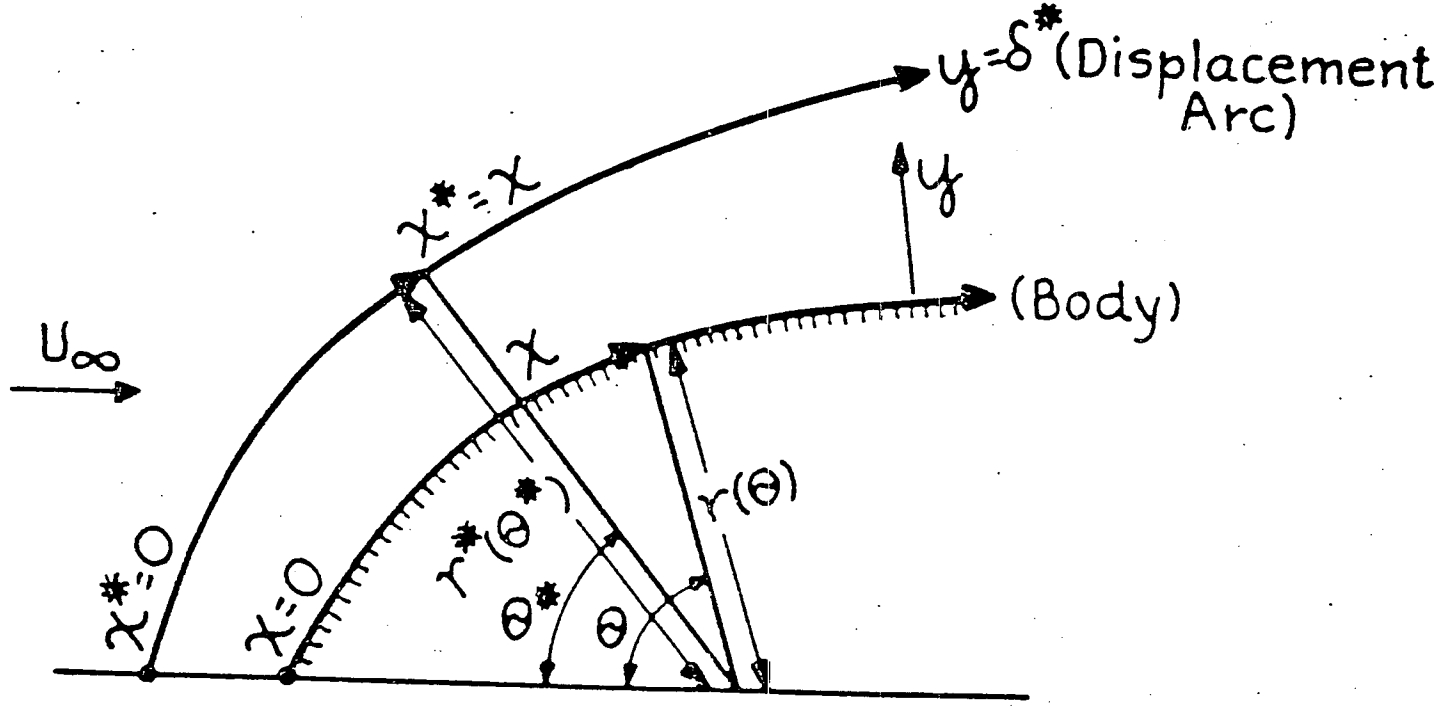

Figure 1. Boundary Layer Coordinate System.

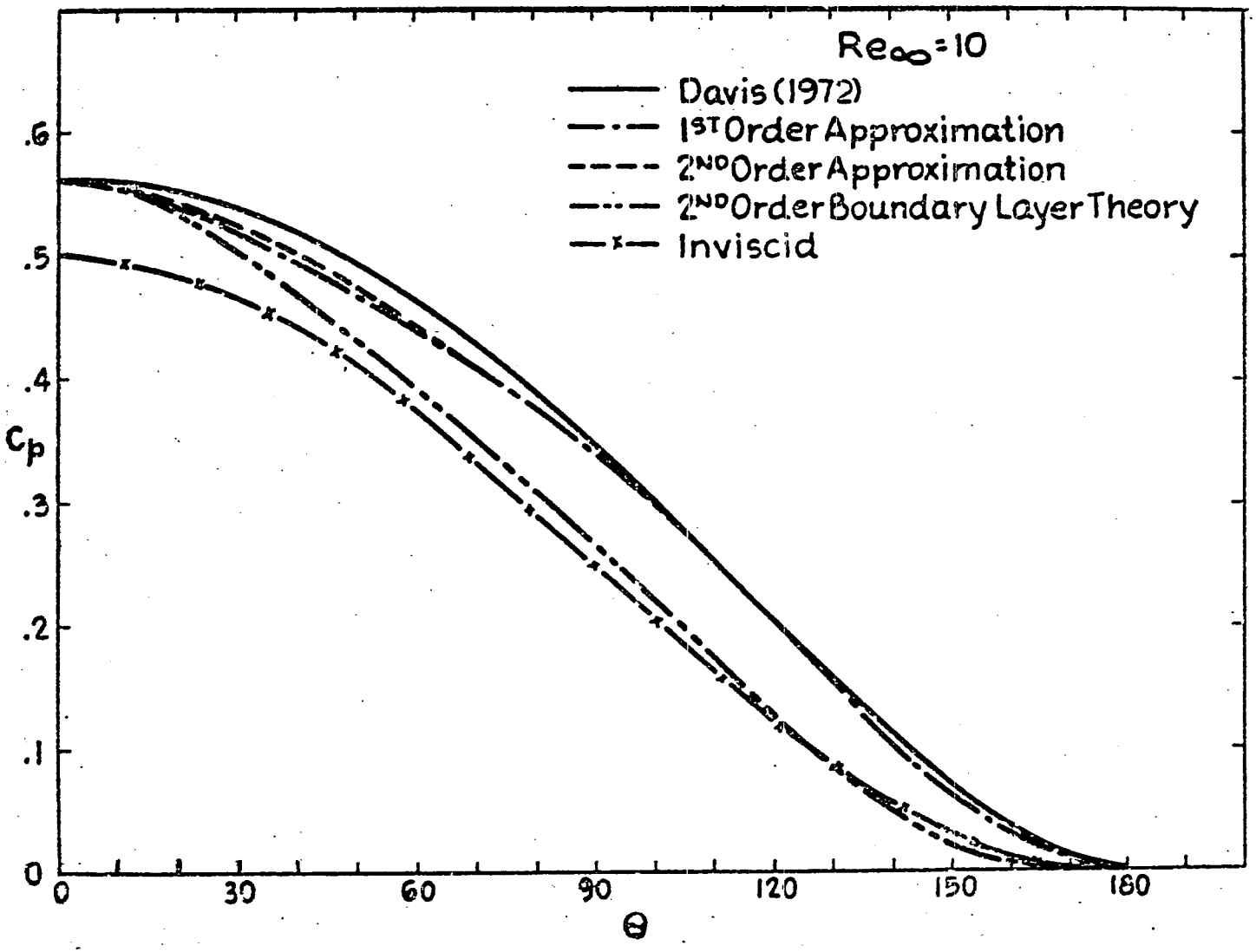

Figure 2. Surface Pressure Distribution for a Parabolic Cylinder.

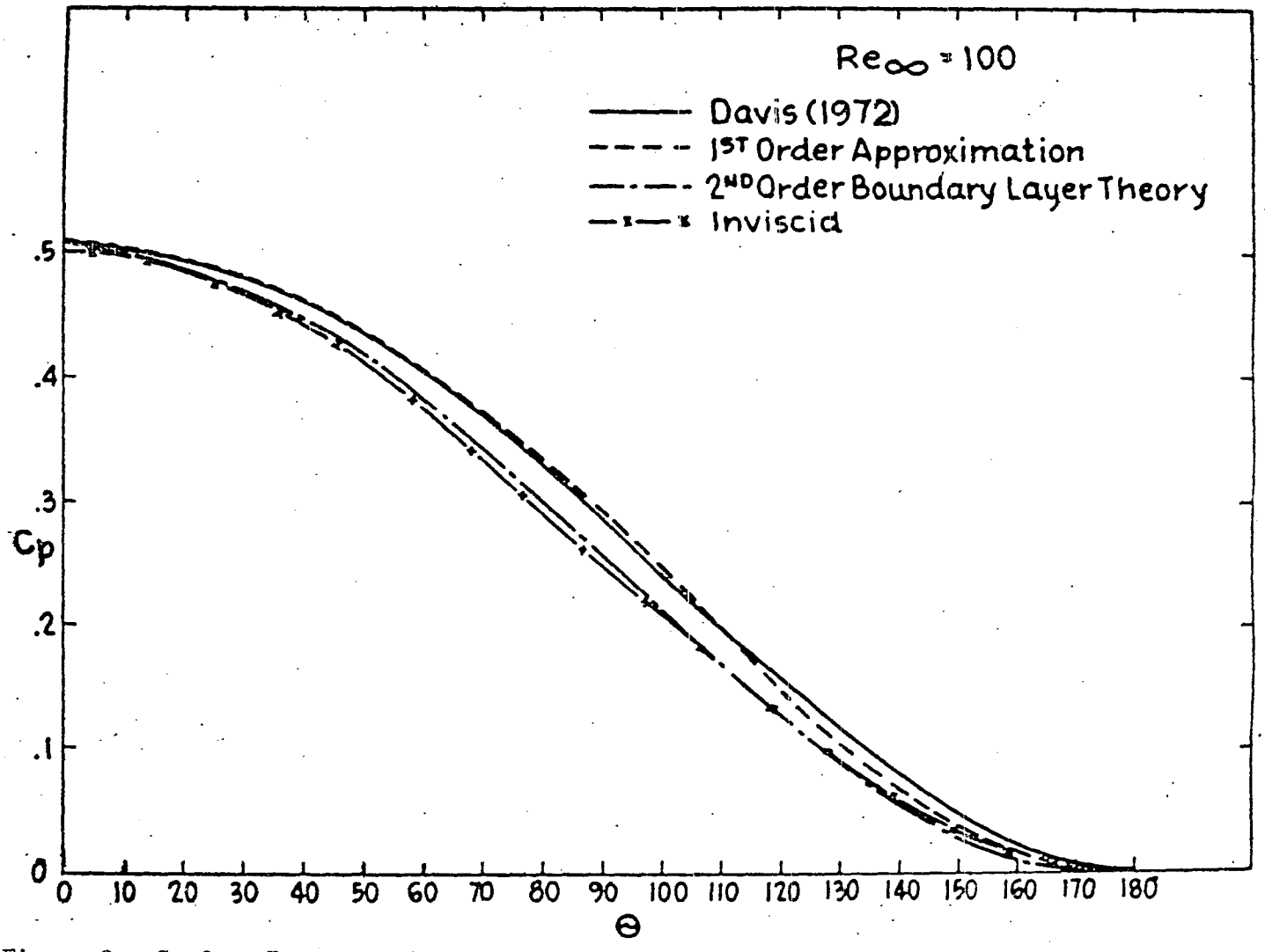

Figure 3. Surface Pressure Distribution for a Parabolic Cylinder.

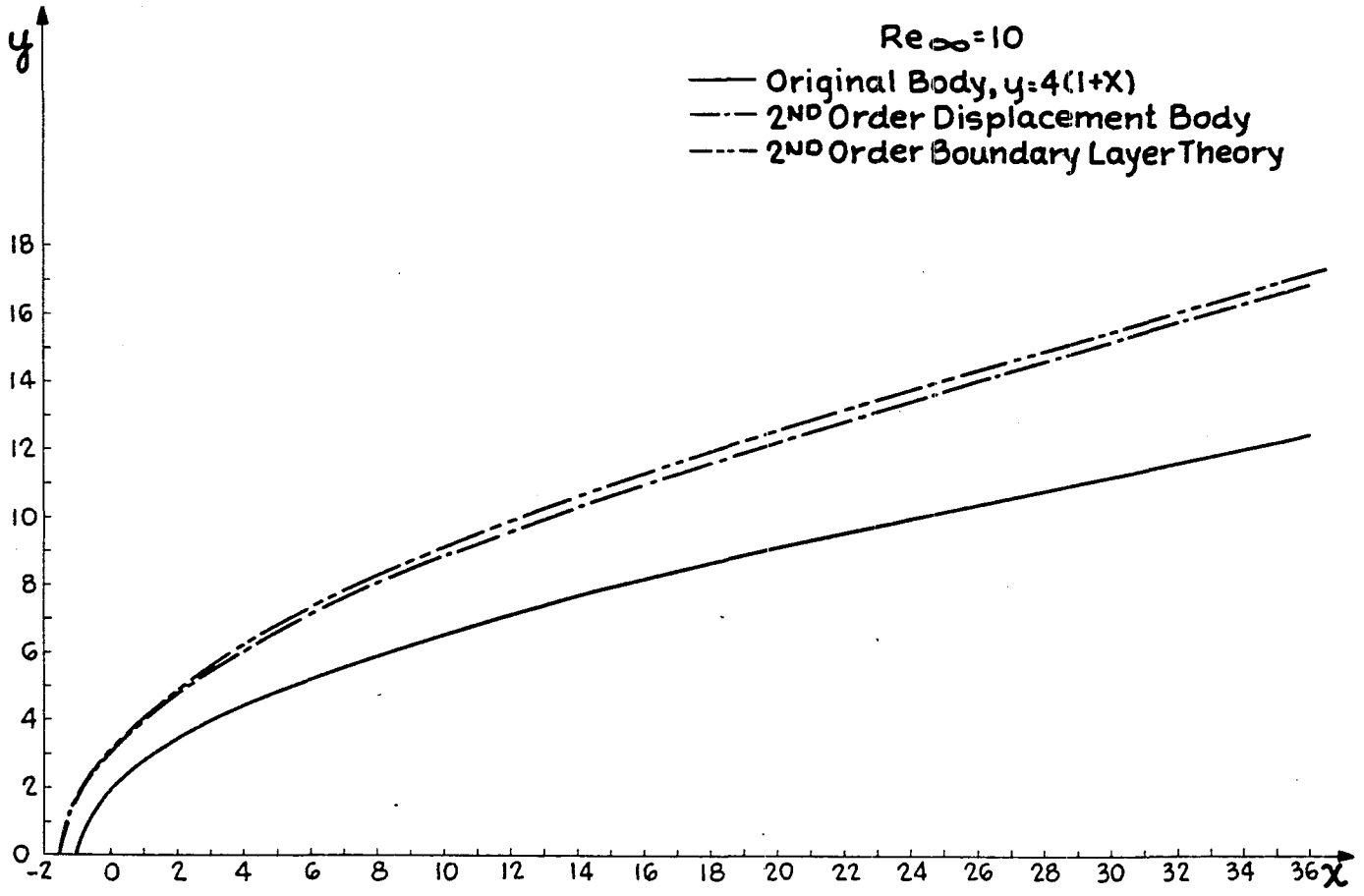

Figure 4. Stream Function Fit of the Displacement Body for a Parabolic Cylinder.

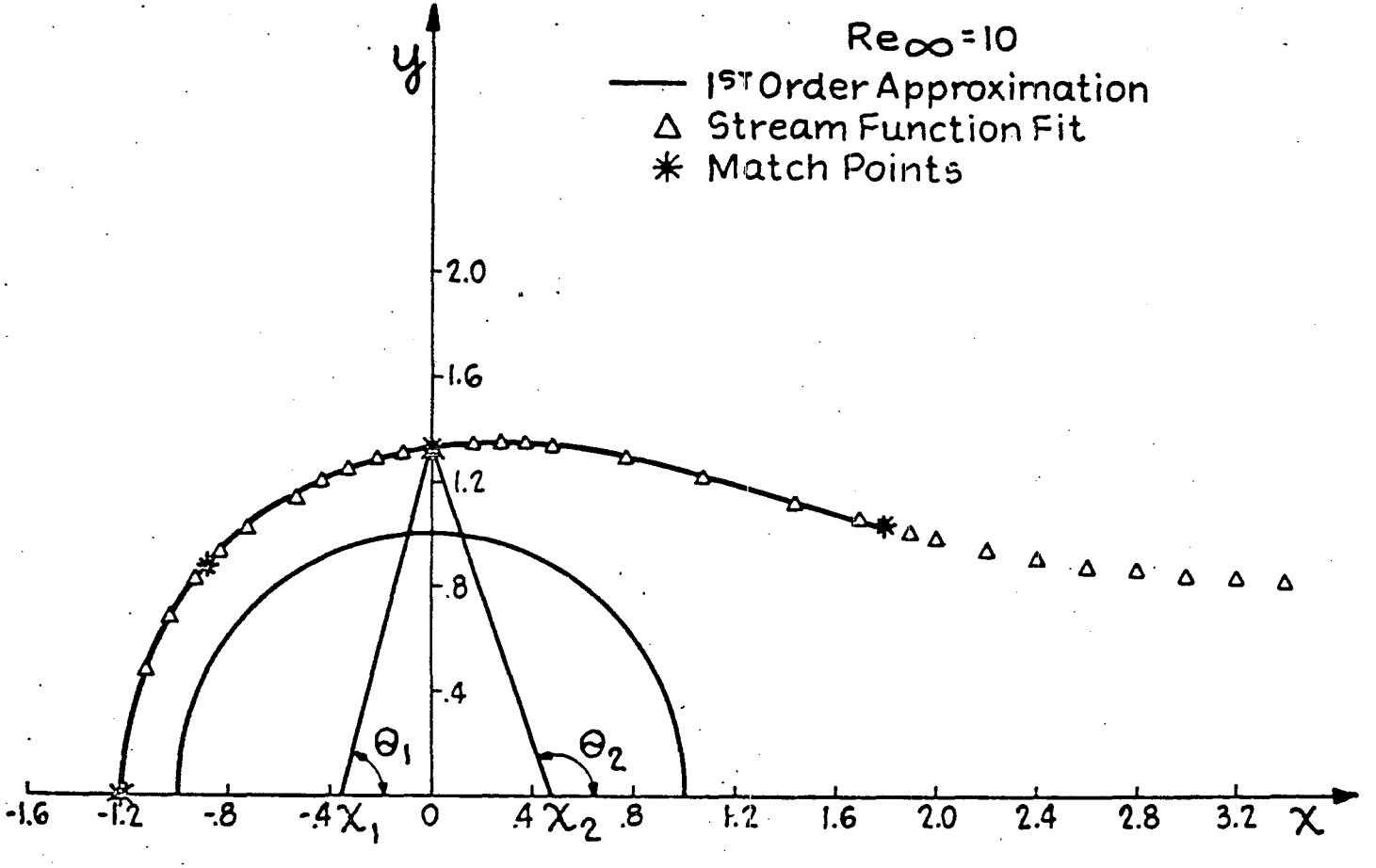

Figure 5. Stream Function Fit of the Displacement Body for a Circular Cylinder.

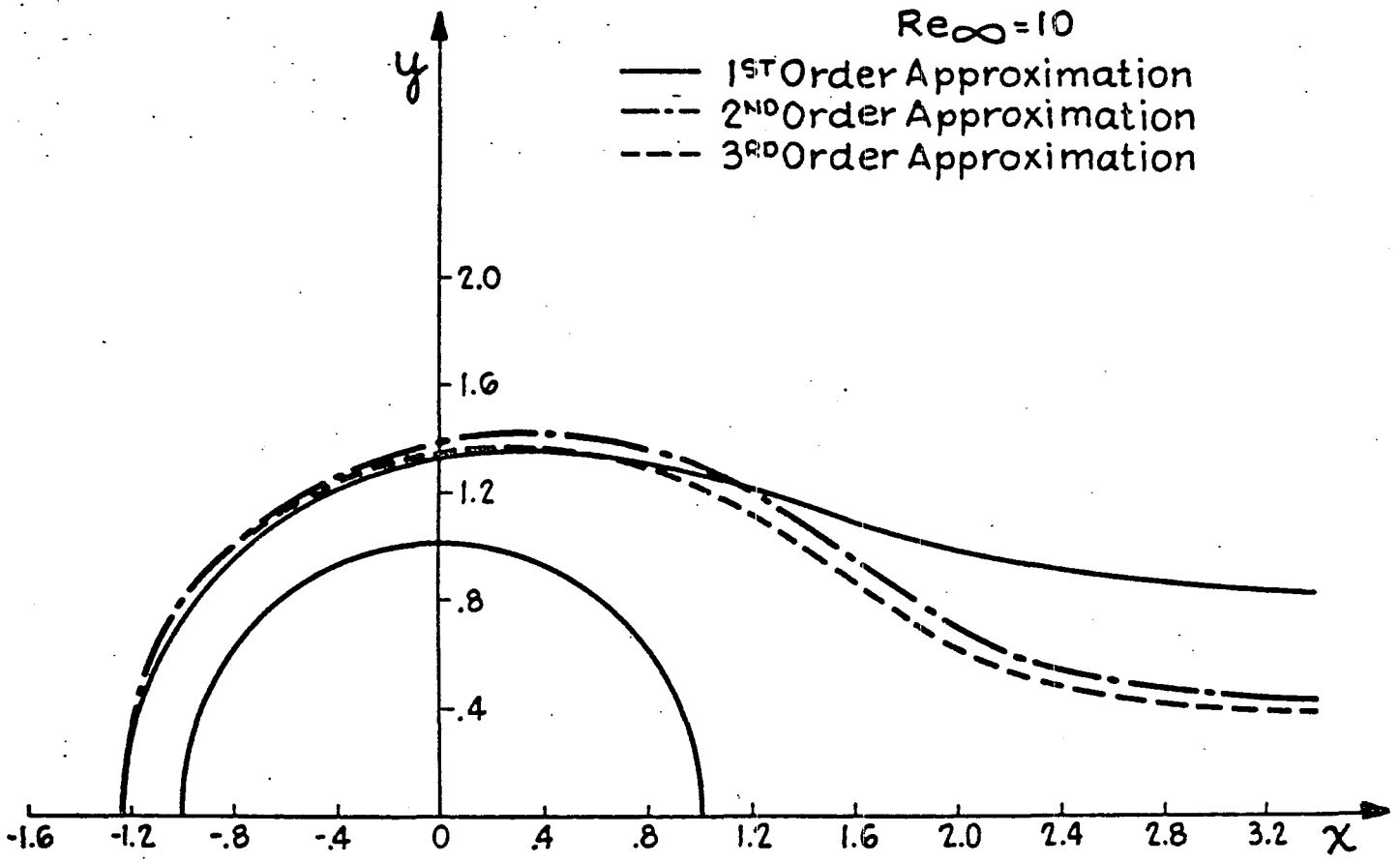

Figure 6. Successive Approximations for the Displacement Body for a Circular Cylinder.

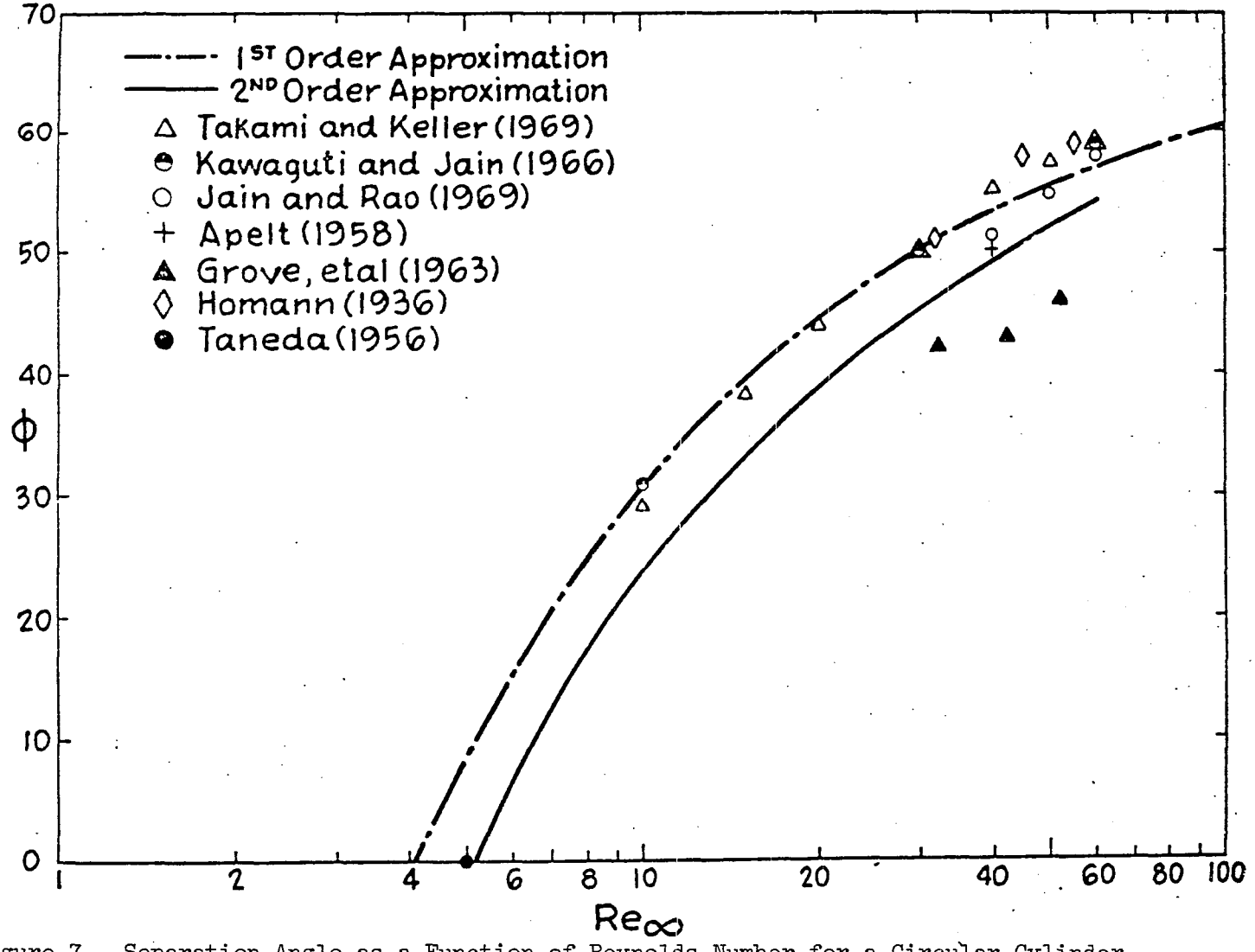

Figure 7. Separation Angle as a Function of Reynolds Number for a Circular Cylinder.

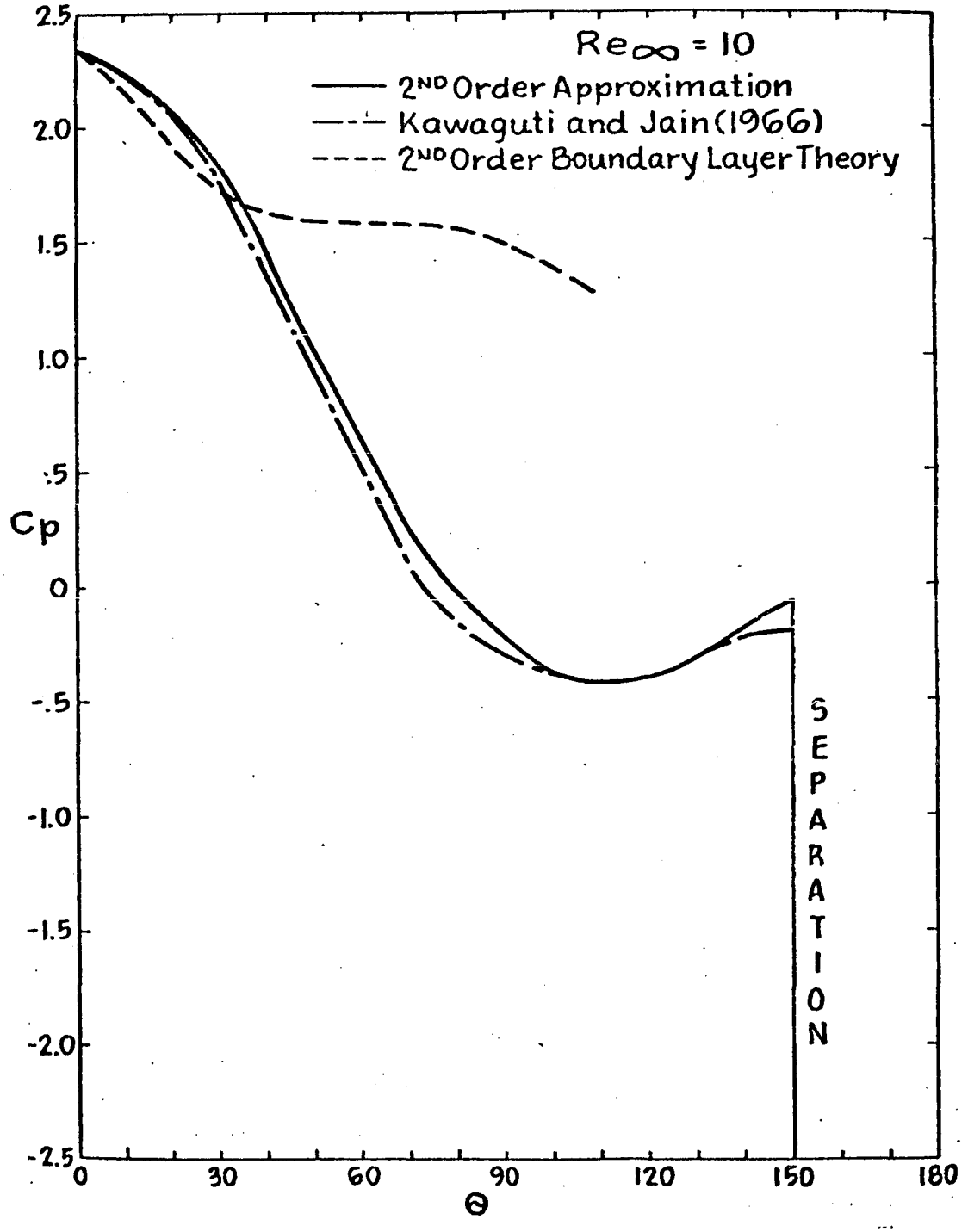

Figure 8. Surface Pressure Distribution around a Circular Cylinder.

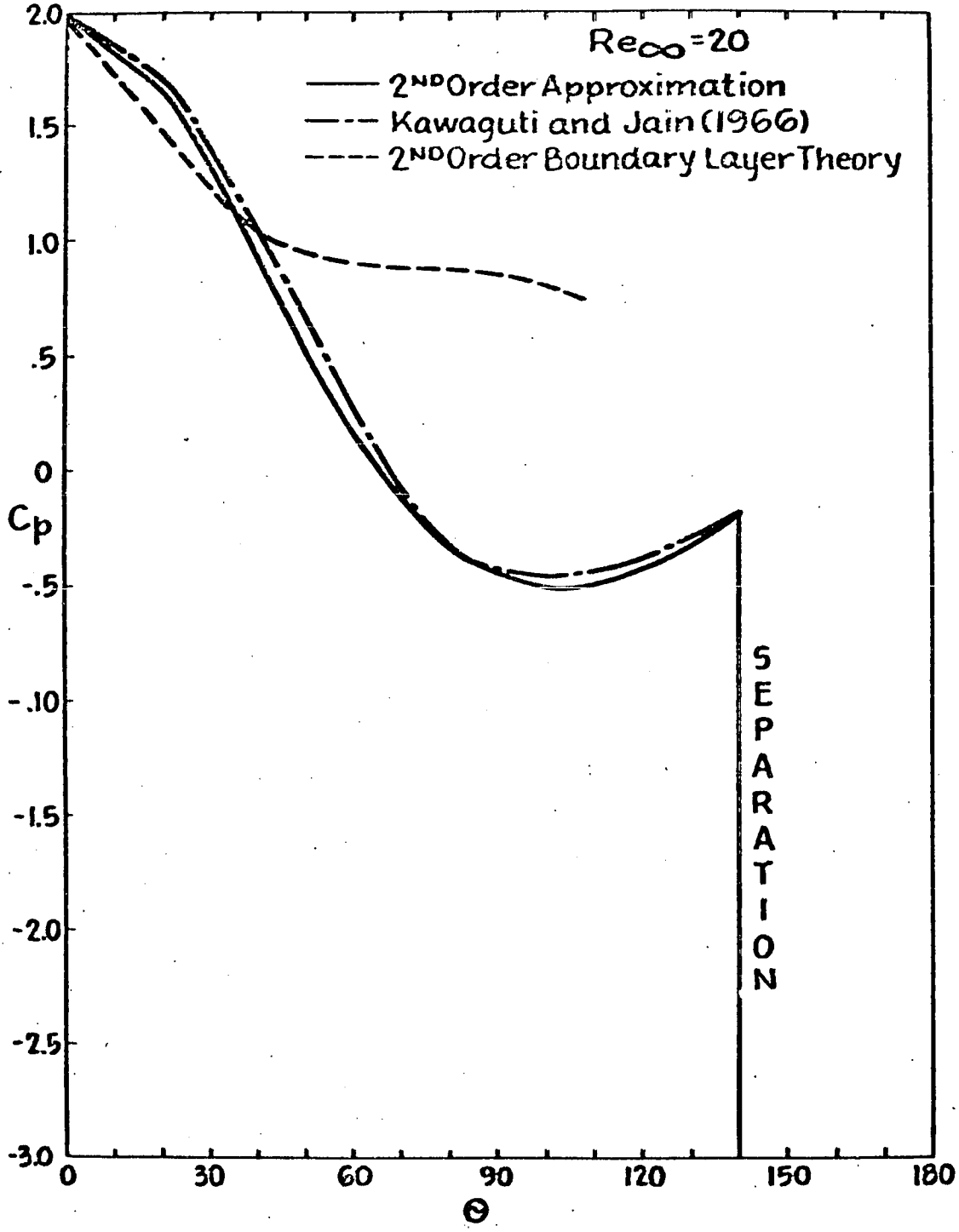

Figure 9. Surface Pressure Distribution around a Circular Cylinder.

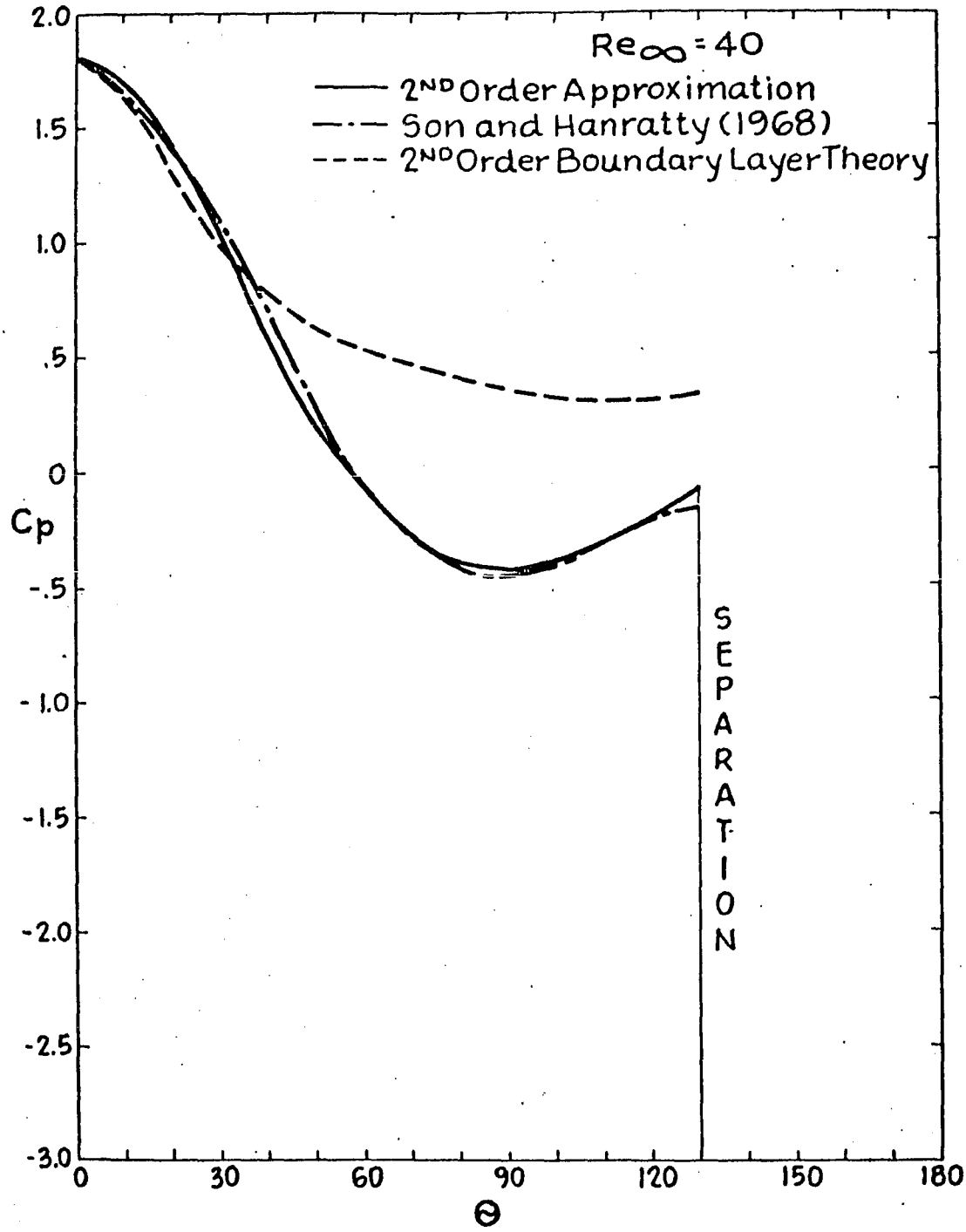

Figure 10. Surface Pressure Distribution around a Circular Cylinder.

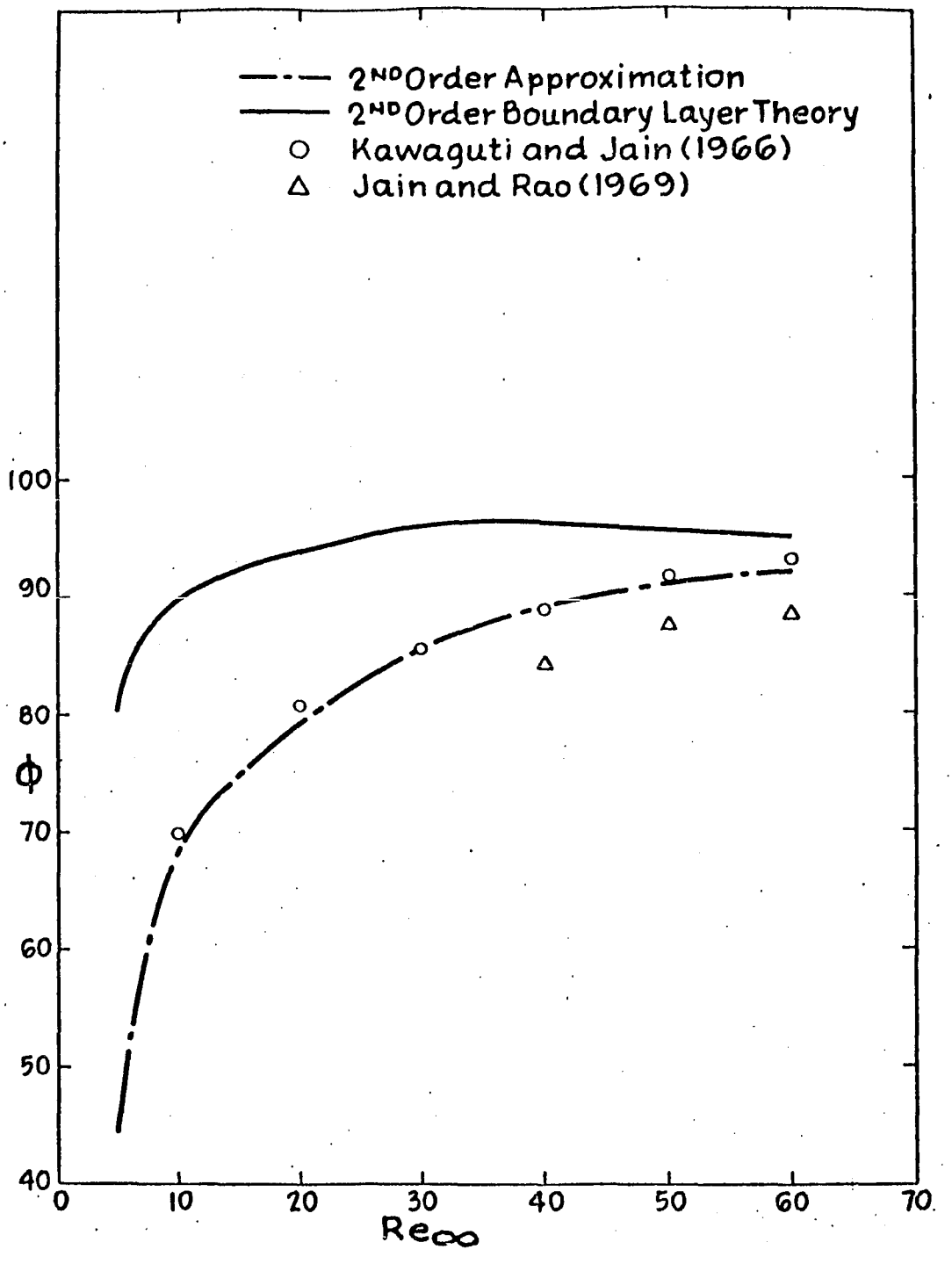

Figure 11. Angle of Minimum Surface Pressure for a Circular Cylinder.

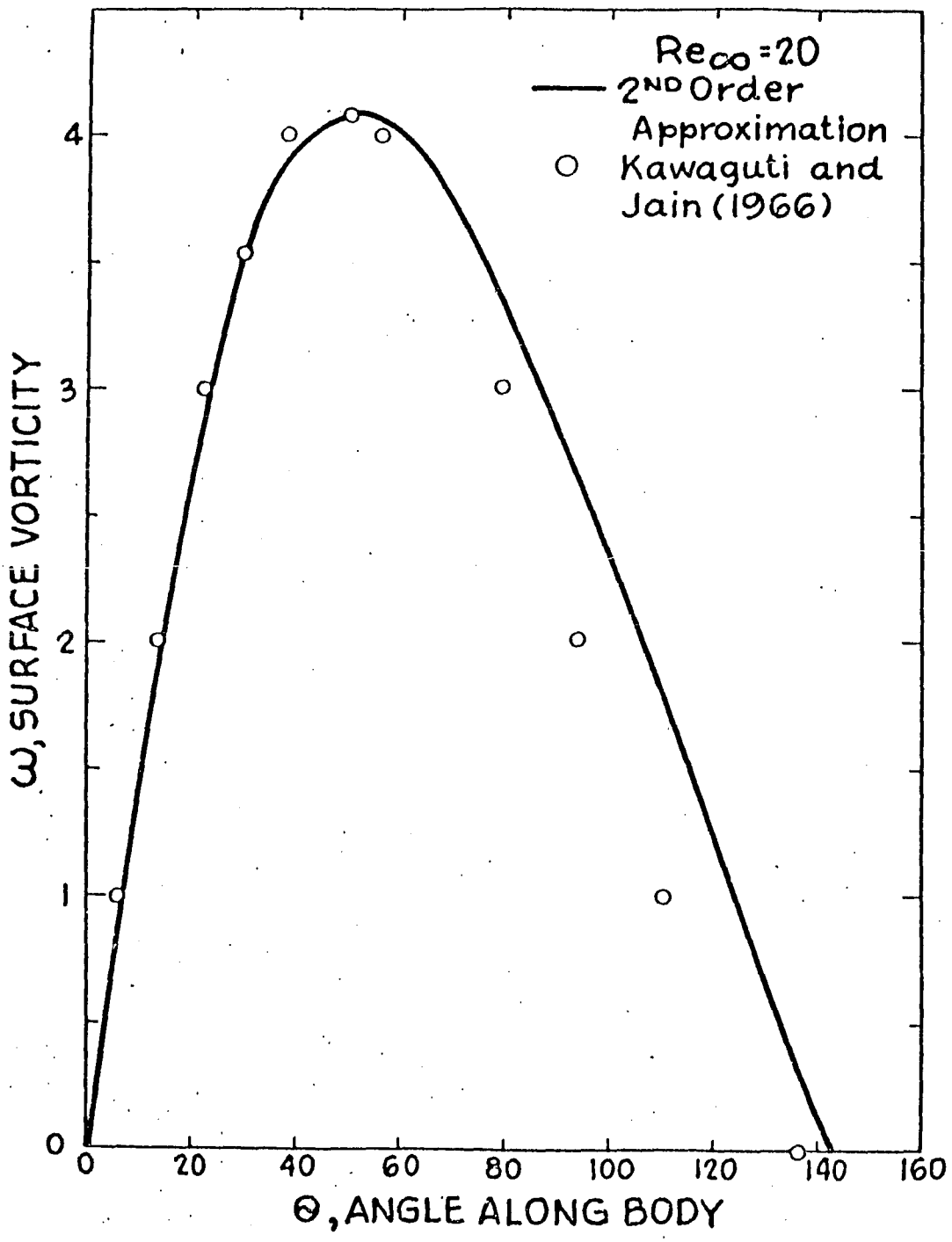

Figure 12. Surface Vorticity Distribution around a Circular Cylinder.

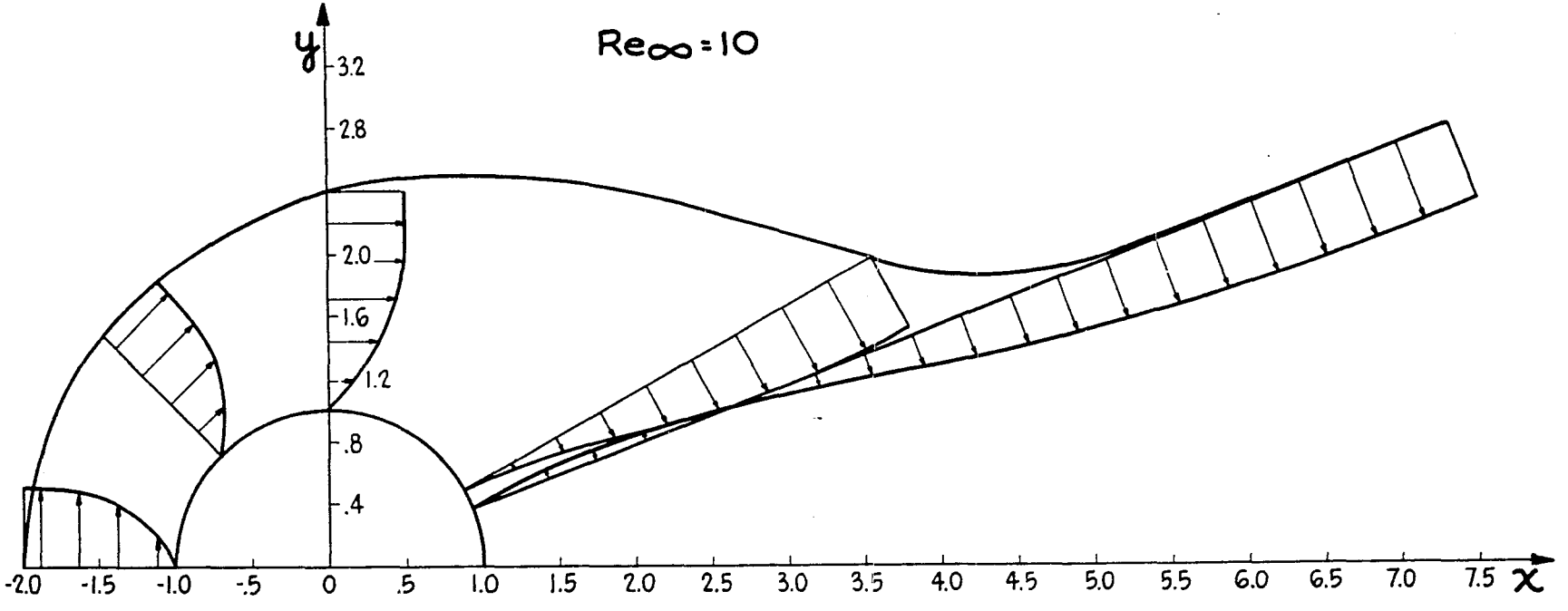

Figure 13. Velocity Profile Development in the Viscous Layer around a Circular Cylinder.

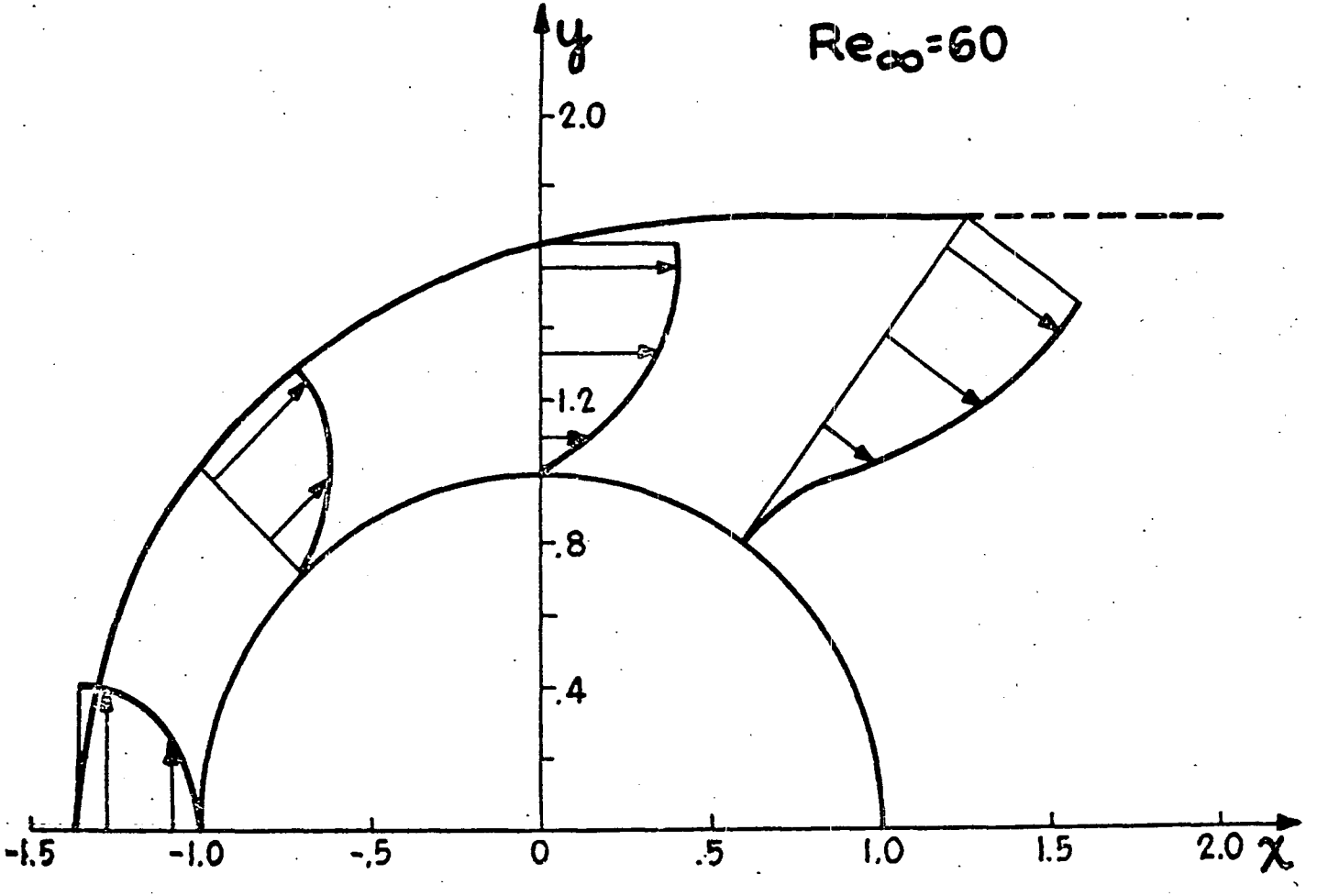

Figure 14, Velocity Profile Development in the Viscous Layer around a Circular Cylinder.

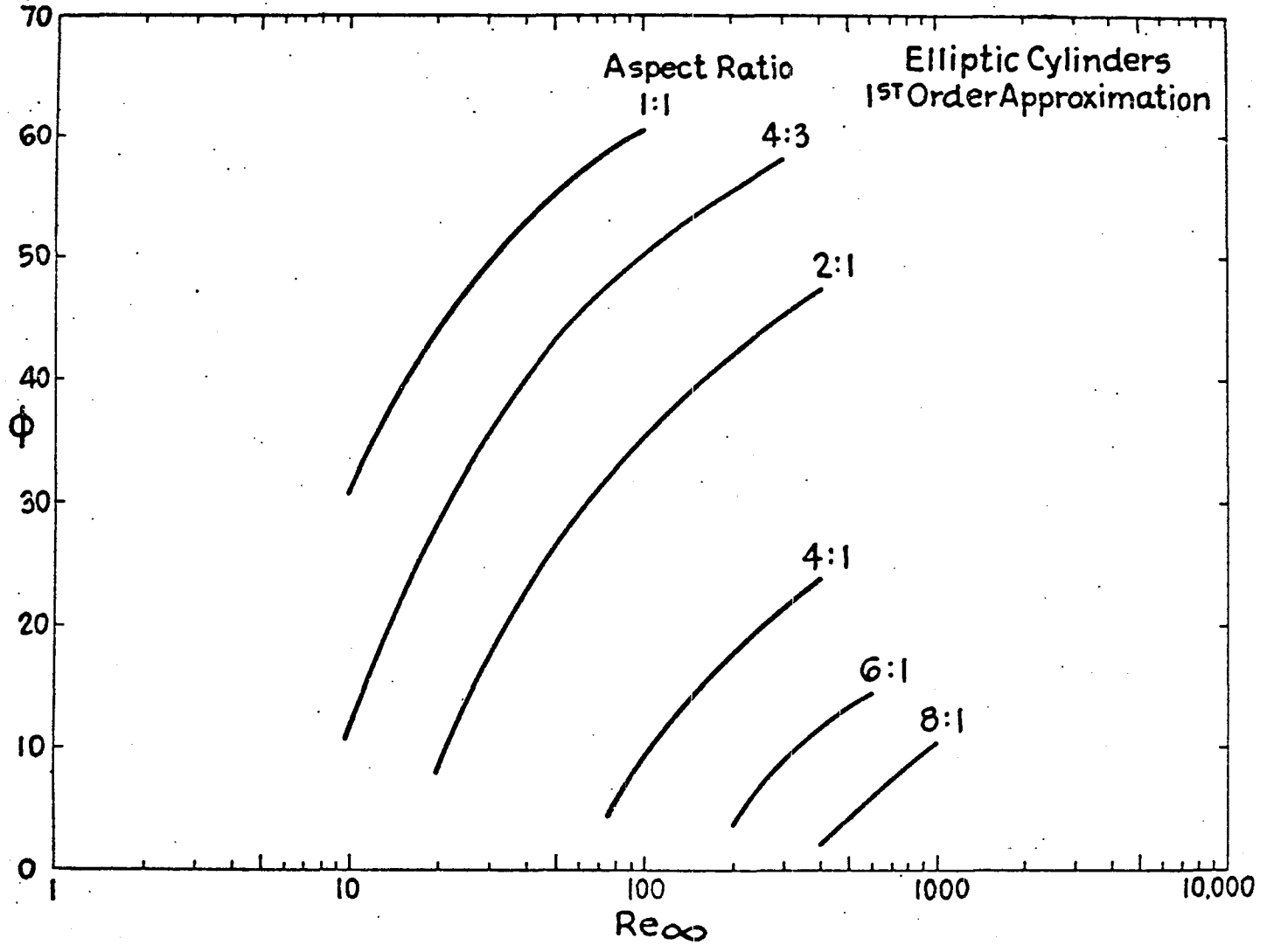

Figure 15. Separation Angle as a Function of Reynolds Number for Elliptic Cylinders, with Aspect Ratio as a Parameter.

CHAPTER III: AN APPROXIMATE THEORY FOR THE STREAMING MOTION PAST AXISYMMETRIC BODIES AT REYNOLDS NUMBERS FROM 1 TO APPROXIMATELY 100

1. Introduction

In Chapter II a new approximate theory was presented for the two-dimensional flow past smoothly contoured bluff objects in the intermediate Reynolds number regime $0(1) < Re < 0(10^2)$ where the viscous displacement of the outer flow produced by the body boundary layer and wake is of comparable magnitude to that produced by the original body and centrifugal effects in the thick viscous layer enshrouding the body can not be neglected. For finite bodies the upper limit of validity of the new approximate theory is determined by the condition that the wake separation bubble behind the body be steady and laminar. This limit has been experimentally observed to occur at Reynolds numbers of approximately 60 for circular cylinders and 130 for spheres Batchelor (1967). For semi-infinite bodies without separation the new theory provides a smooth transition to the solutions obtained from Prandtl's classical high Reynolds number laminar boundary layer theory.

Flows in the intermediate Reynolds number regime of interest in the present study have for long defied simpler theoretical treatment. Theoretical approaches to the low-Reynolds number end of the regime, which have been based on Oseen type linearizations, have not proved fruitful for $Re > 0(1)$ because of the inability of a constant linearizing velocity approximation to adequately describe the separation and wake formation phenomena on bluff bodies. Theoretical approaches from the upper end of the intermediate Reynolds number spectrum have been based largely on the concepts of higher order boundary layer theory, Van Dyke (1962). This theory similarly breaks down because it is a successive approximation scheme based on the potential flow past the

original body which in general will depart substantially from the effective displacement body with its wake at these Reynolds numbers.

At the heart of the new intermediate Reynolds number theory for axisymmetric flow described herein is a new simplifying pressure hypothesis derived in Chapter II that approximately relates the pressure gradient along the surface of the original body and the effective displacement body when centrifugal forces and viscous displacement interaction are considered. Earlier numerical studies by Gluckman (1971) and Werle and Wornom (1972) had demonstrated that if either experimentally measured or numerically generated Navier-Stokes surface pressure distributions were used to drive the Prandtl boundary layer equations, good predictions of the separation point location and surface vorticity distribution are possible for the flow past a circular cylinder for the entire range of Reynolds numbers where a steady wake separation bubble exists. This suggested that conventional boundary layer equations were still an adequate description of the growth of the viscous layer provided the surface pressure boundary condition was modified to take account of both the centrifugal forces that were omitted from the boundary layer equations and the effective enlargement of the body as seen by the inviscid outer flow. The fundamental question asked in Chapter II is thus, whether one could generate a displacement body using the Prandtl boundary layer equations which had the same pressure gradient along its displacement surface as the pressure gradient obtained from a higher order approximation to the Navier-Stokes equation in which centrifugal forces were retained in the governing equations. This effective pressure gradient would act through the centroid of vorticity, Lighthill (1958), of the local

velocity profile and produce the same displacement thickness distribution as the higher order set of equations.

In answer to the question just posed it is shown in Chapter II that the streamwise pressure gradient $\partial p/\partial s^*$ along the displacement surface using Prandtl boundary layer theory and the conventional construction of the displacement body, will be equal to the streamwise pressure gradient along the displacement body obtained by integrating a higher order approximation to the Navier-Stokes equations (equations (2) and (3) Chapter II) in which centrifugal forces and the normal pressure field are included provided

$$\frac{dp}{ds_w} = \left(\frac{R_w}{R^*}\right)\frac{\partial p}{\partial s_{wn}} - \frac{1}{Re^{1/2} R_w R^*}\left(\frac{\partial R_w}{\partial s_w}\right)\int_0^{n^*} u^2 dn \qquad (1)$$

Equation (1) relates the wall pressure gradient in the Prandtl boundary layer equation to the actual wall pressure gradient dp/ds_w in the higher order approximation to the Navier-Stokes equation for the flow past the original body. Here Re is a characteristic Reynolds number based on free stream velocity and body dimensions, s and n are streamline and normal coordinates scaled relative to a characteristic boundary layer thickness δ_o, R_w and R^* are the local radii of curvature of the wall and displacement body and the asterisk denotes conditions at the displacement surface. The first term in equation (1) is a centrifugal correction due to the increase in streamline curvature as one proceeds away from the wall while the second term arises from the streamwise change in curvature of the wall itself. Since s is scaled relative to δ_o (see Chapter II for a further discussion of this point), the second term in equation (1) will, in general, be small compared to the first unless R_w changes to lowest order on a length scale of $O(\delta_o)$. For a

sphere this term is identically zero. Thus, for smoothly contoured bodies without sharp corners equation (1) reduces to

$$\frac{dp}{ds_w} = \frac{\partial p}{\partial s^*_{wn}} \left(\frac{R_w}{R^*}\right) = \frac{dp}{ds^*} \tag{2}$$

where in the second equality we have used the approximation that $ds^* = (R^*/R_w)\, ds_{wn}$.

Equation (2) states that if Prandtl boundary layer equations are used to generate a displacement body in which viscous layer centrifugal effects are included then except for a constant of integration the pressure as a function of distance along the surface of the original body should be equal to the pressure as a function of distance along the displacement body. The pressure transformation from the displacement body back to the surface of the original is thus one that preserves arc length, that is $ds_w = ds^*$. This pressure mapping is equivalent to stretching the differential distance element along the body surface by a factor R^*/R_w in the expression for the wall pressure gradient.

The principal simplifying assumptions used in the derivation of equations (1) and (2) are that the local radius of curvature of the displacement body is equal to the local radius of curvature of the original body plus the local displacement thickness and that viscous corrections to the normal pressure field are of $O(Re^{-1})$ and can, therefore, be neglected. The basic difference between the two-dimensional analysis presented in Chapter II and the axisymmetric theory described herein is the presence of transverse curvature effects in the continuity equation and the viscous terms of the streamwise momentum equation. These differences affect the normal pressure field (only to $O(Re^{-1})$ and have been omitted.

The new pressure hypothesis has been tested against a wide variety of two-dimensional numerical Navier-Stokes solutions in Chapter II. Remarkably good agreement was obtained after a single iteration for the surface pressure distribution for both semi-infinite and finite bodies (parabolas, circular and elliptic cylinders) over the entire range of Reynolds numbers where these finite difference solutions exist. Equally good agreement is obtained in the present study for the flow past paraboloids of revolution, spheres and spheroids.

The other novel feature of the new approximate theory is the successive approximation scheme used for determining the inner and outer flow solutions when both the surface pressure distribution and the effective displacement body are unknown. Due to the large distortion in effective body shape caused by the thick viscous layers and wake, one seeks an iterative solution procedure in which the initial guess for the surface pressure distribution already takes into account in an approximate manner the displacement and centrifugal effects of the viscous flow region. The first trial solution for the potential flow pressure distribution is thus based on a family of enlarged geometrically similar bodies in which the local radius is increased in accordance with the growth of the viscous displacement thickness up to the station in question and the surface pressure gradient modified to satisfy the new pressure hypothesis equation (2). The solution for the outer flow for second and higher order iterations is complicated by the fact that it requires a potential flow solution for the flow past an arbitrary symmetric boundary shape. Accurate but approximate solution techniques based on the boundary method have been developed in Chapter II for two-dimensional potential flow. These techniques which differ for

finite and semi-infinite bodies are extended in the present study to axisymmetric potential flows.

This extended introduction has been given to provide a continuity between the present investigation and the earlier two-dimensional study. Much of the theoretical development for axisymmetric flow parallels that already presented in Chapter II. Only the important differences in this development will be presented in detail herein. The reader is referred to this earlier work for a more complete description of the basic solution procedure and discussion of the fundamental simplifying assumptions.

Section 2 states the boundary value problems for the viscous and inviscid flow regions. The general solution procedure is briefly summarized in Section 3. Sections 4, 5 and 6 describe the application of the new displacement interaction model to paraboloids of revolution, spheres and prolate spheroids, and present detailed numerical comparisons with existing exact Navier-Stokes solutions for the flow past these bodies.

2. The Boundary Value Problem for Axisymmetric Flow

Two important differences between the present analysis and the previous two-dimensional theory are the governing equations for continuity and streamwise momentum in the thick viscous layers surrounding the body. The continuity equation is the same as in conventional axisymmetric boundary layer theory but the steamwise momentum equation contains corrections of $O(\delta_o)$ first derived by Millikan (1932) which arise from transverse curvature effects in the divergence of the stress tensor. The equations in question are:

$$u \frac{\partial u}{\partial x} + v \frac{\partial u}{\partial y} = - \frac{1}{\rho} \frac{dp}{dx} + \nu\left(\frac{\partial^2 u}{\partial y^2} + \frac{1}{R} \frac{\partial R}{\partial y} \frac{\partial u}{\partial y}\right) \tag{3}$$

$$\frac{\partial(uR)}{\partial x} + \frac{\partial(vR)}{\partial y} = 0 \tag{4}$$

Here R is related to the normal boundary coordinate y (see Figure 1) by

$$R = R_o + y\cos\varepsilon \tag{5}$$

and the wall pressure gradient dp/dx is related to the pressure gradient along the displacement body dp/dx* using the new pressure hypothesis equation (2)

$$\frac{dp}{dx} = \frac{dp}{dx^*} \tag{6a}$$

with

$$x = x^* \ ; \tag{6b}$$

where x* is the distance s* measured from the forward stagnation point

of the displacement body. At high Reynolds numbers the new term $\frac{\nu}{R}\frac{\partial R}{\partial y}\frac{\partial u}{\partial y}$ is negligible. This is not, however, true at the intermediate Reynolds numbers characteristic of the present study. Some indication of the importance of this term can be gleaned from Sections 3(a) and 6. It is interesting to note that for a two-dimensional flow $R \to \infty$ and equation (3) reduces to the classical two-dimensional equation given by Prandtl, whereas for $\varepsilon = \pi/2$ equations (3) and (4) reduce to the governing equations for an axisymmetric stagnation point flow. From equation (6) the pressure as a function of distance along the original and displacement bodies is equal except for an additive constant due to viscous losses in total pressure along the streamline passing through the forward stagnation point. Since $r^* > r_w$ the local polar coordinate θ is stretched such that $\theta > \theta^*$ as shown in Figure 1.

The effective displacement body is constructed by adding the displacement thickness distribution

$$\delta^*(x) = \frac{1}{U(x)} \int_0^{\delta(x)} (U(x) - u)dy \qquad (7)$$

obtained from the solution of equation (3) for the velocity profile to the original body surface. This construction differs from the conventional method of constructing the displacement body in that the inviscid pressure gradient at position x^* (angular location θ^*) on the displacement surface is used to calculate the displacement thickness δ^* at position x (angular location θ) on the original body in accord with the pressure mapping described by equation (6).

The inviscid pressure distribution and the velocity $U(\theta^*)$ at the surface of the displacement body is determined from the solution of the

generalized axisymmetric potential flow equation

$$D^2\Psi = 0 \tag{8}$$

where Ψ is the inviscid streamfunction. This equation satisfies the usual inviscid boundary condition that the normal component of the velocity vanish at the displacement surface

$$v(x^*) = 0 \text{ on } r = r^* \tag{9}$$

Since the solution for $\delta^*(x)$ depends on the solution for $p(x)$ and both are unknown, the solution of equations (3) through (9) represents a coupled non-linear boundary value problem. In essence, we wish to solve equation (8), subject to a known boundary condition (9) along an unknown surface, the effective displacement body. This body is determined from the solution of equations (3) and (4) in which the surface pressure distribution satisfies the pressure hypothesis (6) and must be obtained through a process of iterative approximation.

3. Solution Procedure

The solution procedure developed for solving the boundary value problem presented in Section 2 is basically the same as that described in detail in Chapter II for the two-dimensional case. We shall only summarize the method for generating the first trial solution for the displacement body and the iteration procedure for obtaining a converged solution below and refer the reader to Chapter II for the motivation and rationale behind the development of the solution techniques.

A. First trial solution for the displacement body:

1. Both the displacement thickness and the pressure gradient at the forward stagnation point are unknown. To approximate the displacement body a family of geometrically similar bodies with the same focal point as the original body is selected. The pressure or velocity gradient at the forward stagnation point on the displacement body is written in terms of the unknown displacement thickness and applied at the surface of the original body using the pressure stretching hypothesis equation (6). This expression is then simultaneously solved with equation (3) applied at the forward stagnation point. The solution technique is illustrated in subsection 3(a) for the case of a sphere.

2. Having obtained this first trial solution for δ^*, dp/dx and the velocity profile at the forward stagnation point, one performs a forward numerical integration of equation (3). For present purposes it was deemed satisfactory to use a momentum integral approximation to equation (3) rather than the more accurate finite difference solutions in view of the other approximations introduced. At each forward integration step the pressure gradient is represented by the local pressure

gradient for the inviscid flow past the geometrically similar body whose local radius from the focal point of the original body is equal to that of the displacement body. From equation (6) this pressure gradient is also equal to the pressure gradient along the original body surface.

3. The displacement thickness distribution obtained from the solution described in step 2. is now added on normally to the surface of the original body. Because of the pressure mapping (6b) the pressure gradient at position x^* on the displacement body is used to calculate the displacement thickness at position $x = x^*$ on the original body as shown in Figure 1. This completes the first trial solution for the effective displacement body.

B. The iteration procedure for a converged solution:

1. As we shall observe in the results, the first trial solution just outlined provides a reasonable approximation for the displacement surface since it qualitatively includes the streamwise coordinate straining required to describe curvature effects, but a poor detailed description of the surface pressure distribution since the actual shape of the displacement body and its wake can depart significantly from the family of geometrically similar bodies used in the first trial solution. The first step towards obtaining a converged solution is thus to obtain a much more accurate representation of the potential flow pressure distribution on the displacement body. This task is equivalent to solving equations (8) and (9) for an arbitrary boundary shape, since the displacement body obtained from A. above will not in general have a simple analytic representation. An approximate combined numerical and analytical solution technique based on the boundary method has been developed for this purpose and is described in subsection 3(b).

2. The potential flow pressure distribution on the first order displacement body obtained in 1. above is now mapped back to the surface of the original body using equation (6b). The momentum integral equation formulation of equation (3) is now solved again using this new pressure distribution.

3. The new solution for the displacement thickness distribution found in 2. is now added on normally to the surface of the original body, in the same manner as before, to obtain the second order approximation for the displacement body.

4. Steps 1, 2 and 3 are now repeated to obtain the third and higher order approximations to the displacement body until convergence in either body shape or surface pressure distribution is achieved to within predetermined limits.

In accord with the preceeding solution outline the approximate equation for the viscous layer is the momentum integral equation obtained from equations (3) and (4). This equation can either be derived by a direct integration of equations (3) and (4), Millikan (1932) or using a control volume approach, Gluckman (1971). The desired equation is:

$$\frac{d\theta}{dx} = \frac{(\Lambda\nu U'_e)^{1/2}}{U_e}\left(\frac{2}{\Lambda} + \frac{1}{6} - \frac{2\theta}{\delta} - \frac{\delta^*}{\delta} - \frac{R'}{R}\right.$$

$$\left. \frac{U_e}{U'_e}\frac{\theta}{\delta} - \frac{\gamma F_1}{R\,U_e(\Lambda\nu U'_e)^{1/2}} - \frac{\gamma F_2}{R\,U_e(\Lambda\nu\, U'_e)^{1/2}}\right) \tag{10}$$

where

$$\delta^* = \frac{1}{U_e}\int_o^\delta (U_e - u)\,dy \qquad \text{displacement thickness} \tag{11a}$$

$$\theta = \frac{1}{U_e^2} \int_o^\delta u(U_e - u)dy \qquad \text{momentum thickness} \qquad (11b)$$

$$\Lambda = \frac{\delta^2}{\nu} \frac{dU_e}{dx} \qquad \text{velocity profile shape factor} \qquad (12a)$$

$$\gamma = (1 - (\frac{dR}{dx})^2)^{1/2} \qquad (12b)$$

$$F_1 = \frac{d}{dx}[(A_2 - A_1)U_e^2\delta^2] + (1/2 - A_2)U_e U_e' \delta^2 \qquad (12c)$$

$$F_2 = (A_2 - A_1)U_e^2\delta^2 \qquad (12d)$$

$$A_1 = \frac{e^2}{4} + \frac{2ef}{5} + \frac{(f^2+2eg)}{6} + \frac{2(eh+fg)}{7} + \frac{(g^2+2gh)}{8} + \frac{2gh}{9} + \frac{h^2}{10} \qquad (12e)$$

$$A_2 = \frac{e}{3} + \frac{f}{4} + \frac{g}{5} + \frac{h}{6} \qquad (12f)$$

Equation (10) would be identical to the classical high Re number axisymmetric boundary layer equations were it not for the last two terms in the bracket on the right side. These two terms represent transverse curvature effects of $O(\delta_o)$. The coefficients e, f, g, and h in equation (12) are derived from the Pohlhausen quartic profile

$$\frac{U}{U_e} = e(\frac{Y}{\delta}) + f(\frac{Y}{\delta})^2 + g(\frac{Y}{\delta})^3 + h(\frac{Y}{\delta})^4 \qquad (13)$$

with

$$e = 2 + \frac{\Lambda}{6} \qquad (13a)$$

$$f = -\frac{\Lambda}{2} \qquad (13b)$$

$$g = -2 + \frac{\Lambda}{2} \tag{13c}$$

$$h = 1 - \frac{\Lambda}{6} \tag{13d}$$

This profile provides a reasonable description up to separation and a solution of undetermined accuracy beyond the separation point. One notes, however, that the smoothly varying polynomial profile is much more likely to provide at least a qualitatively passable description of the separated flow at the intermediate Reynolds numbers considered herein where steep vorticity gradients are not present than at high Re where there is a thin boundary layer-like structure both in the reversed flow near the wall and in the separated free shear layers.

The ratios θ/δ and δ^*/δ are given below for completeness

$$\frac{\theta}{\delta} = \frac{1}{63}\left(\frac{37}{5} - \frac{\Lambda}{15} - \frac{\Lambda^2}{144}\right) \tag{14a}$$

$$\frac{\delta^*}{\delta} = \frac{3}{10} - \frac{\Lambda}{120} \tag{14b}$$

3(a). First Trial Solution for the Forward Stagnation Point

To elucidate the solution procedure described under step 1. of the first trial solution for the displacement body, we consider the stagnation point flow on a sphere of unit radius. The geometrically similar displacement bodies considered are concentric spheres of radius $r^* = 1 + \delta^*$. Both δ^* and dU/dx at the forward stagnation point are unknown. The potential flow solution for the velocity on the surface of a geometrically similar displacement sphere of radius r^* is

$$U_e = \frac{3}{2} U_\infty \sin\theta^* \tag{15}$$

where θ and θ^* are related by $r\theta = r^*\theta^*$ from equation (6b). The velocity gradient at the forward stagnation point on the original body surface obtained from equation (15) and the pressure transformation (6) is

$$\frac{dU_e}{dx} = \frac{\frac{3}{2} U_\infty}{1+\delta^*} \cos\theta^* \tag{16}$$

Both δ^* and U_e' are unknown at the forward stagnation point. The solution of equation (10) at the forward stagnation point requires that the following term be set equal to zero.

$$\frac{2}{\Lambda} + \frac{1}{6} - \frac{2\theta}{\delta} - \frac{\delta^*}{\delta} - \frac{R'}{R} \quad \frac{U_e}{U_e'} \frac{\theta}{\delta} - \tag{17}$$

$$\frac{\gamma F_1 + \gamma' F_2}{R\, U_e\, U_e'\, \delta} = 0$$

Inserting the definitions (12) and (13) into (17) one obtains an expression for the velocity profile shape factor Λ at the forward

stagnation point

$$\Lambda_{fsp} = \frac{2}{(2 + \frac{1}{R})\frac{\theta}{\delta} + \frac{\delta^*}{\delta} + \frac{\delta}{R}(2A_2 - 3A_1 + \frac{1}{2}) - \frac{1}{6}} \qquad (18a)$$

Equation (18a) is an interesting new result because it shows that the effect of the transverse curvature in equation (10) is to make the shape factor and hence the velocity profile at the forward stagnation point a function of Reynolds number in contrast to the two-dimensional stagnation point solution considered in Chapter II. Table I below shows the results of Λ_{fsp} versus Reynolds number for a sphere.

TABLE I

Λ_{fsp} vs Reynolds Number for a Sphere

Reynolds Number	fsp
∞	4.7160
130	4.318933
100	4.271017
60	4.163813
40	4.064817
15	3.772865
10	3.631787
8	3.54948
5	3.36939

As can be seen, from Table I, the results for larger Reynolds numbers asymptotically approach the high Reynolds number, boundary layer result where Λ_{fsp} is a constant value 4.716.

The displacement thickness at the forward stagnation point can be calculated from equation (18b).

$$\delta^*(0) = \frac{G}{2Re} + \sqrt{\frac{G^2}{4Re^2} + \frac{G}{Re}} \tag{18b}$$

where

$$G = \frac{2\Lambda_{fsp}}{1.5}\left(\frac{3}{10} - \frac{\Lambda_{fsp}}{120}\right)^2 \tag{18c}$$

$\delta^*(0)$ thus depends on Reynolds number and body geometry.

3(b). Inviscid Flow Past the Displacement Body

The crucial step in the iterative approximation procedure used to obtain a converged solution is the development of a simple yet accurate approximate technique for determining the flow past smoothly contoured non-analytic boundary shapes. In Chapter II an approximate technique was developed for two-dimensional potential flows in which the displacement body including the wake was represented by an internal distribution of line sources and sinks whose strength and location were determined using a boundary method approach in which inviscid flow boundary conditions are satisfied at discrete points on the body. The detailed application of the boundary method developed differed depending on whether the body was of low or high (this included semi-infinite bodies) aspect ratio. Following this earlier development one now starts with an unknown finite distribution of N point sources and sinks of strength m_i located at positions x_i along the axis of symmetry of the body and placed in a uniform stream. The stream function for this flow is:

$$\psi = -U_\infty R^2 + \sum_{i=1}^{N} m_i \left(\frac{(x-x_i)}{((x-x_i)^2 + R^2)^{1/2}} - 1 \right) \qquad (19)$$

where x, R here represent cylindrical polar coordinates. For the flow past low and moderate aspect ratio finite bodies, such as a sphere one finds that a surprisingly good representation of the desired $\psi = 0$ boundary shape can be obtained using only four equally spaced boundary points between flow attachment and separation if both m_i and x_i were left unspecified and the series in equation (19) is truncated at $N = 2$, see Figures 4 and 5.

For the flow past semi-infinite bodies, such as the family of paraboloids of revolution considered herein or high aspect ratio finite

bodies, many more boundary points are required for an accurate curve fit in which the $\psi = 0$ streamline does not exhibit wave-like undulations. The solution of the matrix of equations derived from (19) when many boundary points are required is extremely tedious if both m_i and x_i are treated as unknowns since the x_i appear non-linearly. A much simpler procedure for these extended bodies is to specify the source-sink locations x_i and leave only the values of m_i to be determined since these constants appear linearly in equation (19). A convenient but arbitrary selection of boundary points and source locations in this procedure is to position the singularities directly below the boundary points in one to one correspondence. Employing standard matrix reduction schemes for systems of linear equations, one can easily handle as many as 100 boundary points using less than a minute of computer time.

4. Paraboloids of Revolution

As the first application of the new approximate theory described in Sections 2 and 3, we consider the uniform viscous flow past axisymmetric paraboloids of revolution whose surface is defined by

$$R^2 = 4(1+x) \tag{20}$$

at various Reynolds numbers. This simple body shape, for which separation does not occur, provides a convenient axisymmetric geometry to test the basic hypothesis of the new model with existing finite difference solutions of the Navier-Stokes equations, Davis and Werle (1972), and conventional boundary layer theory.

The family of geometrically similar axisymmetric paraboloids used to generate the surface pressure distribution in equation (10) for the construction of the first trial guess for the displacement body is given by

$$R^2 = 4c^2(x+c^2) \tag{21}$$

For $c = 1$ this reduces to equation (20) whereas for $c > 1$ one obtains a family of geometrically enlarged paraboloids with a common focal point at the origin.

The speed along the surface of the paraboloid defined by equation (21) is:

$$q = U = U_\infty \cos\left(\frac{\pi-\theta^*}{2}\right) \tag{22}$$

The potential flow solution (22) replaces equation (15) in the first trial solution for the forward stagnation point flow and is also used to approximate the local pressure gradient in equation (10) as described

in step 2 of the procedure for determining the first trial solution for the displacement body. In applying the pressure mapping described by equation (6) we have related the polar angles θ and θ^* measured from the forward stagnation point along the original and effective displacement body surfaces by the arc length formula

$$\int_o^{\theta^*} \sqrt{r^{*2} + \left(\frac{dr^*}{d\theta}\right)^2}\, d\theta = \int_o^{\theta^*} \sqrt{r^2 + \left(\frac{dr}{d\theta}\right)^2}\, d\theta \qquad (23)$$

In the discussion beneath equation (6) it was mentioned that the pressure distribution as a function of distance along the original and displacement surfaces are equal to within an additive constant due to the viscous loss in total pressure along the stagnation streamline. In Chapter II an expression for the increase in wall pressure coefficient due to viscous losses is developed. This result which is also valid for axisymmetric flow is

$$C_{pw} = \frac{p_w - p_\infty}{\rho U_\infty^2} = \frac{1}{2}\left(1 + \frac{4}{Re}\frac{\partial V_e}{\partial y}\right) \qquad (24)$$

where $\partial V_e/\partial y$ is the velocity gradient normal to the displacement thickness and the Reynolds number is based on the radius of curvature R_o at the forward stagnation point. For the paraboloid this is equal to twice the focal radius.

In Figures 2 and 3 we have compared the results of the present approximate model with the numerical Navier-Stokes solutions of Davis and Werle (1972) for the surface pressure distribution of a paraboloid at a Reynolds number of 10 and 100. The importance of the viscous pressure losses predicted by equation (24) and the streamwise stretching of

the body surface coordinate required by the pressure hypothesis (6) are particularly evident for the Re = 10 flow. The potential flow pressure distribution for the inviscid flow past the original body considerably lags the Navier-Stokes solution for the surface pressure over the entire body. The inclusion of viscous layer displacement effects using conventional axisymmetric boundary layer theory to construct the displacement body and no stretching produces only a very slight improvement in this retarded pressure development (not shown) while the inclusion of the viscous pressure losses from equation (24) serves only to elevate the surface pressure distribution in the forward stagnation point region. A very substantial improvement in the agreement with the exact Navier-Stokes solutions is achieved, however, for the first order approximation to the displacement body using the new pressure stretching hypothesis and the viscous correction for the pressure loss across the layer. The first order approximation is obtained by curve fitting the zeroth order displacement body using equation (19) and then mapping the pressure back to the body surface using equation (6). A typical curve fit employing 12 boundary points is able to generate a $\psi = 0$ boundary streamline which is nearly indistinguishable from the desired shape. Also shown in these figures for comparison is the pressure distribution obtained using second order boundary layer theory, a conventional construction of the displacement body and no coordinate straining.

5. Spheres

A much more rigorous test of the new approximate theory is the flow past a sphere in the Reynolds humber range 5 to approximately 130 where a closed steady wake separation bubble is observed in both experiments and numerical Navier-Stokes solutions.

The solution scheme for spheres has already been described in detail in Section 3. Equation (10) when integrated using the surface velocity distribution (15) yields the first trial solution for the displacement body. This body is illustrated in Figures 4 and 5 for a Re of 10 and 40. Also shown in these figures is the approximate solution for the inviscid flow past this displacement body obtained using equation (19) with N=2, as discussed in Section 3(b). The four match points used are denoted by asterisks. The last asterisk denotes the point of separation. The surprisingly good approximation that can be obtained for the displacement body using only two source-sink singularities is clearly evident in these figures.

Figures 6 and 7 show the displacement bodies obtained by the successive iteration procedure described in 3(b). The significant deviation between the first and higher order approximations arises because the second and higher order approximations predict separation at a smaller angle $\emptyset$ from the rear stagnation point. This is shown in Figure 8 where we have compared the theoretically predicted location of separation as a function of Reynolds number with available Navier-Stokes solutions. The difference between second and higher order approximate solutions is in general very small as observed in Figures 6 and 7.

The crucial test of the new theory is whether it can accurately predict the surface pressure distribution on the sphere. Figures 9-11

illustrate the excellent comparison with available Navier-Stokes solutions obtained using the new pressure hypothesis equation (6). The pressure predicted by the new theory begins to deviate from the numerical Navier-Stokes solutions in the region just prior to separation. This could either be due to the assumptions involved in the derivation of the pressure hypothesis or the failure of the quartic profile to adequately describe the flow in this region.

Also shown in these figures is the surface pressure predicted by second order boundary layer theory equation (10) and conventional construction of the displacement body. It was pointed out earlier that equation (10) in that it contains viscous corrections of $O(\delta_o)$ is equivalent to the streamwise momentum equation used in second order axisymmetric boundary layer theory.

In Table II we have shown the separation angle (as measured from the forward stagnation point) vs. Reynolds number obtained by solving the conventional boundary layer equations, equation (10) without coordinate straining and equation (10) using the new pressure hypothesis. As is easily seen from the table, the inclusion of the additional viscous term has provided a small improvement over the first order axisymmetric boundary layer theory using the conventional construction of the displacement body. At a Reynolds number of 100 (Figure 11) the additional curvature term in equation (10) has provided a significant improvement in the predicted surface pressure without coordinate straining but a relatively poor prediction of the separation point location. At a Reynolds number of 10 (Figure 9) the importance of the new pressure hypothesis is especially evident.

TABLE II

SEPARATION ANGLE vs. REYNOLDS NUMBER

Reynolds Number	Prandtl Boundary Layer Eqns. Conventional Construction Displacement body	Second Order Boundary Layer theory	Present Theory Second Order Approximation	EXACT (Rimon and Cheng 1969)
10	115.9	121.7	163.0	167.5
20	113.4	118.4	150.0	
40	111.6	115.6	139.5	144
60	110.9	114.2	135.0	
100	109.98	112.9	130.0	127.5
130	109.61	112.2	127.5	
∞	109.6	109.6		

In the present study we have been primarily concerned with determining the surface pressure up to the point of separation, since the fourth order polynomial description given by equation (13) is a poor detailed representation of the flow in the separated flow region. The pressure at the rear stagnation point on the sphere could, therefore, not be used as the zero reference value as is commonly done in the numerical Navier-Stokes solutions. Instead we have chosen the pressure at the forward stagnation point as predicted by numerical Navier-Stokes solutions as the reference pressure for all sphere calculations.

The dramatic improvement over second order boundary layer theory in the prediction of the surface pressure distribution noted in Figures 9-11 using the new pressure hypothesis can be attributed to the greatly improved representation of the first order displacement body that results from the present solution procedure. In the conventional axisymmetric boundary layer theory, where the first order

solution for the displacement body is based on the potential flow past the original body surface, separation occurs at approximately 109.6 degrees from the forward stagnation point independent of Reynolds number. In contrast, the stretching of the body coordinate implicit in the new pressure hypothesis leads in the first trial solution to a reasonable prediction of the separation point location as observed in Figure 8. The importance of the new pressure hypothesis is clearly demonstrated in Figure 12 where we have compared the angular location of the minimum surface pressure predicted by second order boundary layer theory and the present approximate theory with available Navier-Stokes numerical solutions.

In Figure 13 we have shown a typical surface vorticity distribution for the flow past a sphere at Re = 40. The agreement with exact Navier-Stokes solutions is excellent. Figures 14 and 15 show the velocity profile development in the viscous layer and the growth of the boundary layer outer edge up to separation at Reynolds numbers of 10 and 40 respectively. No difficulty is encountered in integrating the momentum integral equation (10) through separation using the interaction pressure field. Thus, if a more accurate family of separated flow profiles is constructed one should, in theory, be able to obtain reasonable solutions for the wake separation bubble. This possibility is currently being studied.

6. Additional Results and Comments

The new theory has also been applied to a more general class of three-dimensional axisymmetric bodies, prolate spheroids, of which the sphere is the limiting case. These bodies are oriented such that their major axis is parallel to the flow. Figure 16 shows the displacement body obtained for a prolate spheroid of aspect ratio 10:9 (major/minor axis) at a Re of 100. Exact Navier-Stokes solutions of Masliyah and Epstein (1970) exist for this case. Since this body shape is almost a sphere it was anticipated that a single source/sink pair would adequately model the displacement body. This proved to be the case, as can be seen in Figure 16. Figure 17 compares the surface pressure distribution obtained using the new theory with the numerical Navier-Stokes solution of Masliyah and Epstein (1970). Figures 18 and 19 are for a prolate spheroid of aspect ratio 2:1. In this case it was necessary to use more boundary points (five) to obtain an adequate fit to the displacement body. The numerical solution of Masliyah and Epstein (1970) for the surface pressure distribution is shown in Figure 19 for comparison.

7. REFERENCES

Batchelor, G.K., 1967, "Fluid Dynamics", Cambridge University Press, 51.

Davis, R.T. and Werle, M.J., 1972, A.I.A.A. Journal 10, 1224.

Gluckman, M.J., 1971, Ph.D. Thesis, The City University of New York.

Hamielec, A.E. and Hoffman, T.W., 1967, A.I.Ch.E. Journal 13, 212.

Jenson, V.G., 1959, Proc. Royal Soc., London 249A, 346.

Lighthill, M.J., 1958, J. Fluid Mech. 4, 383.

Masliyah, J.H. and Epstein, N., 1970, J. Fluid Mech. 44, 493.

Millikan, C.B., 1932, Am. Soc. Mech. Eng. Trans. 54, 29.

Nisi, H. and Porter, A.W., 1926, Phil. Mag. 46, 754.

Rimon, Y. and Cheng, S.I., 1969, Phys. of Fluids 12, 949.

Taneda, S.J., 1956, J. Phys. Soc. Japan 11, 302.

Van Dyke, M., 1962, J. Fluid Mech. 14, 161.

Weinbaum, S., Kolansky, M.S., Pfeffer, R., and Gluckman, M.J., 1976, accepted by the Journal of Fluid Mechanics.

Werle, M.J. and Wornom, S.F., 1972, International J. Eng. Sci., 10, 875.

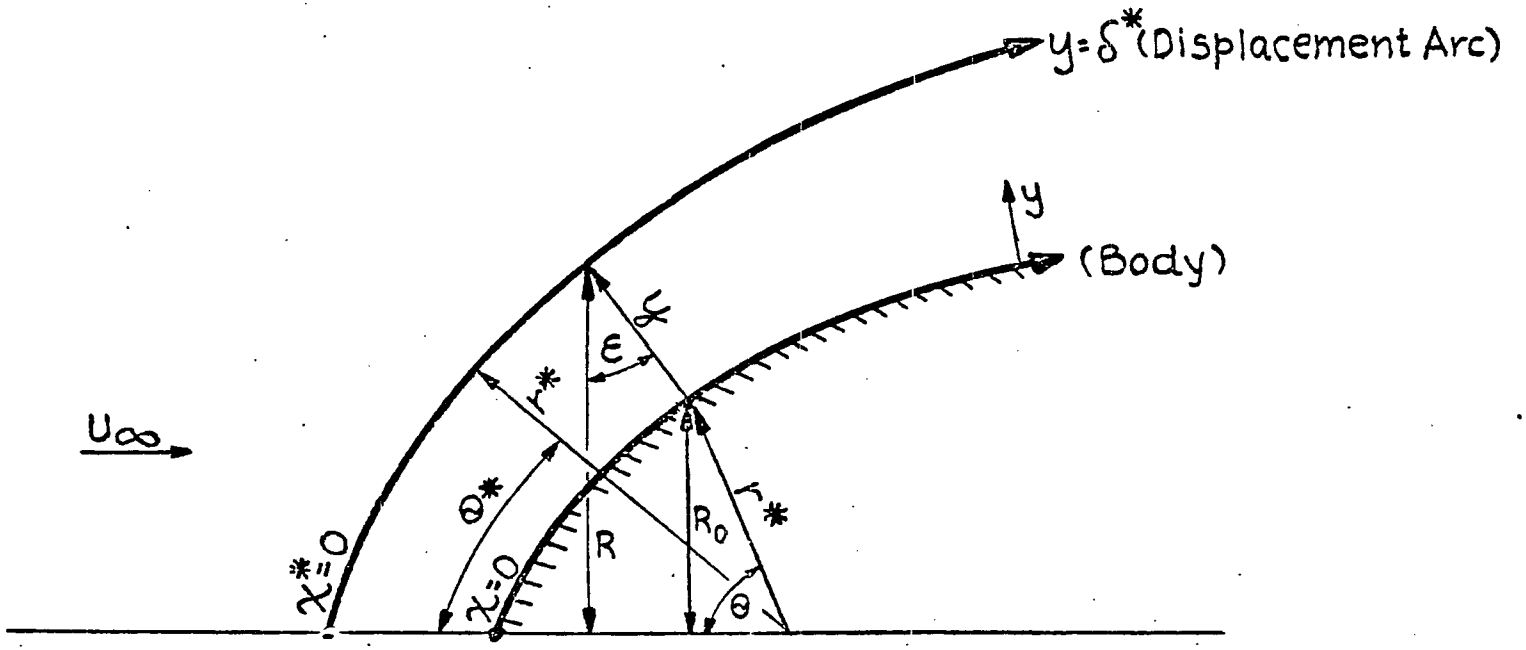

Figure 1. Boundary Layer Coordinate System.

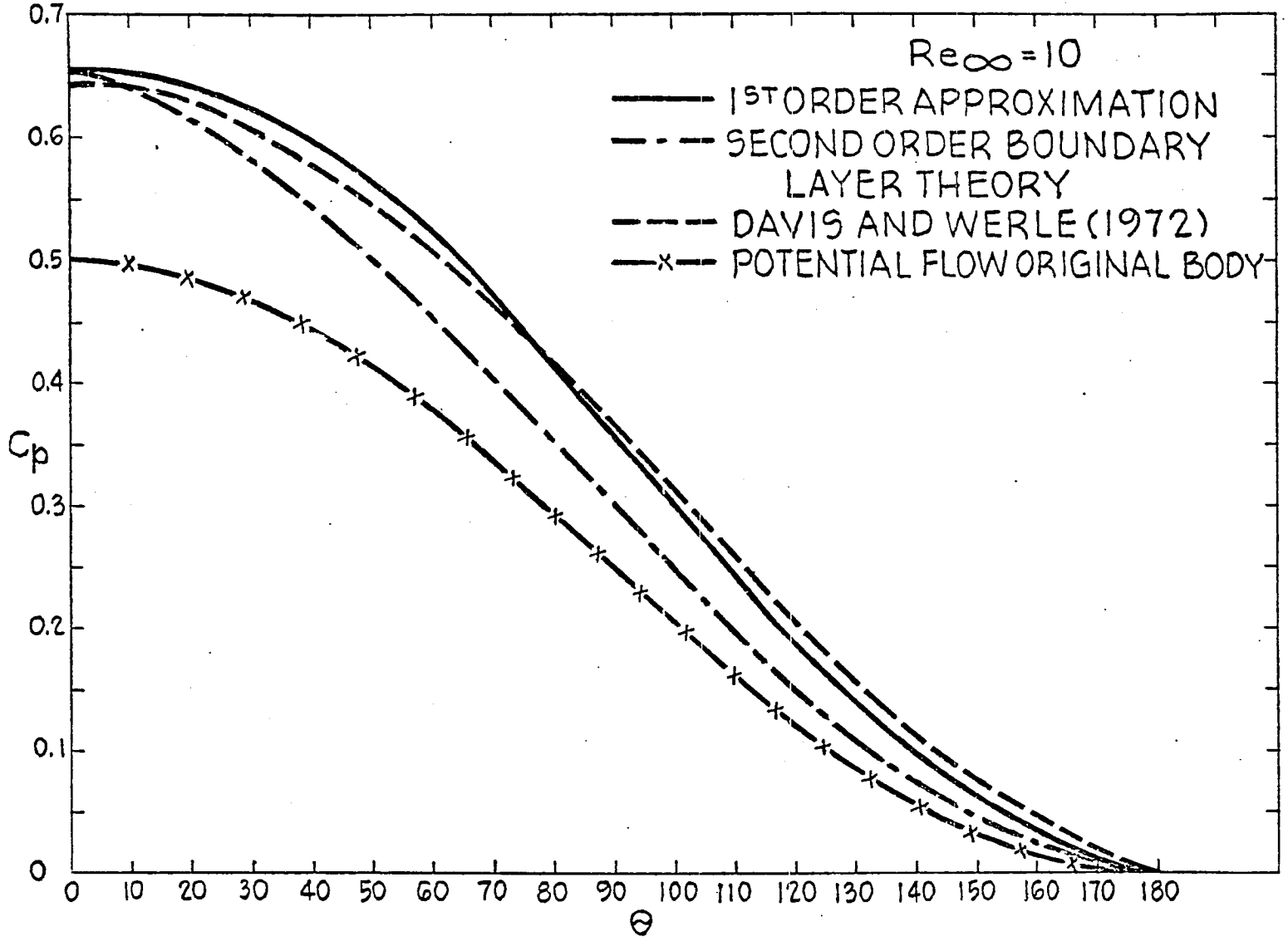

Figure 2. Surface Pressure Distribution for a Paraboloid of Revolution.

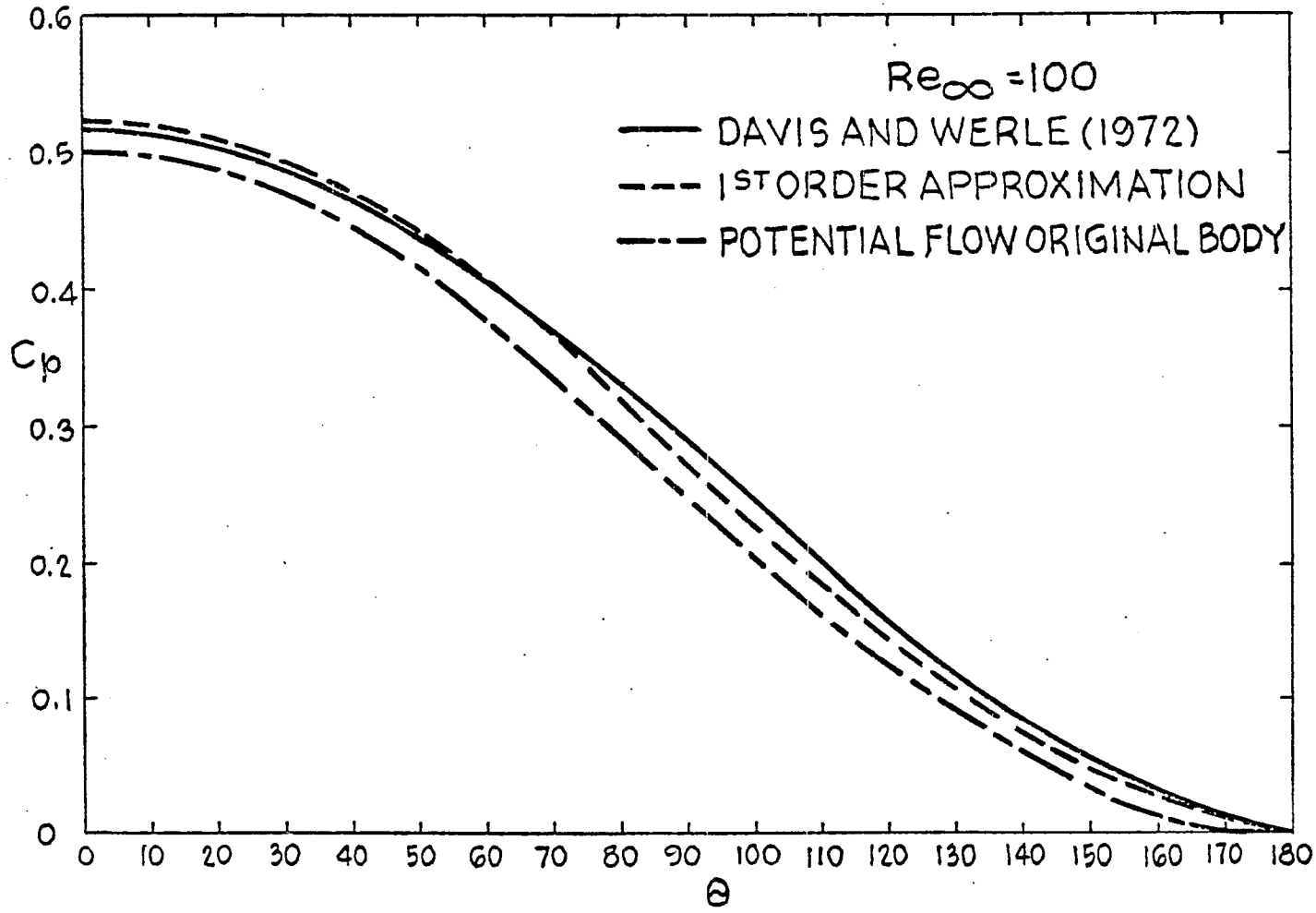

Figure 3. Surface Pressure Distribution for a Paraboloid of Revolution.

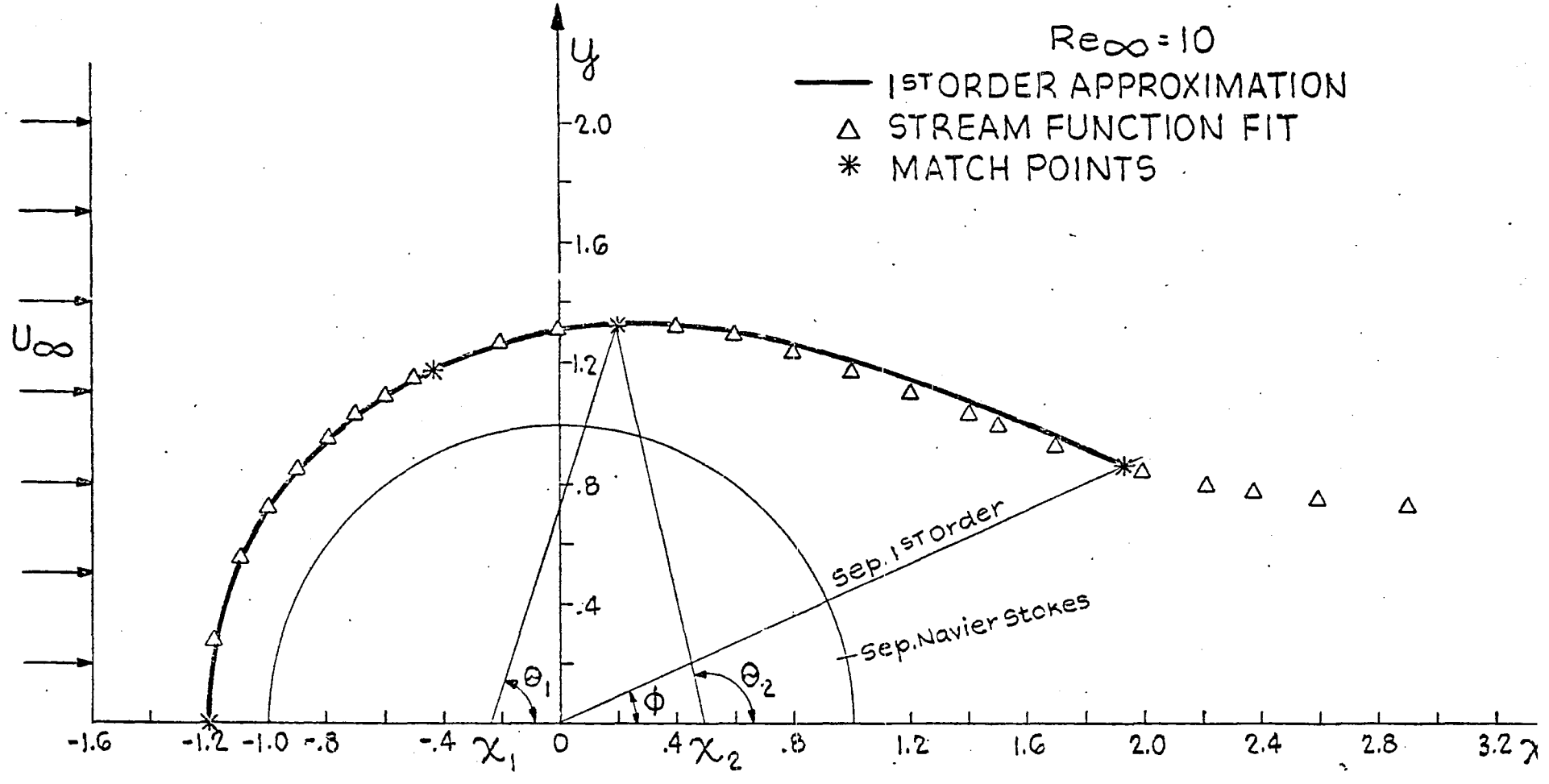

Figure 4. Stream Function Fit of the Displacement Body for a Sphere.

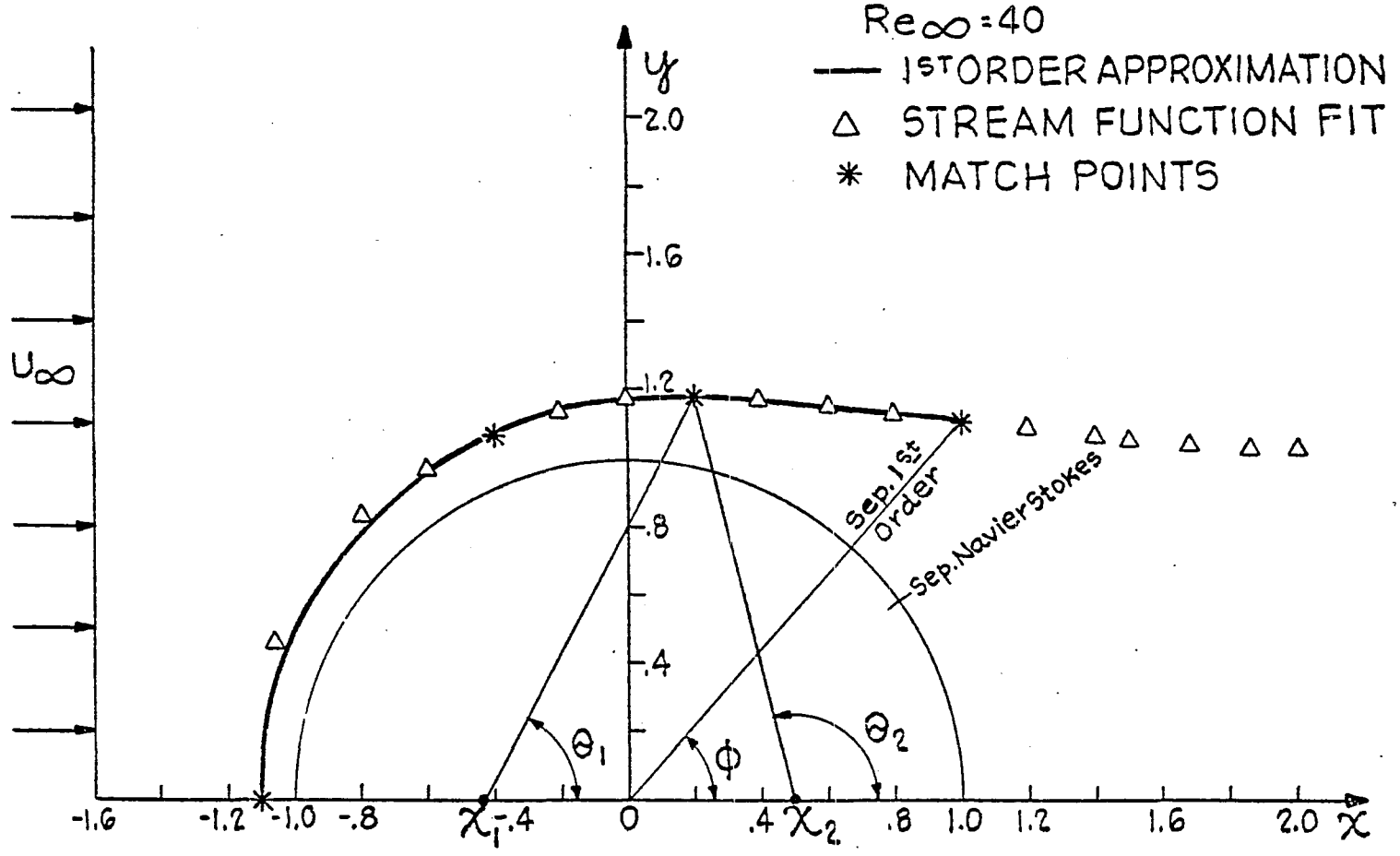

Figure 5. Stream Function Fit of the Displacement Body for a Sphere.

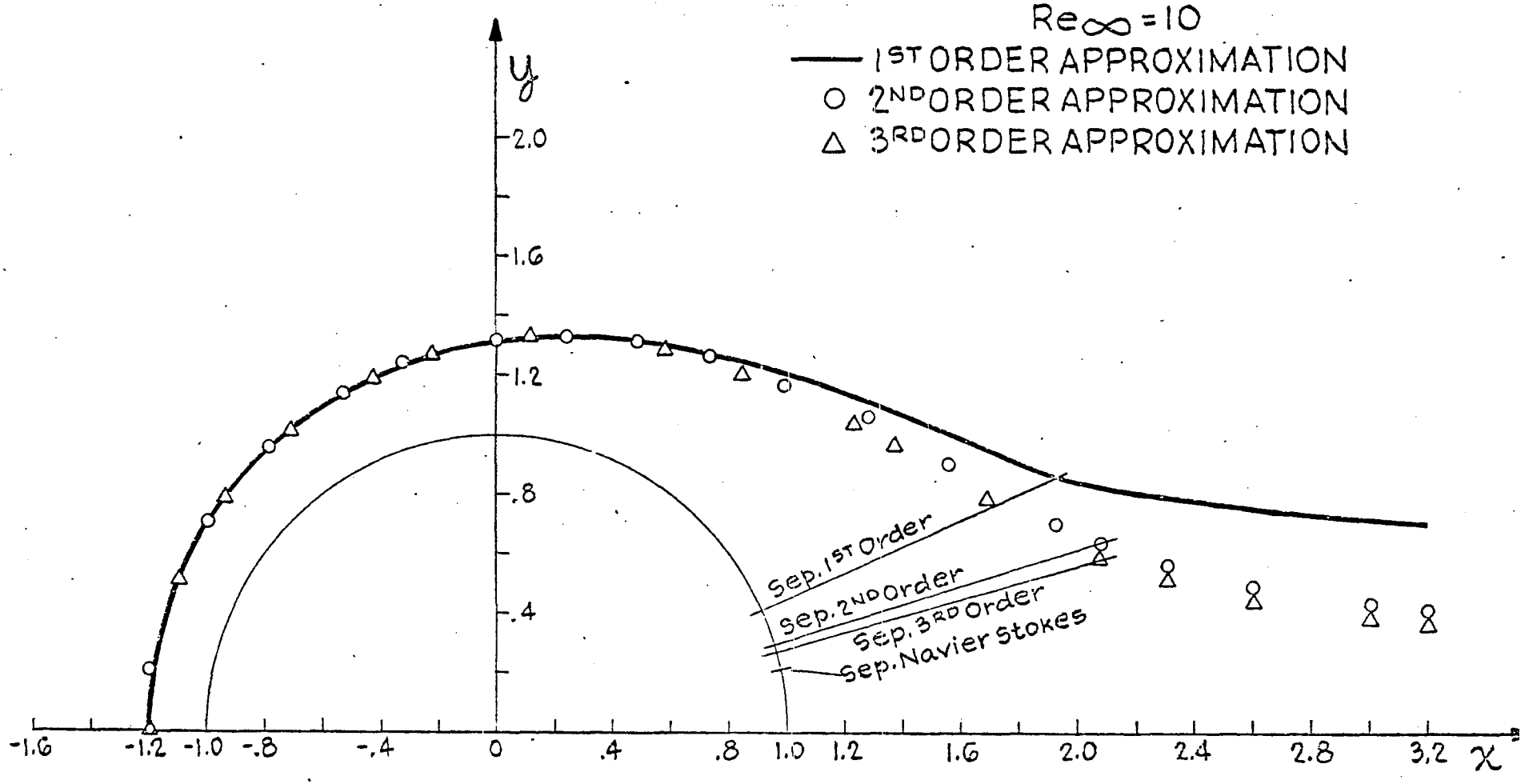

Figure 6. Successive Approximations for the Displacement Body for a Sphere.

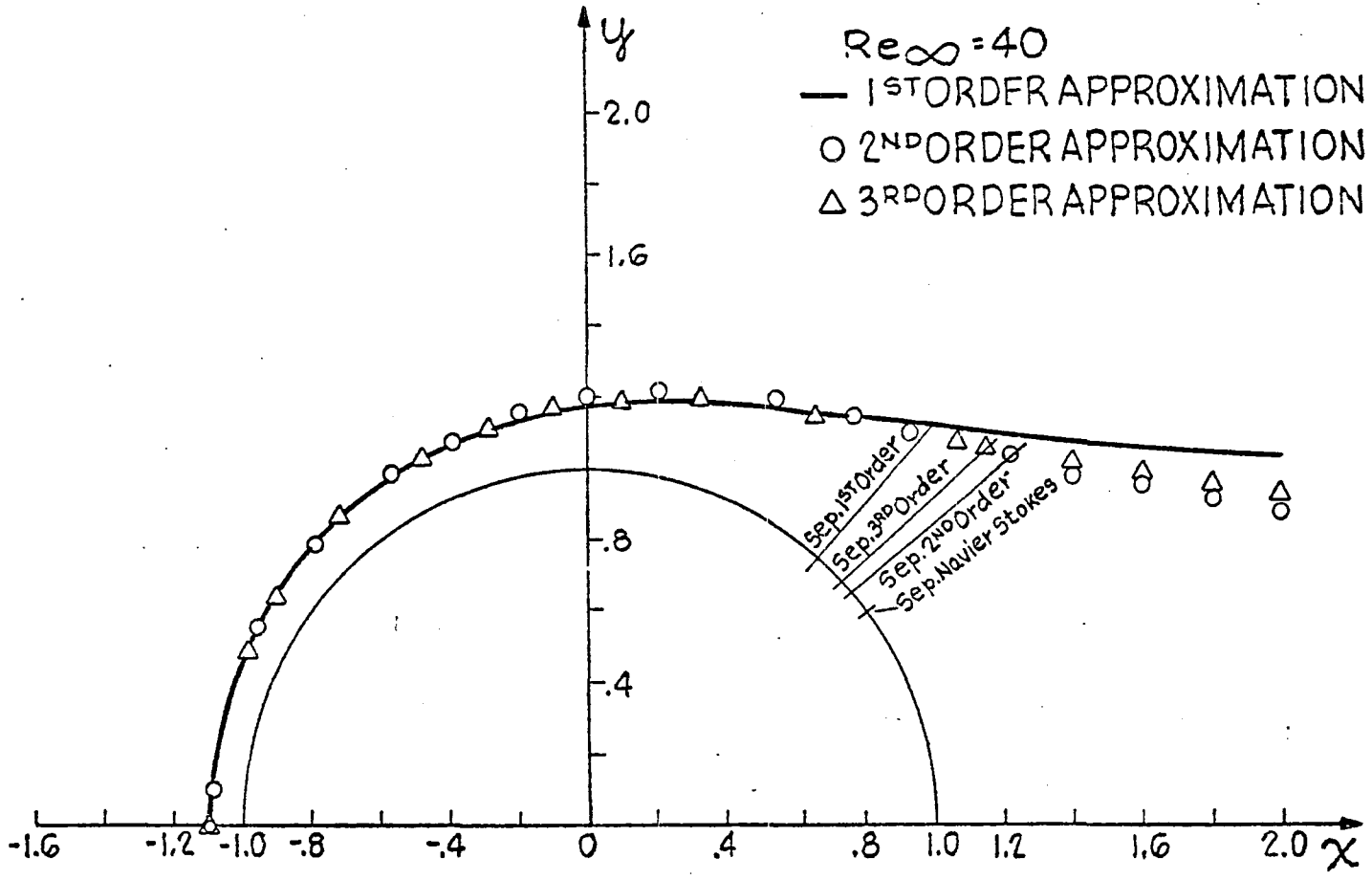

Figure 7. Successive Approximations for the Displacement Body for a Sphere.

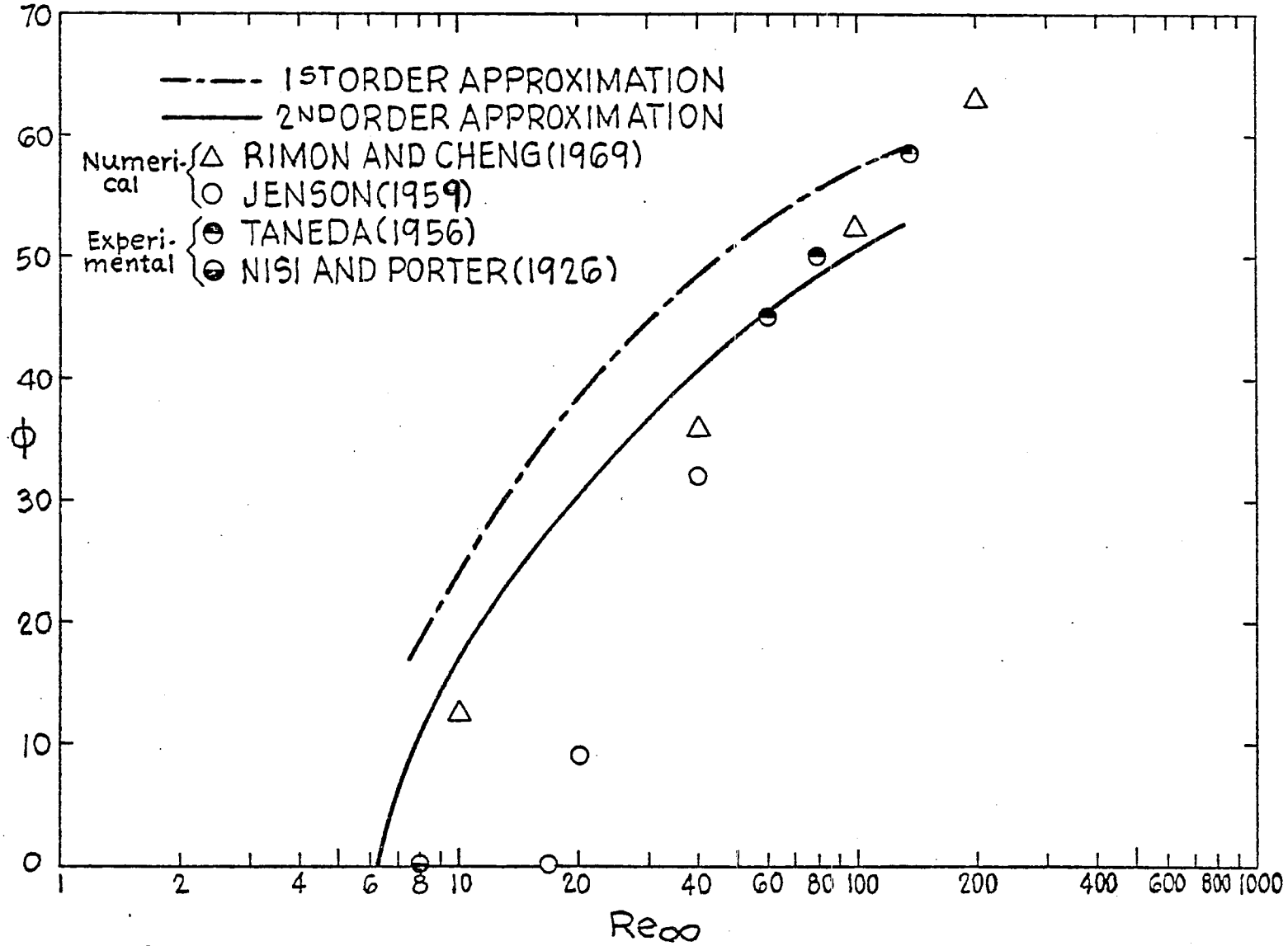

Figure 8. Separation Angle as a Function of Reynolds Number for a Sphere.

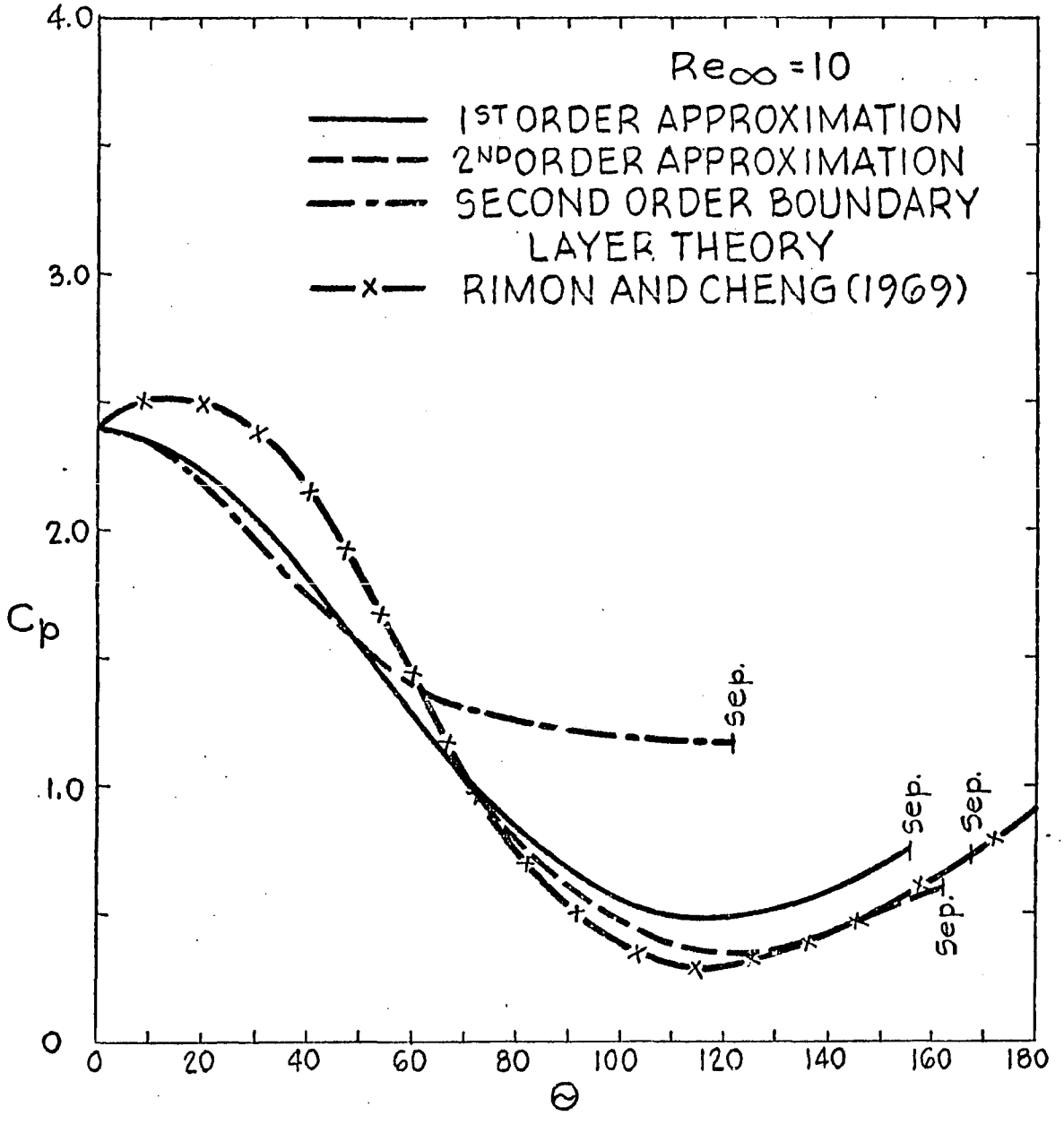

Figure 9. Surface Pressure Distribution around a Sphere.

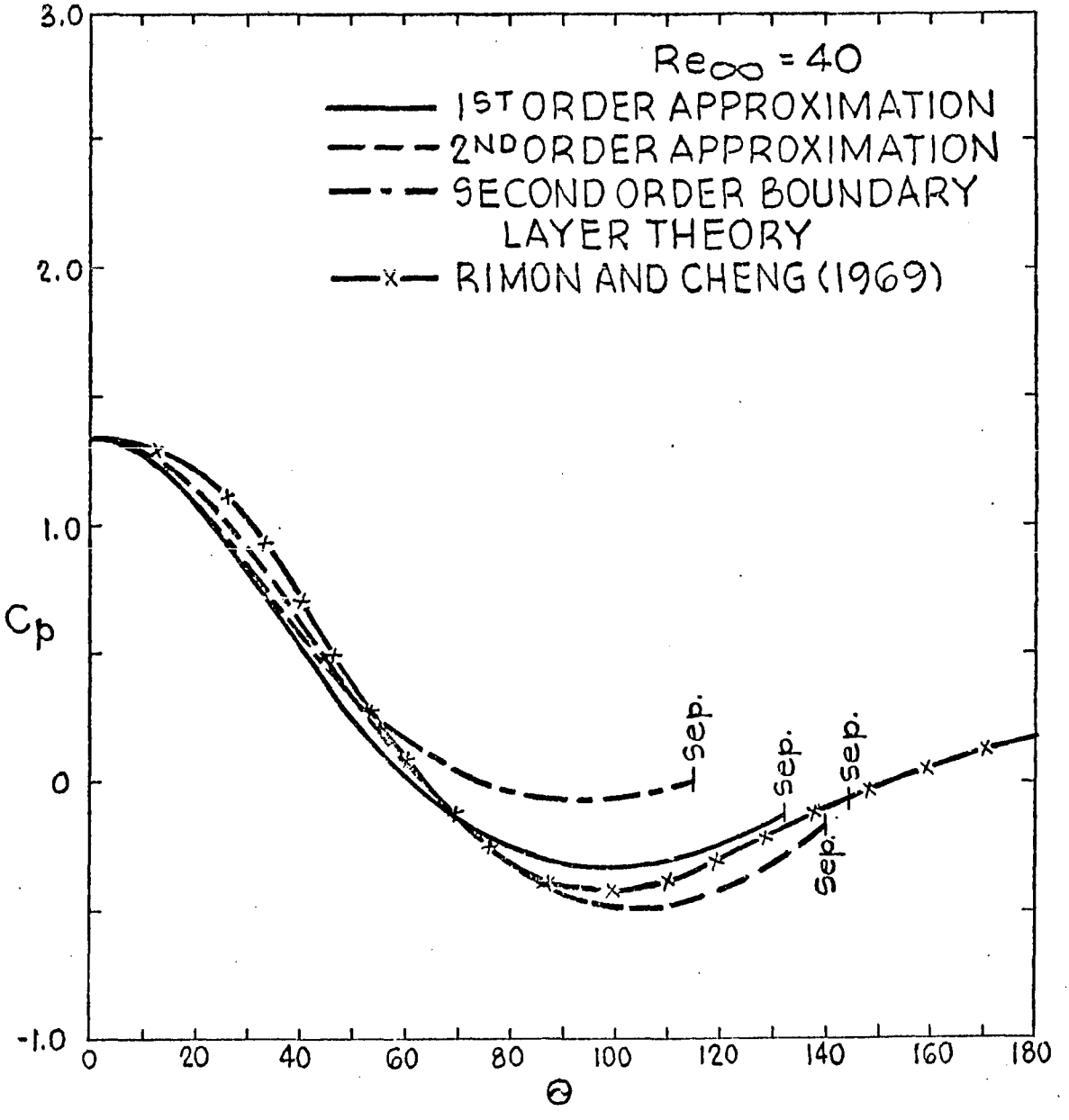

Figure 10. Surface Pressure Distribution around a Sphere.

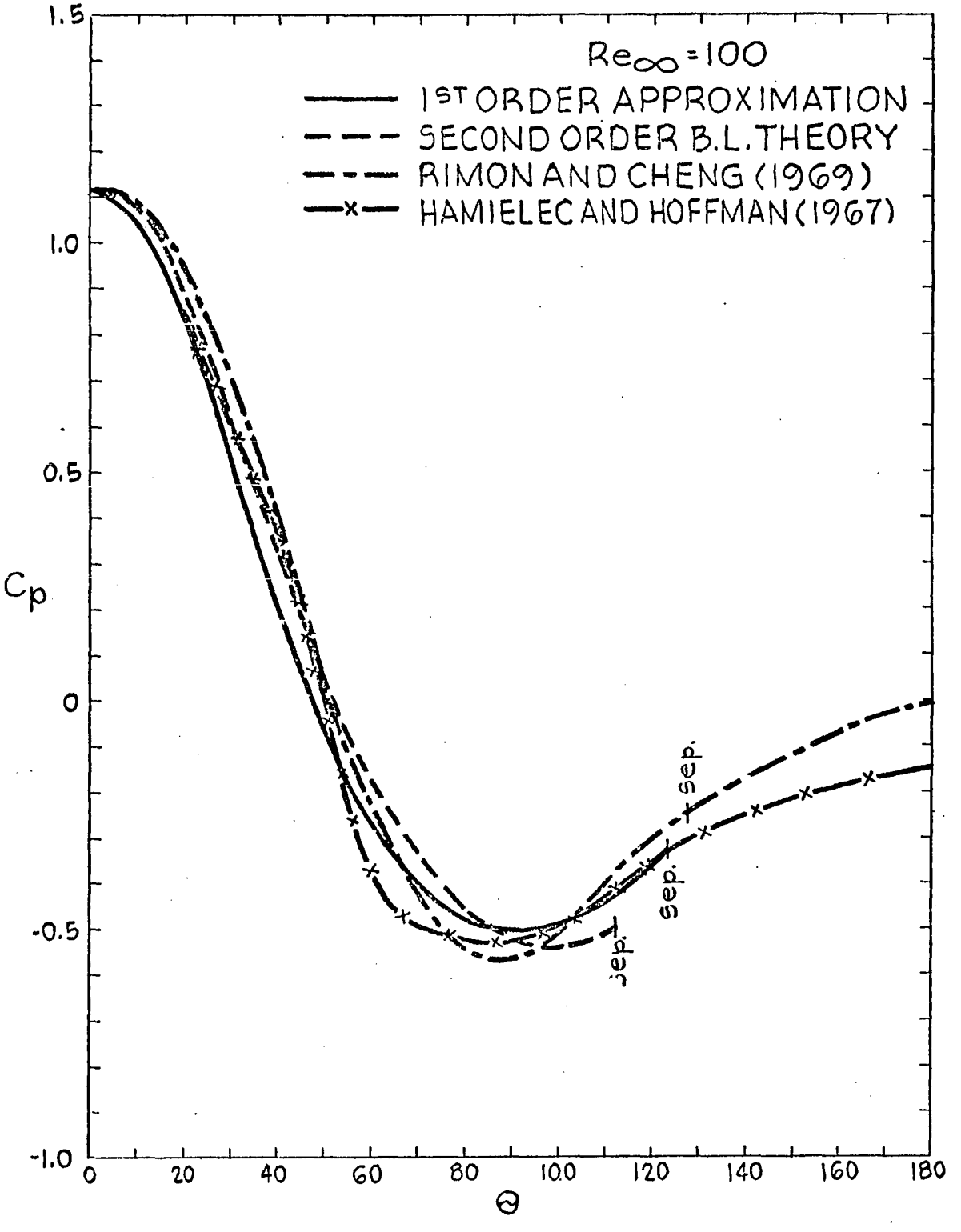

Figure 11. Surface Pressure Distribution around a Sphere.

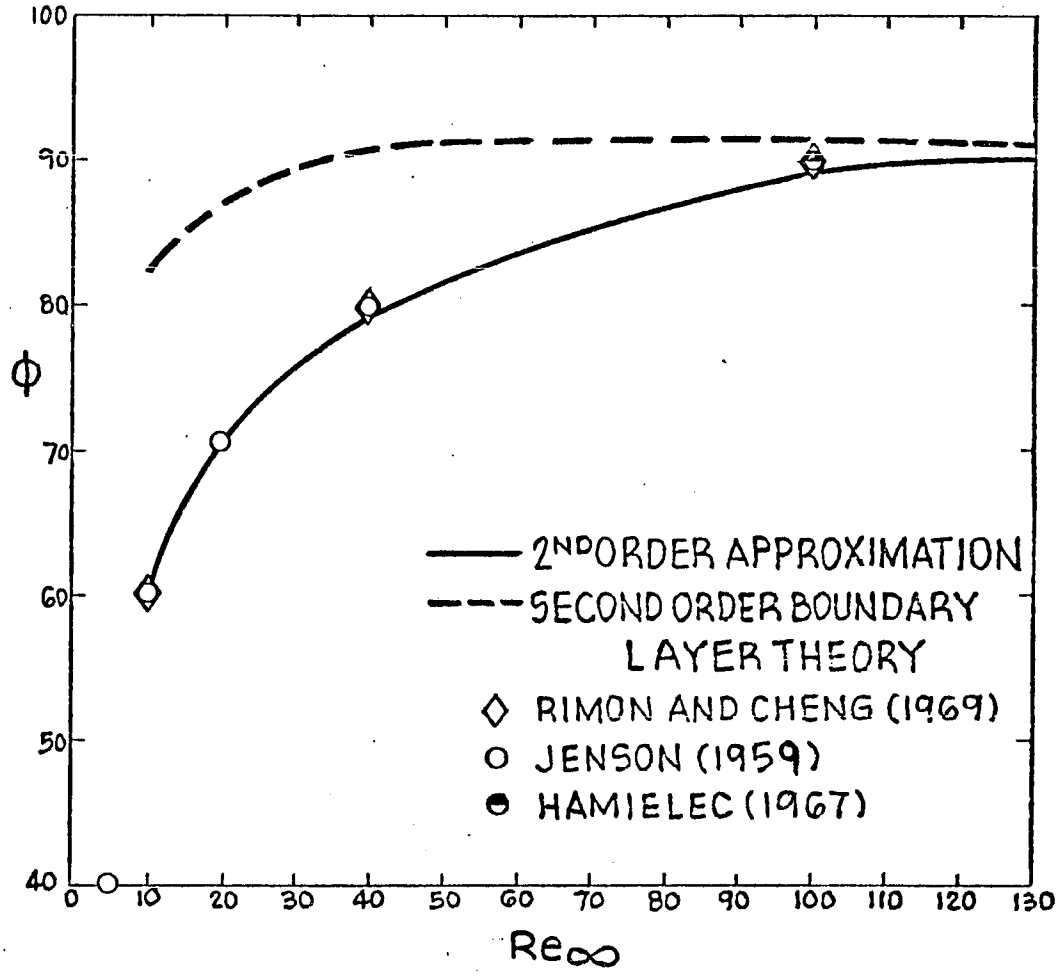

Figure 12. Angle of Minimum Surface Pressure for a Sphere.

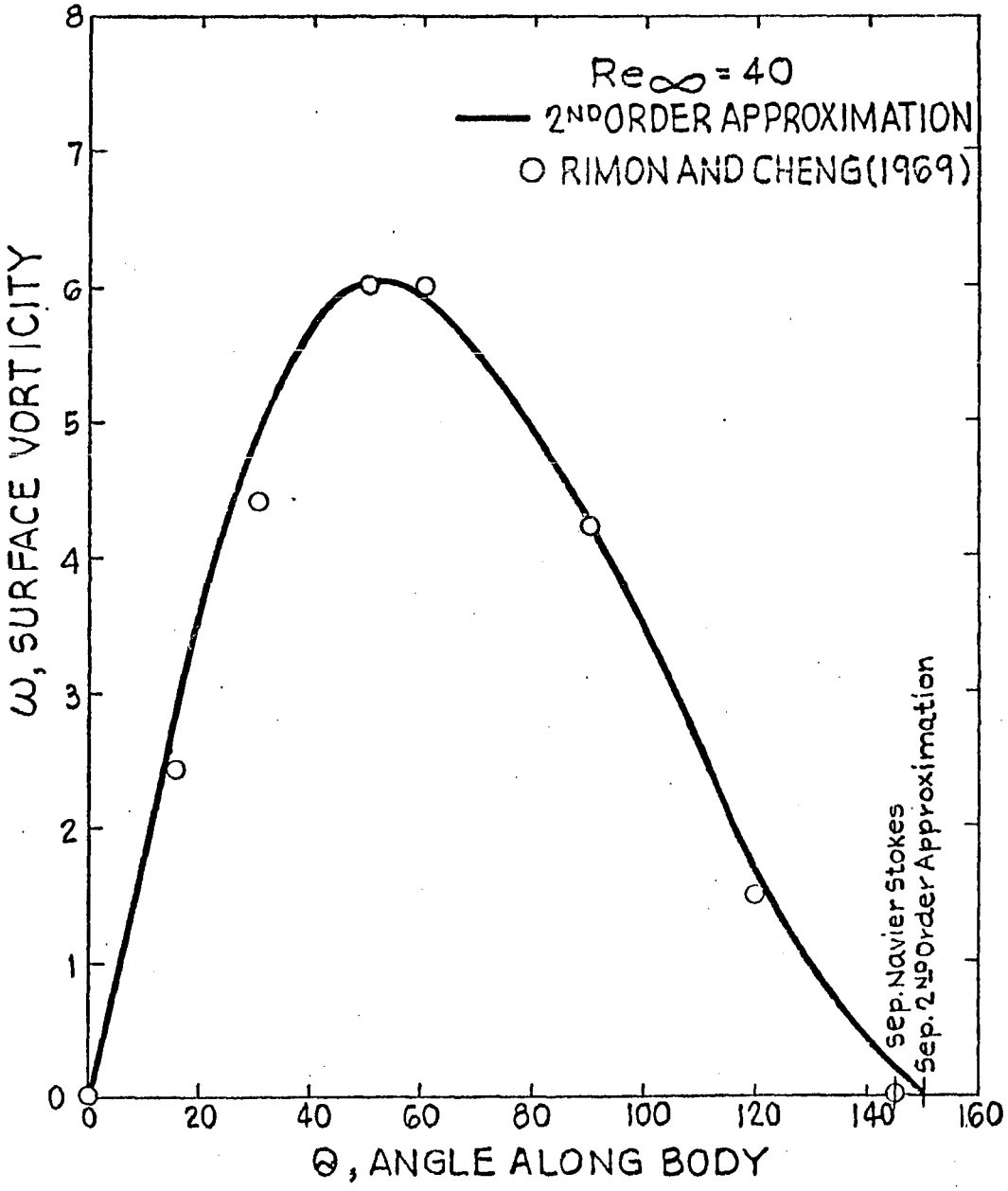

Figure 13. Surface Vorticity Distribution around a Sphere.

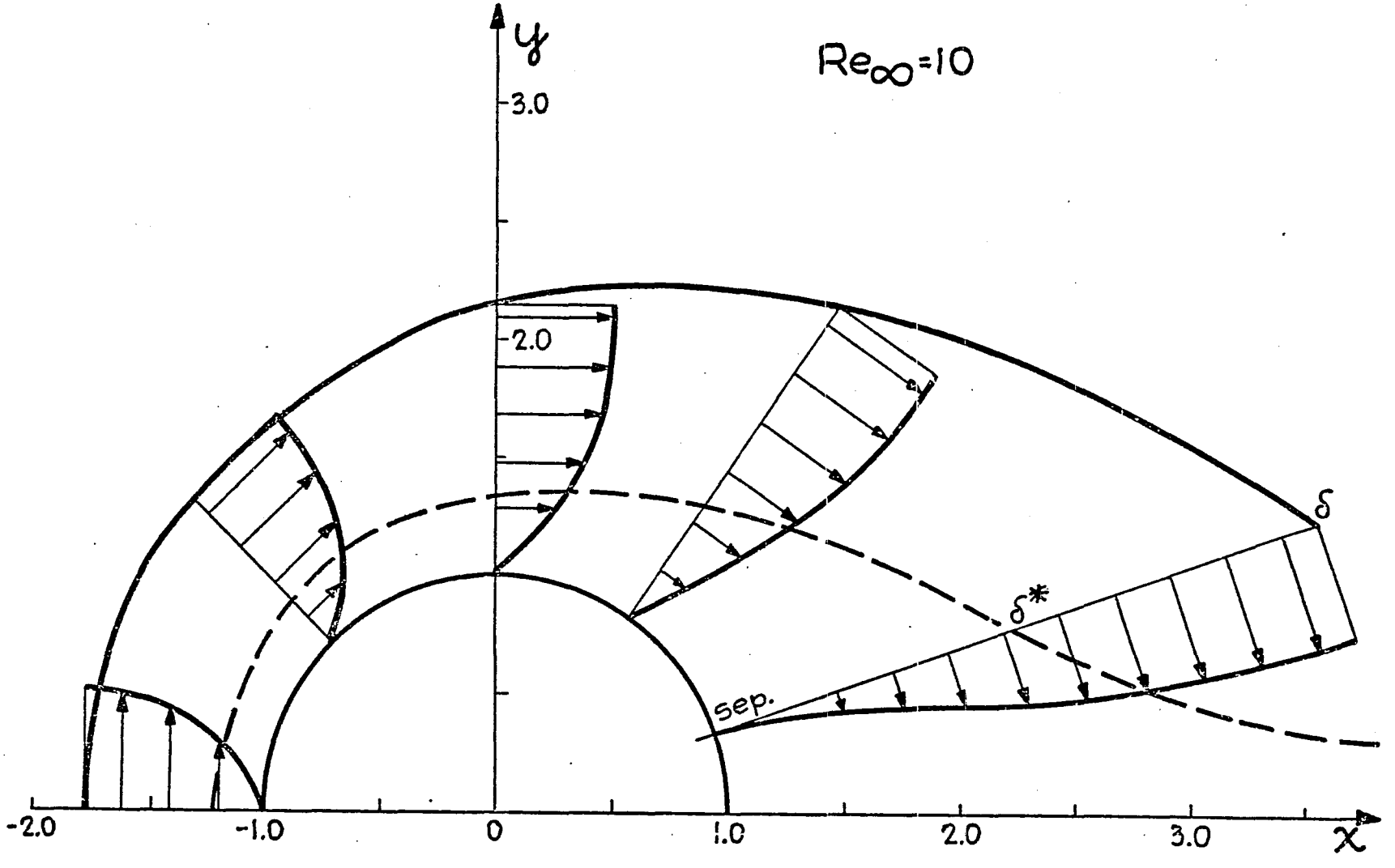

Figure 14. Velocity Profile Development in the Viscous Layer around a Sphere.

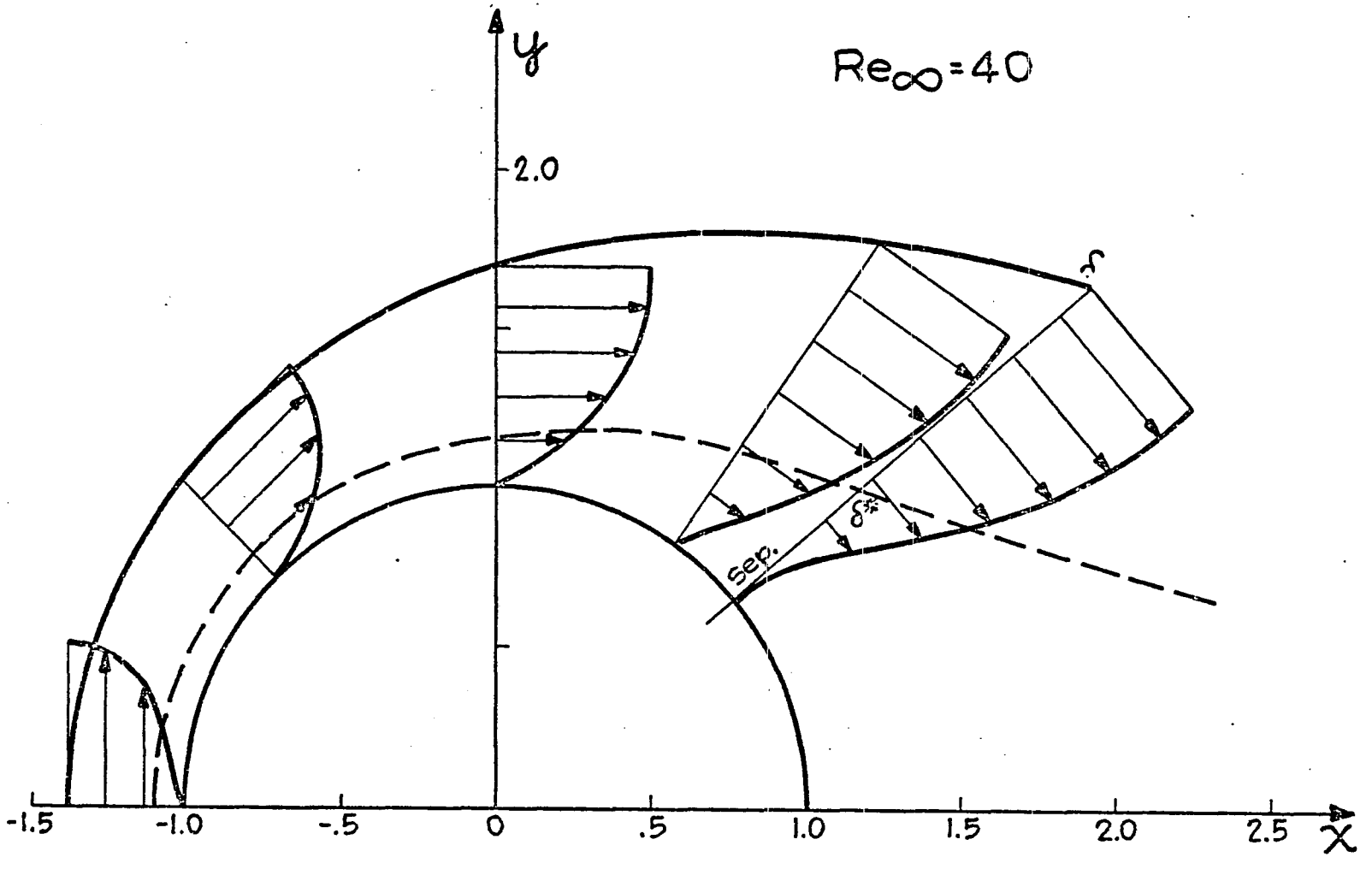

Figure 15. Velocity Profile Development in the Viscous Layer around a Sphere.

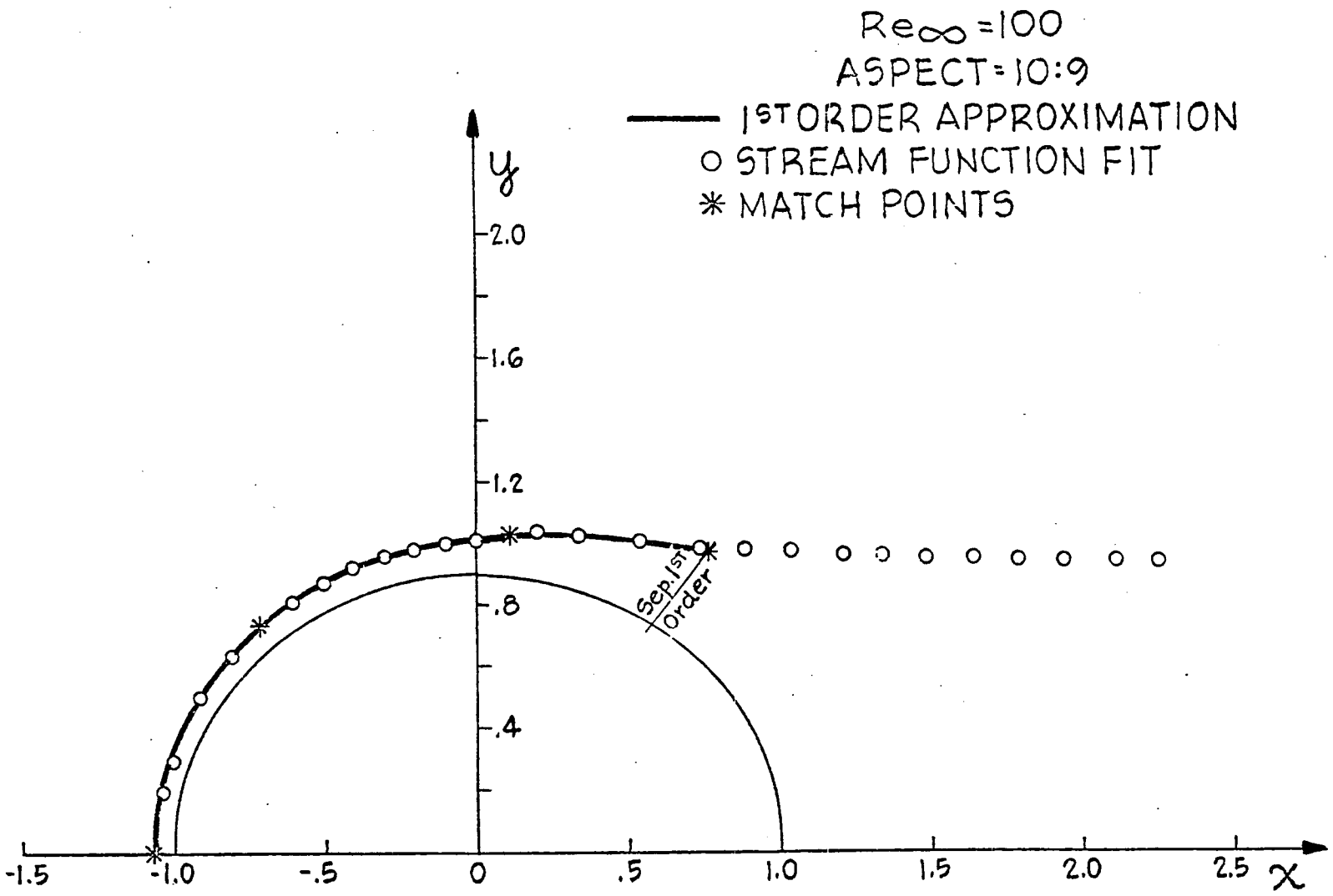

Figure 16. Stream Function Fit of the Displacement Body for a Prolate Spheroid.

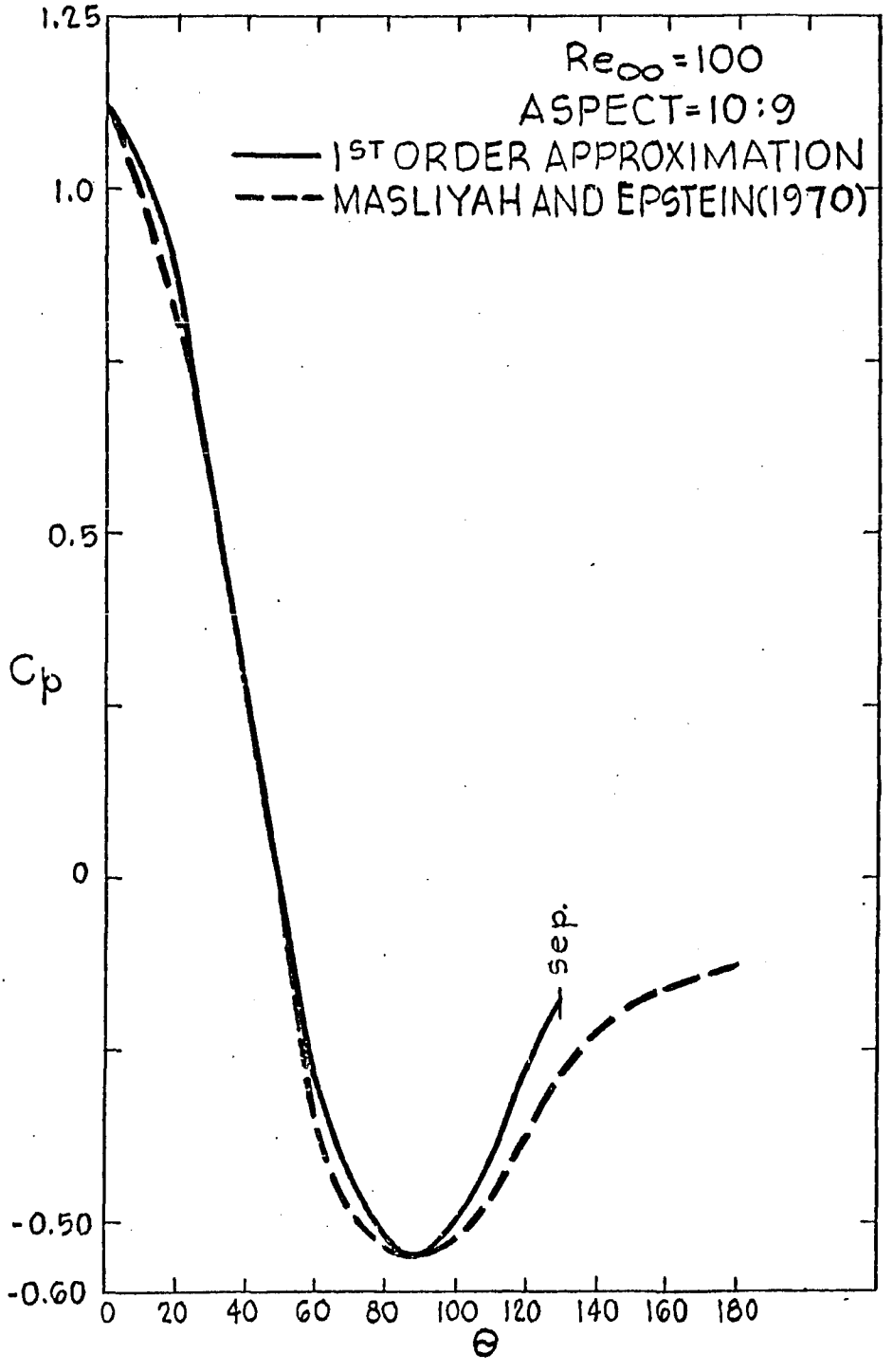

Figure 17. Surface Pressure Distribution around a Prolate Spheroid.

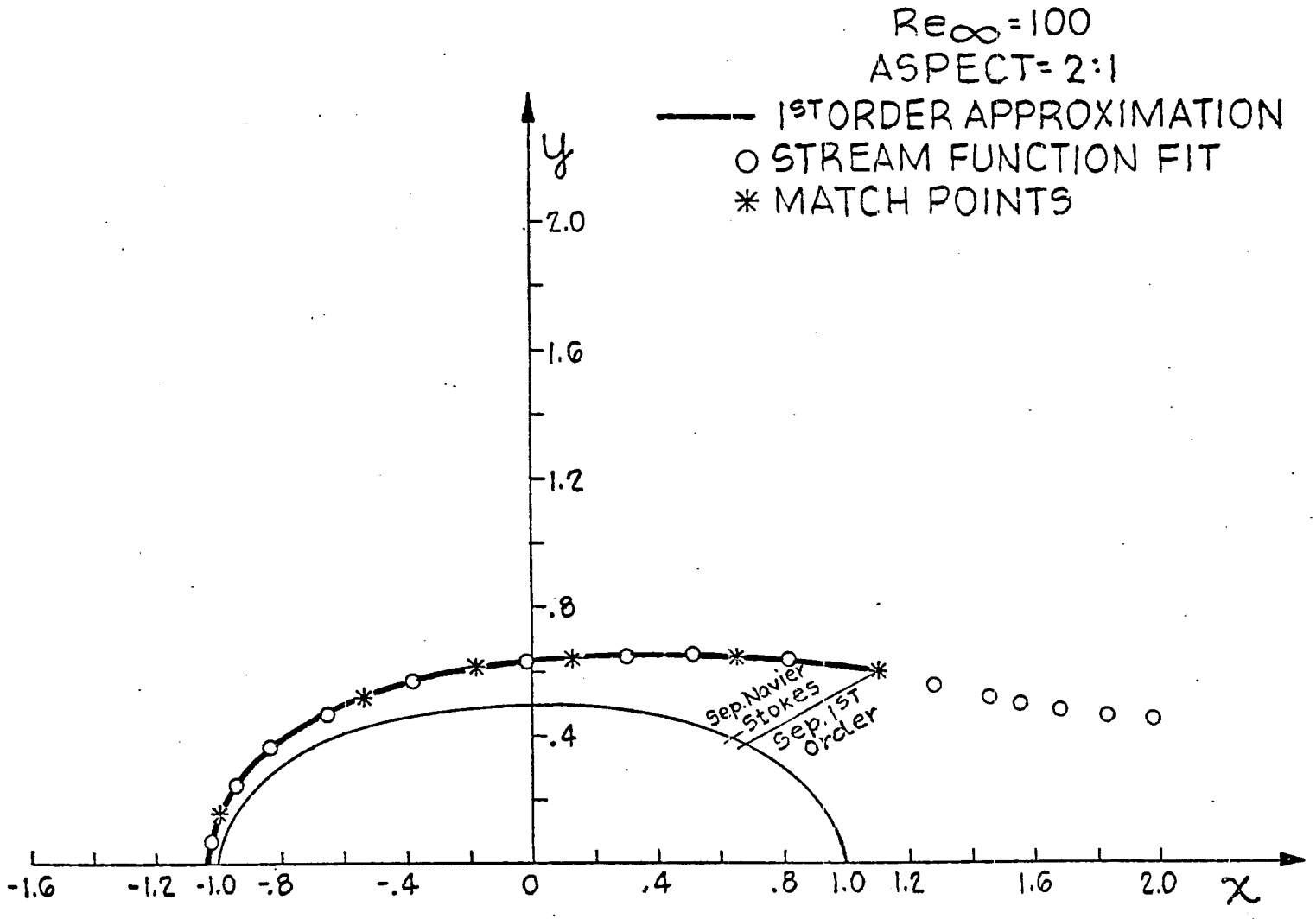

Figure 18. Stream Function Fit of the Displacement Body for a Prolate Spheroid.

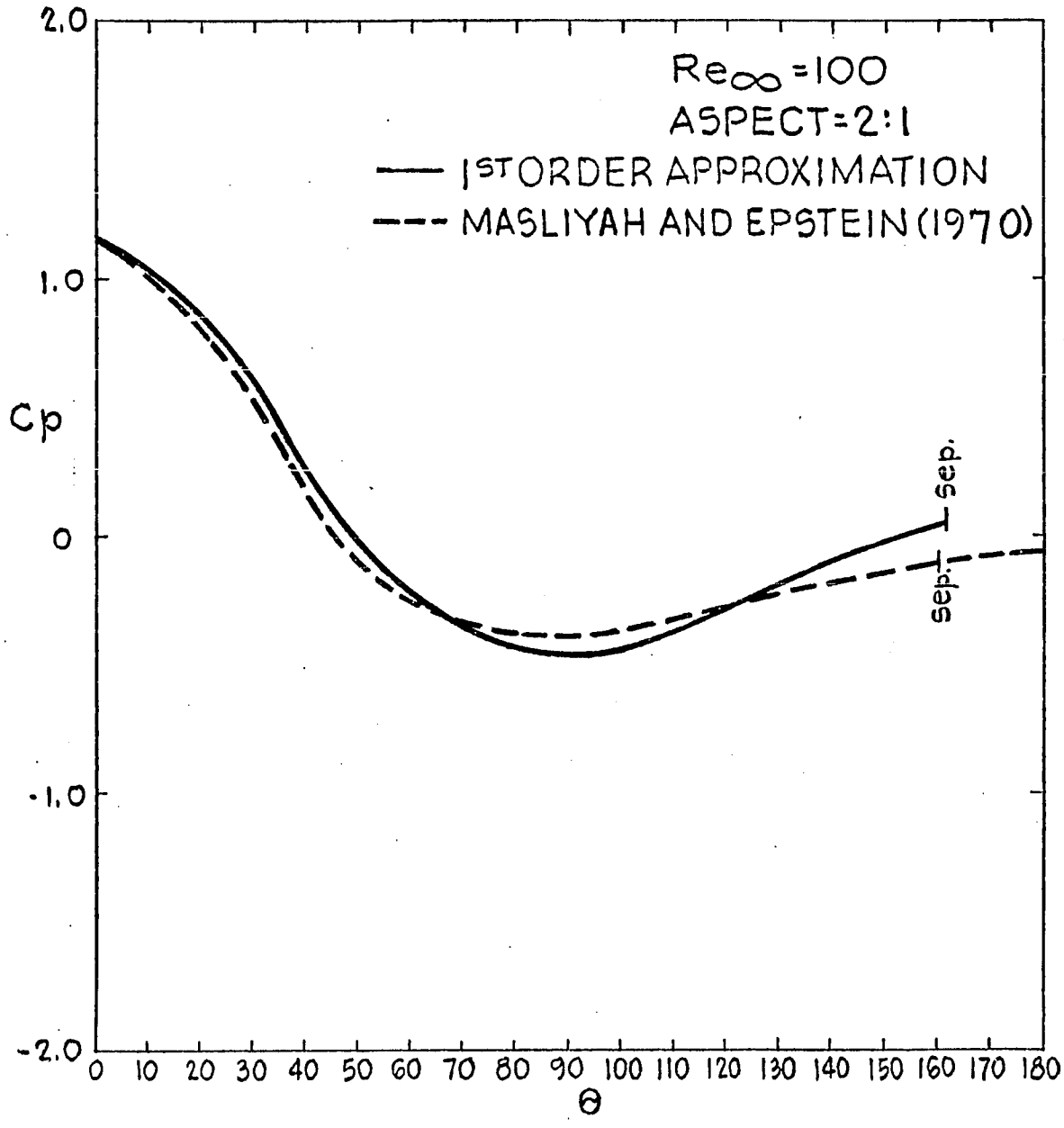

Figure 19. Surface Pressure Distribution around a Prolate Spheroid.

CHAPTER IV: CONCLUDING REMARKS

Chapter I

The present series of experiments have brought to light two new and interesting phenomena. The first is the fact that the von Karman constant for the gas phase is unaffected by the addition of particles whereas the solid phase, while it still obeys a logarithmic u^+ vs y^+ profile outside the buffer layer, exhibits a change in the proportionality constant as a function of loading ratio. The mixing length of the solid phase thus decreasing with increasing loading ratio. The second is the observation that the slip velocity between the gas and particles is not confined to the buffer region but extends well into the core up to $y/R = 0.5$ which is equivalent to 10 buffer layer thicknesses.

Previous theoretical models by Jotaki and Tomita (1971) and Kane et al (1973) which have attempted to explain the drag reduction mechanism in terms of the Stokesian dissipation between a particle and eddy, assumed that significant slip between the two phases is confined to a thin region of the order of the buffer zone. The present experiments indicate that large slip velocities in the near wall region are not generated but a significant slip extends well into the core. The integrated viscous dissipation due to particle slip across this much thicker region must, therefore, be of the same order as that calculated using a much thinner (buffer layer) model with a large slip velocity.

Chapters II and III

The proposed approximate theory, which is based on a reasonable intuitive derivation rather than rational arguments, has been shown to be in very good agreement with a broad spectrum of numerical Navier-Stokes solutions for the flow past smoothly contoured bodies in the Reynolds numbers range 5 to approximately 100. The theory can be easily applied to many boundary shapes for which published numerical Navier-Stokes solutions currently do not exist, e.g., the elliptic cylinders considered in Chapter II. The important fundamental contribution of the study is the improved understanding of the role and construction of the displacement body and the effect of centrifugal forces in thick viscous layers.

VITA

Michael Steven Kolansky was born in Brooklyn, New York, on August 4, 1949. He attended the City College of New York where he received his Bachelor's Degree in Chemical Engineering (1972) and his Master's Degree in Chemical Engineering (1974). Since completing his Master's Degree he has been engaged in Doctoral research at the Engineering graduate division of the City University of New York, located at the City College.

The author lives with his parents in Brooklyn, New York.